

**A DOUBLE SIDED SILICON STRIP DETECTOR AS AN
END DETECTOR FOR THE DRAGON RECOIL MASS
SEPARATOR**

by

Christopher Lars Henrik Wrede

B.Sc., University of Victoria

THESIS SUBMITTED IN PARTIAL FULFILLMENT
OF THE REQUIREMENTS FOR THE DEGREE OF
M.Sc.
IN THE DEPARTMENT
OF
PHYSICS

© Christopher Lars Henrik Wrede 2003
SIMON FRASER UNIVERSITY
June, 2003

All rights reserved. This work may not be
reproduced in whole or in part, by photocopy
or other means, without permission of the author.

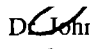
APPROVAL

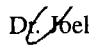
Name: Christopher Lars Henrik Wrede

Degree: M.Sc.

Title of Thesis: A Double Sided Silicon Strip Detector as an End Detector for the DRAGON Recoil Mass Separator

Examining Committee: Dr. John Bechhoefer
Professor, Simon Fraser University (Chair)

 John M. D'Auria
Professor, Simon Fraser University

 Joel G. Rogers
Research Scientist, TRIUMF

Dr. Michel Vetterli
Professor, ~~Simon Fraser University~~

Dr. Gregory Hackman
Research Scientist, TRIUMF

Date Approved: June 4th, 2003

PARTIAL COPYRIGHT LICENSE

I hereby grant to Simon Fraser University the right to lend my thesis, project or extended essay (the title of which is shown below) to users of the Simon Fraser University Library, and to make partial or single copies only for such users or in response to a request from the library of any other university, or other educational institution, on its own behalf or for one of its users. I further agree that permission for multiple copying of this work for scholarly purposes may be granted by me or the Dean of Graduate Studies. It is understood that copying or publication of this work for financial gain shall not be allowed without my written permission.

Title of Thesis/Project/Extended Essay

A DOUBLE SIDED SILICON STRIP DETECTOR

AS AN END DETECTOR FOR THE

DRAGON RECOIL MASS SEPARATOR

Author _____

(signature)

Christopher Lars Henrik Wreck

(name)

03/07/22

(date)

Abstract

The DRAGON electromagnetic recoil mass separator located at TRIUMF-ISAC in Vancouver, Canada was built to study resonant radiative proton and α -particle capture reactions relevant to nuclear astrophysics. In DRAGON experiments, a stable or radioactive ion beam in the energy range 0.15 MeV/amu to 1.5 MeV/amu from ISAC impinges on a differentially pumped, windowless gas target of hydrogen or helium. Recoiling reaction products are separated electromagnetically from beam ions and detected in the final focal plane, typically with a double sided silicon strip detector. A bench test facility for testing and improvement of the double sided silicon strip detectors and related systems has been assembled. The facility has been used to measure the efficiency and energy resolution of the detectors using an α -particle source, and to assess the effects of radiation damage on the detectors. The pulse height defect and the effect when particles pass through the gap between strips have been measured. Data from α -particle tests have been compared with data from stable beam experiments in the mass range $A = 12$ to $A = 25$, and used to predict detector performance in future DRAGON experiments. A 1 MeV/amu ^{16}O beam has been used to measure timing resolution. DRAGON has used this detector system successfully in measurements of the resonance strengths of several astrophysically relevant resonances in the $^{21}\text{Na}(p,\gamma)^{22}\text{Mg}$ reaction with a radioactive beam of ^{21}Na . A hybrid thermoelectric/liquid cooling system has been designed, built and tested with the purpose of cooling the double sided silicon strip detectors and improving their performance. The future possibility of using silicon detectors for particle identification by pulse-shape discrimination has been researched.

To my mom and dad.

Acknowledgments

Many people have contributed to the production of this work, and I would like to thank them. John D’Auria invited me to work with the DRAGON group, and his leadership and encouragement have motivated me throughout my work.

Professor Ahmed Hussein and Dr. Joel Rogers welcomed me to work with them on the DRAGON DSSSD system, which they conceived, and I have since learned many lessons from their knowledge and experience.

Hart Sprenger helped with the cooling system design work, and Heinz Biegenzein machined all three iterations of the design. Mike Lamey and Dario Gigliotti contributed to the mechanical assembly of the DSSSD test station. The technical expertise of Marielle Goyette, Peter Machule, Robert Openshaw and Dave Ottewell has been a asset throughout this work.

I would like to thank all DRAGONeers for contributing to the measurements done using DRAGON, and for their colourful character. In particular, the roar of the DRAGON would hardly be a squeak without the tireless efforts and physical insights of Professor Dave Hutcheon.

Several people took the time to read manuscripts of this document, each of whom suggested helpful revisions, including Shawn Bishop, John D’Auria, Ahmed Hussein, Mike Lamey (twice), and Joel Rogers.

Figures 4.1, 4.2, 4.4, 4.5, and 4.8 were provided by Ahmed Hussein. Figure 5.9 was provided by Joel Rogers.

Finally, I would like to thank my family and friends for their love and support.

Contents

Approval	ii
Abstract	iii
Dedication	iv
Acknowledgments	v
Contents	vi
List of Tables	ix
List of Figures	x
1 Introduction	1
1.1 Introduction	1
2 Nuclear Astrophysics	4
2.1 Novae	4
2.2 X-Ray Bursts	5
2.3 Supernovae	8
2.4 The Hot CNO Cycle and Beyond	8
3 DRAGON	10
3.1 The DRAGON facility	10
3.1.1 ISAC	10

3.1.2	Windowless Gas Target	12
3.1.3	Gamma Ray Detector Array	14
3.1.4	Mass Separator	14
3.1.5	Focal Plane Detection Systems	16
4	The DRAGON DSSSD	26
4.1	Semiconductor Diode Detectors	26
4.1.1	Band Theory of Solids	26
4.1.2	Semiconductors	27
4.1.3	The $p-n$ Diode Junction	28
4.1.4	Reverse Biased $p-n$ Junction as a Radiation Detector	29
4.1.5	Position Sensitive Diode Detectors	29
4.2	The DRAGON DSSSD Test Station	30
4.2.1	The DRAGON DSSSD	32
4.2.2	Vacuum Systems	32
4.2.3	Electronics and Data Acquisition	35
5	DSSSD Testing and Calibration	40
5.1	Energy Resolution	40
5.2	Relative Efficiency of Strips	42
5.3	The Pulse Height Defect	42
5.3.1	The Window Defect	42
5.3.2	The Nuclear Stopping Defect	45
5.3.3	The Residual Defect	47
5.3.4	Energy Calibration as a Function of Ion Species	48
5.4	The Gap Effect	52
5.5	Beam Testing Results	56
5.5.1	Energy and Time Resolution	56
5.5.2	The Forbidden Trough	58
6	DSSSD Cooling	60
6.1	DSSSD Cooling System Design	60
6.1.1	The Peltier Effect and its Application	60

6.1.2	Heat Transfer	62
6.1.3	Cooling System Design I	63
6.1.4	Testing of Cooling System Design I	65
6.1.5	Cooling System Design II	66
6.1.6	Testing of Cooling System Design II	67
6.2	Cooling New DSSSDs	75
6.2.1	Effect of Cooling on α -particle Energy Resolution	75
6.2.2	Effect of Cooling on Pulser Width	76
6.2.3	Effect of Cooling on Timing Resolution	80
6.3	Radiation Damaged Detectors	80
6.3.1	Radiation Damage	80
6.3.2	Radiation Damage to the DRAGON DSSSDs	81
6.3.3	Inventory of the DRAGON Silicon Strip Detectors	82
6.3.4	Cooling Radiation Damaged DSSSDs	82
7	Future prospects for the DRAGON DSSSDs	86
7.1	A, Z Discrimination	86
7.1.1	Rise-time	86
7.1.2	Relevance to DRAGON	88
7.1.3	Optimizing A, Z Discrimination	89
7.2	Installation of DSSSD Cooling on DRAGON (Cooling System Design III) .	90
8	Conclusions	93
	Bibliography	95

List of Tables

5.1	Energy resolution of individual strips for 5.486 MeV α -particles.	41
5.2	Window thickness measurements.	47
5.3	Calculated and measured pulse height defects.	49
5.4	Pulse height defects for proposed DRAGON reactions.	52
6.1	Thermal conductivities of cooling system materials	62
6.2	Cooling system, design II temperatures versus Peltier voltage.	72
6.3	DSSSD warming time.	73
6.4	DRAGON silicon strip detector inventory.	83
6.5	Efficiency of undamaged DSSSDs compared with that of radiation damaged DSSSDs.	83

List of Figures

1.1	Nuclear reaction vectors on the proton rich side in the $Z - N$ plane.	2
2.1	The nova mechanism.	6
2.2	The normal CNO cycle and one hot CNO cycle branch.	8
2.3	The hot CNO cycle branches and breakout paths.	9
3.1	Schematic of the Detector of Recoils and Gamma-rays of Nuclear Reactions.	11
3.2	Schematic of the TRIUMF-ISAC radioactive beams facility.	13
3.3	The DRAGON windowless gas target.	14
3.4	Technical drawing of the DRAGON BGO γ -ray detector array.	15
3.5	Schematic of the DRAGON iso-butane ionization chamber.	18
3.6	Schematic of the DRAGON parallel grid avalanche counter.	20
3.7	Schematic of the DRAGON micro-channel plates.	21
3.8	Schematic of the DRAGON position-sensitive timing detector.	23
3.9	Possible focal plane detector arrangements.	24
4.1	Diode current-voltage characteristics.	29
4.2	The geometry of a double sided silicon strip detector.	30
4.3	The DRAGON DSSSD test facility.	31
4.4	Schematic of electrical connections to DSSSD strips.	33
4.5	Micron Semiconductor W(DS)-250 DSSSD front view.	34
4.6	DSSSD test facility vacuum system.	36
4.7	RAL 108A,B preamplifiers in place.	37
4.8	The DRAGON DSSSD test station electronics.	38
4.9	DSSSD test facility electronics and data acquisition.	39

5.1	Projection of front strips with an un-collimated 5.486 MeV α -particle source.	43
5.2	Projection of back strips with an un-collimated 5.486 MeV α -particle source.	44
5.3	Window defect as a function of window thickness.	46
5.4	DSSSD singles spectrum for $^{21}\text{Ne}(p,\gamma)^{22}\text{Na}$ at 5.5 MeV showing the pulse height defect.	50
5.5	DSSSD γ -coincidence spectrum for $^{21}\text{Ne}(p,\gamma)^{22}\text{Na}$	51
5.6	Parallel collimator evidence: counts on strips adjacent to a collimated gap. .	54
5.7	Scan of a 180 μm collimator across two gaps and three strips.	55
5.8	Gap peak and full energy peak in 5.486 MeV α -particle energy spectrum with a collimator straddling a gap.	57
5.9	Scan of a 1 MeV/amu ^{16}O beam across a DSSSD.	59
6.1	Peltier effect in a thermoelectric pump.	61
6.2	Schematic of a Peltier cooler.	61
6.3	Cold plate for cooling system design I.	64
6.4	Outside of cooling system II vacuum plate and feed-throughs.	68
6.5	Inside of cooling system II vacuum plate.	69
6.6	Schematic of cooling system design II.	70
6.7	Effect of Peltier voltage on DSSSD temperature.	71
6.8	Restoration of ambient temperature of a cooled DSSSD.	74
6.9	Pulser spectrum for strip 10 with Peltier disconnected and power supply off.	78
6.10	Pulser spectra for strip 10 with Peltier a) disconnected and power supply off, and b) connected and 6 V applied.	79
6.11	Energy resolution of undamaged DSSSDs compared with that of radiation damaged DSSSDs.	85
7.1	Schematic of cooling system design III.	92

Chapter 1

Introduction

1.1 Introduction

Without invoking nuclear physics, we cannot scientifically answer the question, “where do we come from?” in depth. We can inquire about the biochemistry and genetics of the reproduction process [1], the evolution of our species [2], or the origin of life on Earth. All of these inquiries yield to a more fundamental question: how were the copious chemical elements that make up the Earth and everything on it produced [3]? The lightest elements, hydrogen and helium, were produced in abundance shortly after the Big Bang [4, 5], in the Big Bang nucleosynthesis [6]. Heavier elements like carbon, oxygen, silicon and iron (important for our Earth and the life on it) are produced by fusing lighter nuclei into heavier ones in nuclear processes in stars; stellar nucleosynthesis [7, 8]. Some of the heaviest elements can only be produced in explosive processes involving stars; explosive stellar nucleosynthesis. Nuclear astrophysics is the study of nuclear processes in the cosmos, and it has had great success in explaining some types of objects and events that we observe in space, and the chemical elements that these objects and events are able to produce by nuclear processes [9].

Nuclear astrophysics and cosmology have been used successfully to explain the abundance of the light elements (D, ^3He , ^4He and ^7Li) produced in the first 200 seconds after the Big Bang [10]. The rates of quiescent burning in main-sequence stars (stellar nucleosynthesis) are well understood because they involve nuclei near the valley of stability on the chart of nuclides which are readily available and therefore relatively easy to study. Quiescent

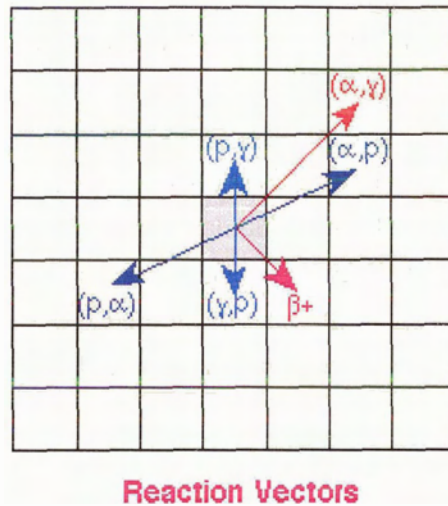


Figure 1.1: Nuclear reaction vectors on the proton rich side in the $Z - N$ plane.

burning proceeds by relatively slow processes like the pp chain, the CNO cycles, the He- and C- burning sequences and the s-process [11, ch. 6]. Radioactive nuclei do not play an important role in quiescent burning because temperatures and densities are so low that any radioactive nucleus produced usually β -decays before it reacts with another nucleus. However, in explosive stellar environments, sufficiently high temperatures and densities may be reached for a radioactive nucleus to be produced and undergo several successive captures of protons, α -particles, or neutrons before undergoing β -decay. These explosions, termed x-ray bursts, novae and supernovae are driven in part by nuclear processes involving unstable nuclei. A knowledge of the nuclear structure, and reaction and decay rates of unstable nuclei far from the valley of stability is necessary to model the energy generation in these explosions and to predict their elemental output [12] (figure 1.1).

Direct measurement of reaction rates relevant to explosive burning must be done with either radioactive ion beams or radioactive targets. The temperature in explosive burning environments is higher than that for quiescent burning, and therefore the particle energies are higher and the range of reactive particle energies, or Gamow peak, is broader, resulting in larger proton and α -particle capture cross sections and than normally encountered in

quiescent burning environments [11, p. 163]. These reactions are, nevertheless, difficult to study because of the high intensity of radioactive beams required and the relatively large levels of background radiation encountered in such experiments [13]. Several radioactive ion beam facilities have been constructed to meet the challenge of studying nuclear reactions relevant to explosive nucleosynthesis [14]. One of these is the TRIUMF-ISAC [15, 16] facility located in Vancouver, Canada which delivers radioactive beams to several experimental stations including the Detector of Recoils And Gamma rays Of Nuclear reactions (DRAGON) [17]. DRAGON was built to measure the cross sections of radiative resonant proton and α -particle capture reactions at the energies encountered in explosive astrophysical scenarios.

Direct measurement of a nuclear capture cross section requires detection of the reaction product. DRAGON has employed a double sided silicon strip detector (DSSSD) for this purpose [18]. The subject of this thesis is the assembly, testing and improvement of the DRAGON DSSSD system for detection of low energy heavy ions.

Chapter 2

Nuclear Astrophysics

In general, nuclear astrophysics is the study of the nuclear physics relevant to astrophysics and vice-versa [3]. One particular application of nuclear astrophysics is the use of nuclear structure information, and reaction and decay rates, to model energy generation and elemental abundance during the course of, and following, an explosive astrophysical event [12]. Novae, supernovae and x-ray bursts are explosive astrophysical events in which nuclear physics plays a prominent role [19].

2.1 Novae

Novae were first observed as stars that appeared where there had formerly been no star observable to the naked eye [20, p. 363]. They acquired their name from the Latin “stella nova” meaning “new star”. We now interpret novae not as new stars, but instead as the intense brightening of a white dwarf star in a binary star system by as many as 20 orders of magnitude [19].

When a star of mass less than $1.4 M_{\odot}$ ¹ has exhausted its nuclear fuel, it collapses under gravity [21]. Its core may form a dense object composed of either carbon and oxygen if the star has completed helium burning, or oxygen, neon and magnesium if the star is massive enough to complete carbon burning [22]. The object is supported against gravity by degenerate electron pressure rather than radiative pressure from nuclear burning [23].

¹ M_{\odot} and L_{\odot} refer to the solar luminosity and mass respectively

Such a star may contain the mass of the Sun ($m \approx 2 \times 10^{30}$ kg) in a volume close to that of the Earth. We call this object a white dwarf star since it is hot ($T \approx 2 \times 10^5$ K) and small ($R \approx 1 \times 10^7$ m).

If a white dwarf has a companion star orbiting close enough to fill its Roche lobe, the figure-eight shaped gravitational equipotential surface surrounding two spherically symmetric matter distributions [11, p. 123], then the white dwarf accretes material from the surface of the companion star (figure 2.1). In a likely scenario, this material is hydrogen and helium from a red giant star. By hitting the surface of the white dwarf at high velocities because of the strong gravitational field of the white dwarf, this material creates high temperatures on the surface of the white dwarf. The matter on the surface of the white dwarf is degenerate so it is not able to expand and cool as it would on the surface of a non-degenerate star. Instead, there is a condition of temperature increase at constant pressure and density. Once sufficient mass is accreted, thermonuclear ignition takes place at the bottom of the accreted envelope via the pp-chains. Dredge up of carbon and oxygen catalyzes a thermonuclear runaway via the CNO cycles (see section 2.4) which lifts the degeneracy once the Fermi temperature is exceeded [24]. A tremendous amount of energy is produced in this process, and the white dwarf may brighten to $10^5 L_{\odot}$ [25]. This super-Eddington luminosity [26] results in a nova explosion which ejects the accreted envelope and enriches the interstellar medium with newly formed nuclei.

2.2 X-Ray Bursts

The atmosphere of the Earth is not transparent to x-rays. It follows that x-ray astronomy must be done with instruments located high in the atmosphere of the Earth or in space. Balloon-borne and satellite x-ray observatories have been used to observe objects in space that emit periodic pulses of x-rays, and objects that emit periodic or aperiodic bursts of x-rays [27]. Well accepted theories have been devised to explain these x-ray phenomena.

If the Chandrasekhar mass limit of $1.4 M_{\odot}$ [21] is reached by a star formerly stabilized by degenerate electron pressure, then it collapses into a denser object in which most of the nucleons have been converted to neutrons via electron capture ($p^+ + e^- \rightarrow n + \nu_e$), an endothermic process made possible by the dependence of degenerate electron energy on density [28, p. 599]. In a commonly accepted model, the resulting object is stabilized by

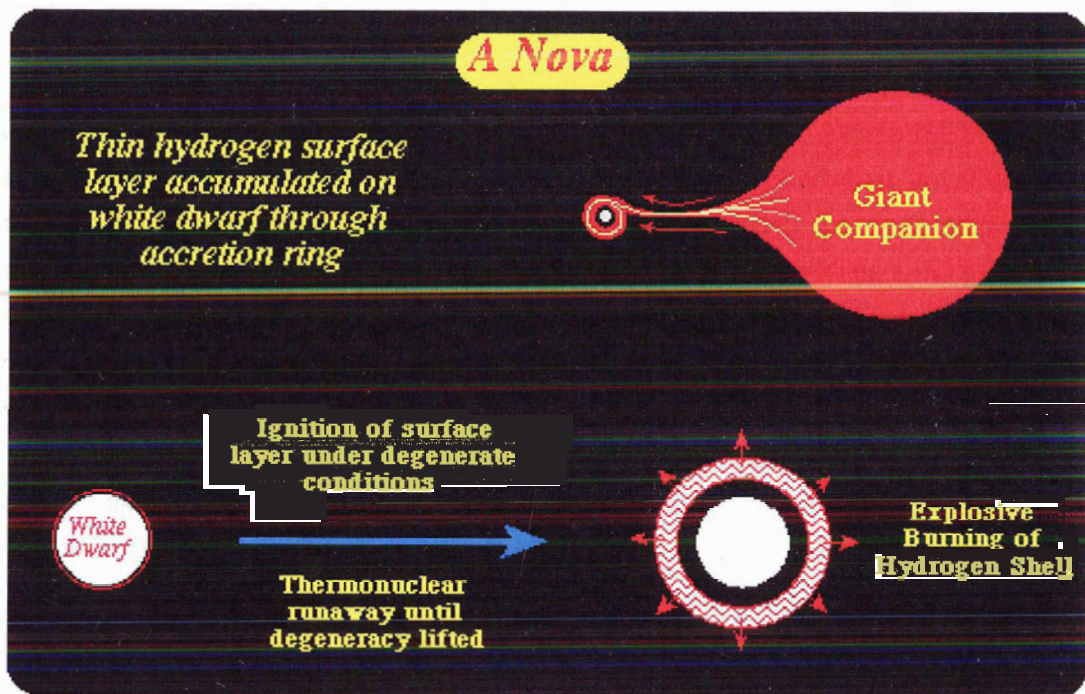


Figure 2.1: The nova mechanism.

the degenerate Fermi pressure of its constituent neutrons, forming an object of radius about 10 km, and mass $1.4 M_{\odot}$ to $1.8 M_{\odot}$ [29] [30, ch. 5]. We call this object a neutron star and it is approximately 9 orders of magnitude denser than a white dwarf .

A neutron star may have a hydrogen burning companion, forming a binary system. Again, if the two stars are close enough together that mass transfer can occur, then material (hydrogen and helium) from the larger star accumulates on the surface of the neutron star. Many neutron stars have strong magnetic fields as remnants of their progenitors [30, ch. 5]. Material from a companion can spiral down to a neutron star around the magnetic field lines of the neutron star at high velocities due to the extremely strong gravitational field of the neutron star, with each particle emitting energy in the form of many x-rays [31]. As the neutron star rotates, we may observe periodic pulses of x-rays in a lighthouse-like effect when the magnetic poles point towards us since the axis of rotation and direction of the magnetic field are not required to coincide [32]. We may also observe a longer period oscillation in x-ray flux due to eclipsing of the neutron star by its companion as they orbit each other [30, ch. 5]. These x-ray stars, called “x-ray pulsars”, are not thought to be emitting periodic bursts of x-rays; rather they emit a more constant flux of x-rays that are observed as periodic due to rotation or revolution.

Near the center of the Galaxy in globular clusters (regions associated with old stars), periodic and aperiodic bursts of x-ray emission from distinct sources lasting 1 s to 10 s have been observed [33]. The x-ray spectra from these bursts are consistent with black-body emission from compact objects with a radius of approximately 10 km and temperature between 1 keV and 2.5 keV, i.e. neutron stars. If a neutron star is older, then its magnetic field should be weaker, and we should not expect to observe the lighthouse-like effect of x-ray emission. If the companion star is old then it must burn hydrogen relatively slowly and be small, which reduces the probability of a longer term oscillation in x-ray emission due to eclipse. The observation of aperiodic x-ray bursts have been attributed to thermonuclear flashes occurring on the surfaces of old neutron stars when they have accreted a sufficient amount of hydrogen rich material. Such a flash ought to release a burst of x-rays; hence the identification of the observed and model “x-ray burst” occurring on the surface of an “x-ray burster”. X-ray bursters and novae have been suggested as possible sites for the astrophysical rp- process [34], where protons are captured successively on radioactive nuclei on timescales that allow them to bypass β -decay.

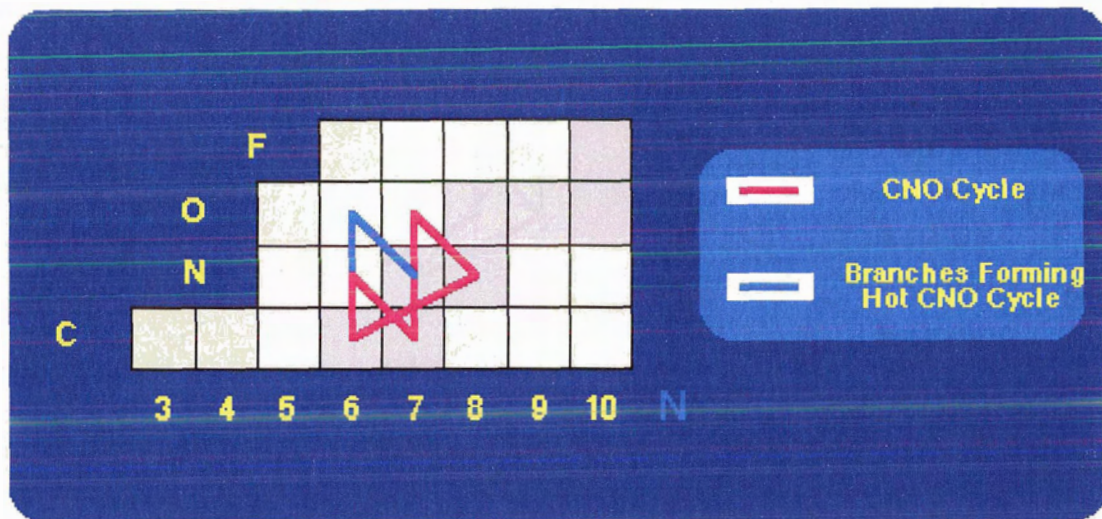


Figure 2.2: The normal CNO cycle and one hot CNO cycle branch.

2.3 Supernovae

The core collapse of a massive ($> 8 M_{\odot}$) star can result in an explosion in which most of the mass of the star is expelled into space, called a type II supernova. Since neutronization occurs in the core of a supernova, the rapid neutron capture process (r-process) predominates there [9].

2.4 The Hot CNO Cycle and Beyond

in stars larger than the Sun, hydrogen burning occurs increasingly with increasing temperature via a set of nuclear reaction and decay cycles involving relatively heavy nuclei compared to the pp-chains. There are four such cycles and they are known as the CNO-cycles. Shown in figures 2.2 and 2.3 are the normal CNO cycle and the hot CNO cycle branches respectively. The hot CNO cycle becomes important when sufficiently high temperatures and densities are reached for the $^{13}\text{N}(p,\gamma)^{14}\text{O}$ reaction² to bypass β -decay of ^{13}N [35].

In explosive astrophysical environments, temperatures greater than 10^8 K can be reached [11,

²The notation $X(a,b)Y$ refers to a nuclear reaction with a heavy reactant, X, a light reactant, a, a light product b, and a heavy product, Y.

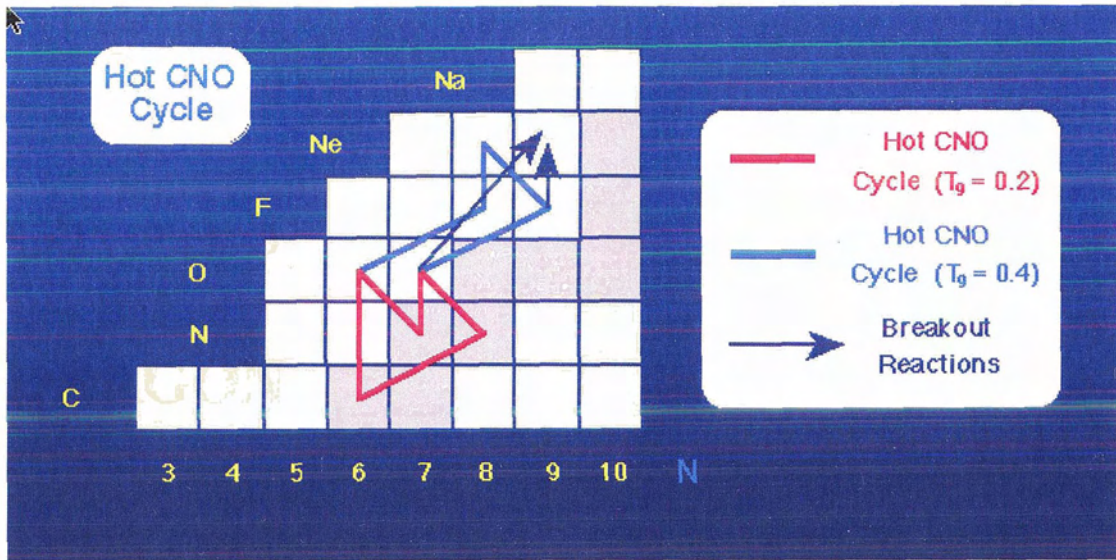


Figure 2.3: The hot CNO cycle branches and breakout paths, T_9 denotes a temperature in units of 10^9 K.

ch. 5,6]. At these temperatures the timescale for proton and α -particle capture reactions may become short enough to compete with β -decay for some nuclides at points in a cycle where there is a β -decay at lower temperatures. For example, in the CNO cycles $^{15}\text{O}(\alpha, \gamma)^{19}\text{Ne}$ may begin to compete with $^{15}\text{O}(\beta^+ \nu_e)^{15}\text{N}$, leading to a breakout from the CNO cycles, and a diversion of nuclear flow to heavier nuclei by the rp-process (figure 2.3) [34]. At high enough temperatures, in proton and α -particle rich environments, heavier nuclei may be produced with nuclear flow following the proton drip line closely where β^+ decay competes with further capture reactions.

These nuclear processes are important for energy generation in an explosion, and for heavy element production in the universe. For example, the hot CNO cycle is the dominant energy generation process in novae [9], and the rp-process in x-ray bursts provides a path for production of heavy elements [34]. To quantify these issues, measurements of proton and α -particle capture cross sections on radioactive nuclei are required [3]. By performing a nuclear network calculation, one can use the data obtained from such measurements to model nuclear flow and energy generation through the course of an explosion [25].

Chapter 3

DRAGON

3.1 The DRAGON facility

The Detector of Recoils And Gamma rays Of Nuclear reactions (DRAGON) is located at the TRIUMF-ISAC radioactive beams facility in Vancouver, British Columbia, Canada. It was built to measure directly, using inverse kinematics, the resonant radiative proton and α -particle capture cross-sections of unstable nuclei thought to exist in explosive astrophysical environments like novae, supernovae, and x-ray bursts. A stable or radioactive beam is delivered by ISAC to the DRAGON windowless gas target of either hydrogen or helium, where it may undergo a resonant proton or α -particle capture to an excited state of a product nucleus which promptly decays by γ -ray emission. Surrounding the gas target is an array of γ -ray detectors to detect these prompt reaction γ -rays. Recoiling reaction products are separated from the beam electromagnetically and detected in the final focal plane. Figure 3.1 shows a schematic of DRAGON.

3.1.1 ISAC

The Isotope Separator and Accelerator (ISAC) facility at TRIUMF is capable of producing stable or radioactive ion beams up to mass $A = 30$ with energy fully variable in the range 0.15 MeV/amu to 1.5 MeV/amu and radioactive beam intensities of 10^8 ions/s [36, 37] in the case of ^{21}Na , for example.

Radioactive ion beams are produced by the Isotope Separation On-Line (ISOL) tech-

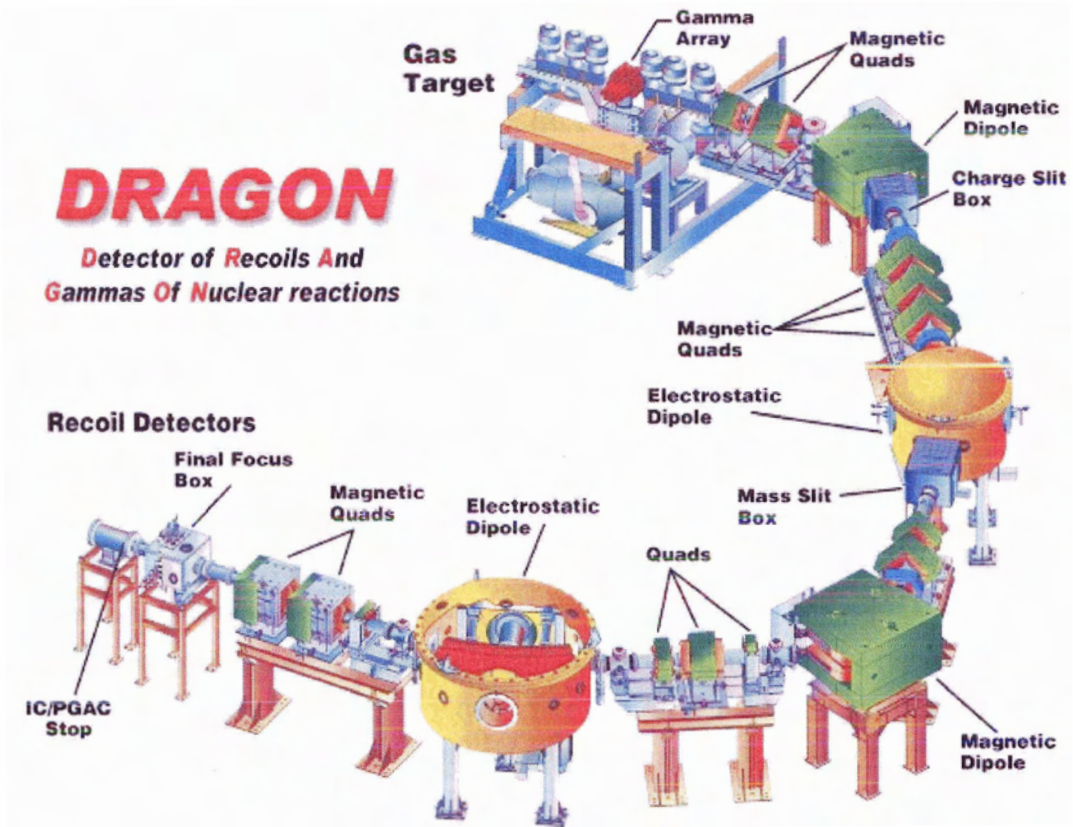


Figure 3.1: Schematic of the Detector of Recoils and Gamma-rays of Nuclear Reactions.

nique. The ISOL system consists of a primary production beam of protons of energy 500 MeV and intensity up to 100 μA from TRIUMF's main cyclotron, a target/ion source (a SiC target, for example, can produce ^{21}Na by spallation of Si), a mass separator and low energy beam transport [15]. Alternatively, stable ions may be provided by an off-line ion source.

In either case, the ions may be delivered to a low energy experimental area or accelerated through an 8 m long Radio Frequency Quadrupole (RFQ), and a Drift Tube Linac (DTL) [16] to a higher energy experimental area. The RFQ can accelerate ions with charge to mass ratio in the range $1/30 \leq q/A \leq 1/6$ to an energy of 150 keV/amu. The beam then passes through a thin carbon electron stripper foil and enters the DTL, which accepts ions with charge to mass ratios in the range $1/6 \leq q/A \leq 1/3$, and accelerates them to the higher energy ISAC experimental stations, including DRAGON, with energy fully variable between 0.15 MeV/amu to 1.5 MeV/amu. Figure 3.2 shows a schematic of the ISAC facility.

3.1.2 Windowless Gas Target

In DRAGON experiments, the ion beam is incident upon a differentially pumped, trapezoidal windowless gas target cell, of either hydrogen or helium, designed for a central pressure between 0.2 torr and 10 torr, with a nearly constant gas density in the 11 cm between apertures [38]. Inverse kinematics are used because most of the radioactive ions of interest would decay before they could be assembled in a target. The gas target is windowless because ions would undergo significant energy loss and straggling in window material degrading the energy resolution of DRAGON.

A small fraction of incident ions react with the target gas in (p, γ) or (α , γ) reactions. Two silicon elastic scattering monitor detectors are mounted at 30° and 57° relative to the beam axis to measure luminosity by detecting elastically scattered protons or α -particles from the target. The beam intensity can then be deduced with a knowledge of gas target pressure. Figure 3.3 shows a photograph of the inside of the DRAGON gas target including the trapezoidal gas cell and adjacent elastic scattering monitor mounts.

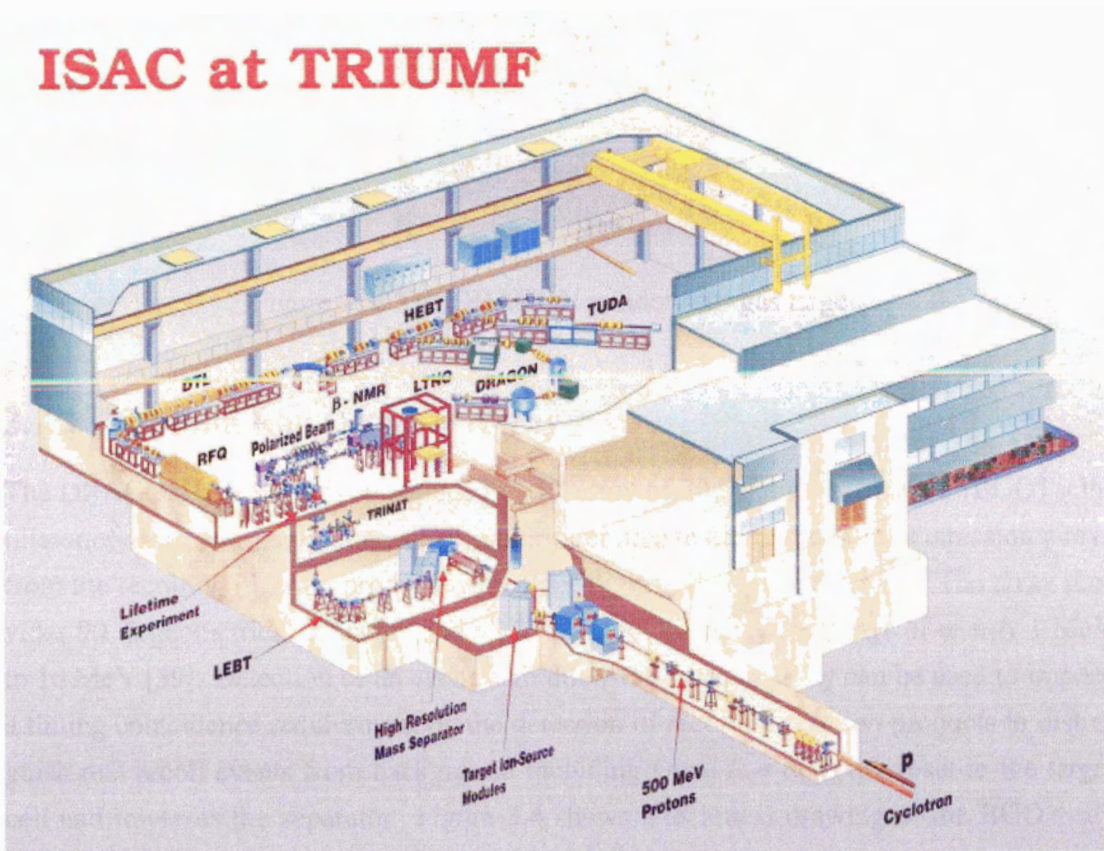


Figure 3.2: Schematic of the TRIUMF-ISAC radioactive beams facility.

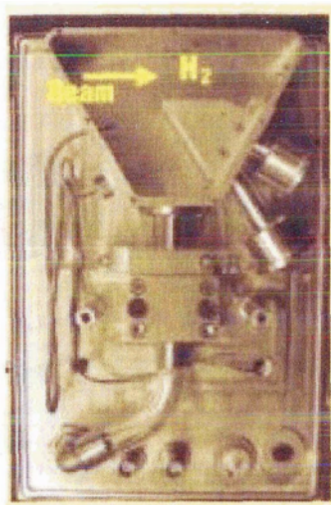


Figure 3.3: The DRAGON windowless gas target.

3.1.3 Gamma Ray Detector Array

The DRAGON gas target is surrounded by an array of 30 bismuth germanate (BGO) scintillator crystals, each coupled to a photomultiplier tube to detect the prompt emission γ -rays from the recoiling reaction products which decay from their excited states. The array provides 90 % geometrical coverage and 45 % to 60 % efficiency for γ -rays of energy 1 MeV to 10 MeV [39]. Detection of an event with this γ -ray detector array can be used to impose a timing coincidence requirement on the detection of recoiling reaction products to distinguish real recoil events from background including beam that does not react in the target cell and traverses the separator. Figure 3.4 shows a technical drawing of the BGO γ -ray detector array surrounding the gas target box.

3.1.4 Mass Separator

Upon exiting the gas target, the recoiling reaction products are overwhelmed by factors of 10^{10} to 10^{15} by the beam which has nearly the same momentum and trajectory due to inverse kinematics. To detect the recoil products, the beam must be suppressed by 10 to 15 orders of magnitude, which is partially done with an electromagnetic separator.

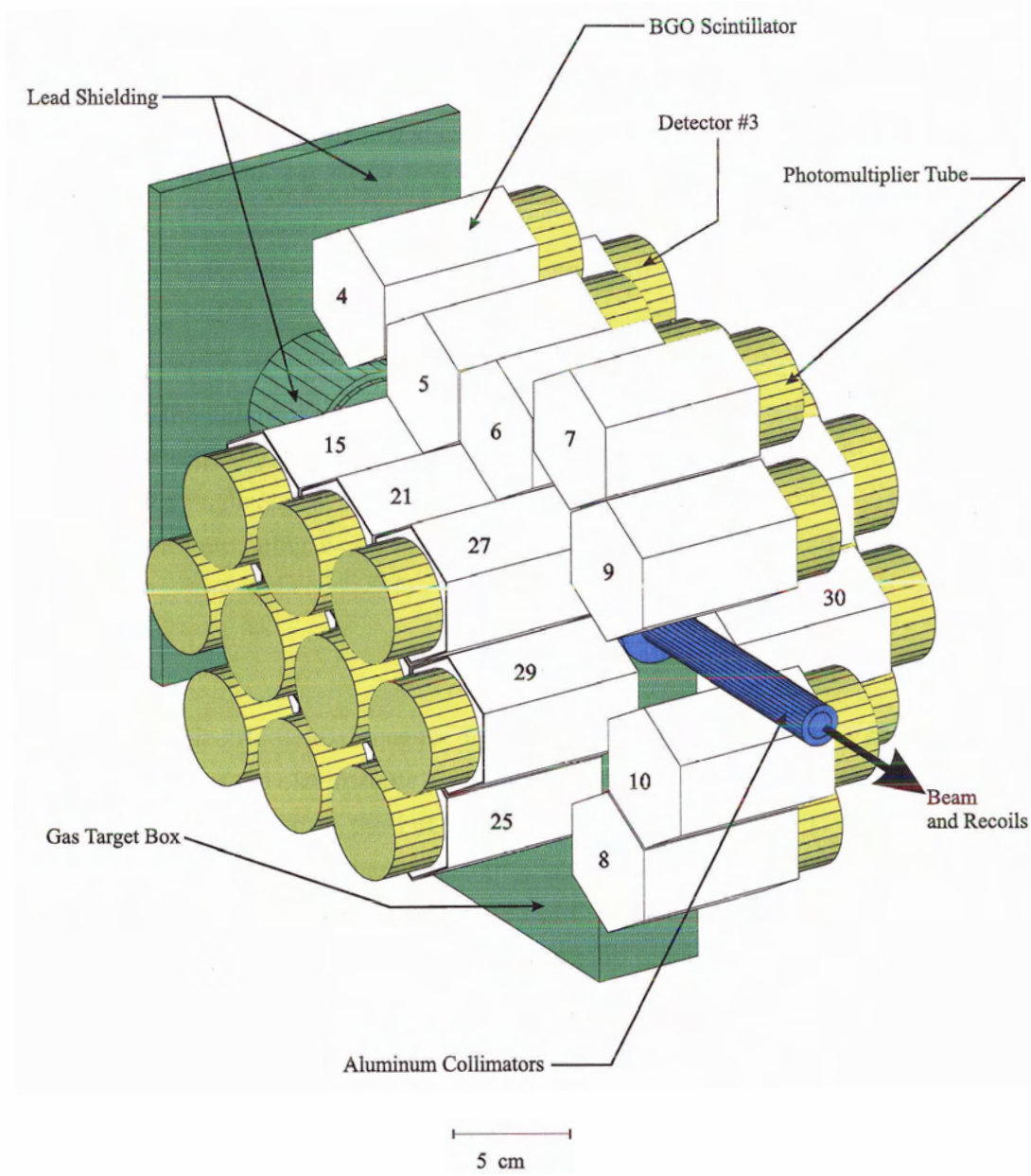


Figure 3.4: Technical drawing of the DRAGON BGO γ -ray detector array.

The DRAGON mass separator consists of two stages of magnetic dipoles (M), magnetic quadrupoles (Q), magnetic sextupoles (S), and electrostatic dipoles (E), arranged in the order (QQMSQQQSE)(QQSMQSEQQ), and magnetic steerers for fine tuning.

Under ideal conditions, the first stage should suppress the beam entirely. Recoiling ions and beam ions exit the gas target in a distribution of charge states [40, 41]. A magnetic dipole separates ions according to their magnetic rigidity,

$$Br = mv/q, \quad (3.1)$$

where m , v , and q are the mass, velocity, and charge of the ion respectively, B is the magnetic field, and r is the radius of curvature of the path of the ion in the field. Since the beam and recoils have essentially the same momentum, mv , placing slits downstream of the magnetic dipole allows a single charge state (usually the most probable for recoil ions) to be selected. By passing the remaining beam and recoil ions through an electric dipole, they can be separated according to their electric rigidity,

$$Er = mv^2/q, \quad (3.2)$$

where E is the electric field. Since recoil ions have a lesser kinetic energy, $\frac{1}{2}mv^2$, placing slits downstream of the electrostatic dipole allows recoil ions to be selected.

However, the vacuum in the DRAGON separator is of order 10^{-6} torr to 10^{-7} torr and beam ions may undergo charge changing interactions with residual gas or with a solid surface which destroys the perfect separation of the first stage of DRAGON. Hence, there is the need for a second stage with another magnetic dipole and electric dipole to further separate recoil ions from beam ions. The DRAGON mass separator has been shown to suppress 10^{10} beam particles for each one that it transmits [17].

3.1.5 Focal Plane Detection Systems

DRAGON requires a focal plane detector at the end of the separator whose main function is to detect the recoiling reaction products. Despite two stages of electromagnetic separation, it has been observed that a small number of “leaky” beam ions are able to traverse the separator in some experiments [17]. Therefore, it is necessary to employ detection systems that are able to discriminate between recoil ions and beam ions.

Discrimination between recoil ions and beam ions can be accomplished in several ways. First, the beam and recoils differ in kinetic energy, therefore a detector with sufficient energy resolution can separate the two. Second, the beam and recoils have nearly the same momentum but different mass. Therefore their velocity is different and a local time of flight measurement over 1 m can reveal the identity of an ion if the timing resolution of the detectors employed is sufficient. Typical times-of-flight through the 21 m separator are between 1 μ s and 5 μ s. The difference in time-of-flight between beam and recoils is typically hundreds of nanoseconds. Therefore most experiments require nanosecond timing resolution to use this method locally. Third, the transverse position of ions detected at the end of DRAGON may reveal their identity since the optics can be tuned to demand that recoils hit the end detector in a particular spot. Finally, recoil ions and beam ions have different mass, energy and nuclear charge [42]. Therefore they have unique signatures in their energy loss and charge production in a detector. DRAGON has at its disposal four types of detectors for performing the above measurements [43]: a gas ionization chamber, a parallel grid avalanche counter, a double sided silicon strip detector, and a position sensitive timing detector.

Gas Ionization Chamber

The DRAGON gas ionization chamber (figure 3.5) is a hollow cylinder filled with about 10 torr of iso-butane gas. Beam and recoils enter the chamber through a thin window at one end of the cylinder. Inside the chamber reside a cathode plate and a segmented anode consisting of 5 plates to measure the energy loss profile of ions. Between the anode and the cathode is a Frisch grid which is held at an intermediate voltage. All plates are in a plane parallel to the ion trajectory. Ions are constrained by the beam-line and beam optics to enter the chamber between the cathode and the Frisch grid. A similar ionization chamber is described in reference [44].

The amount of charge produced in this gas ionization chamber is proportional to the energy of the incident ion. If the signal is taken across a resistor between the anode and the Frisch grid, then its amplitude is proportional to the charge produced and, hence, to the energy of the incident ion. In this manner an energy resolution of 2 % to 5 % can be achieved. This resolution alone is not sufficient to separate beam from recoils in low energy experiments.

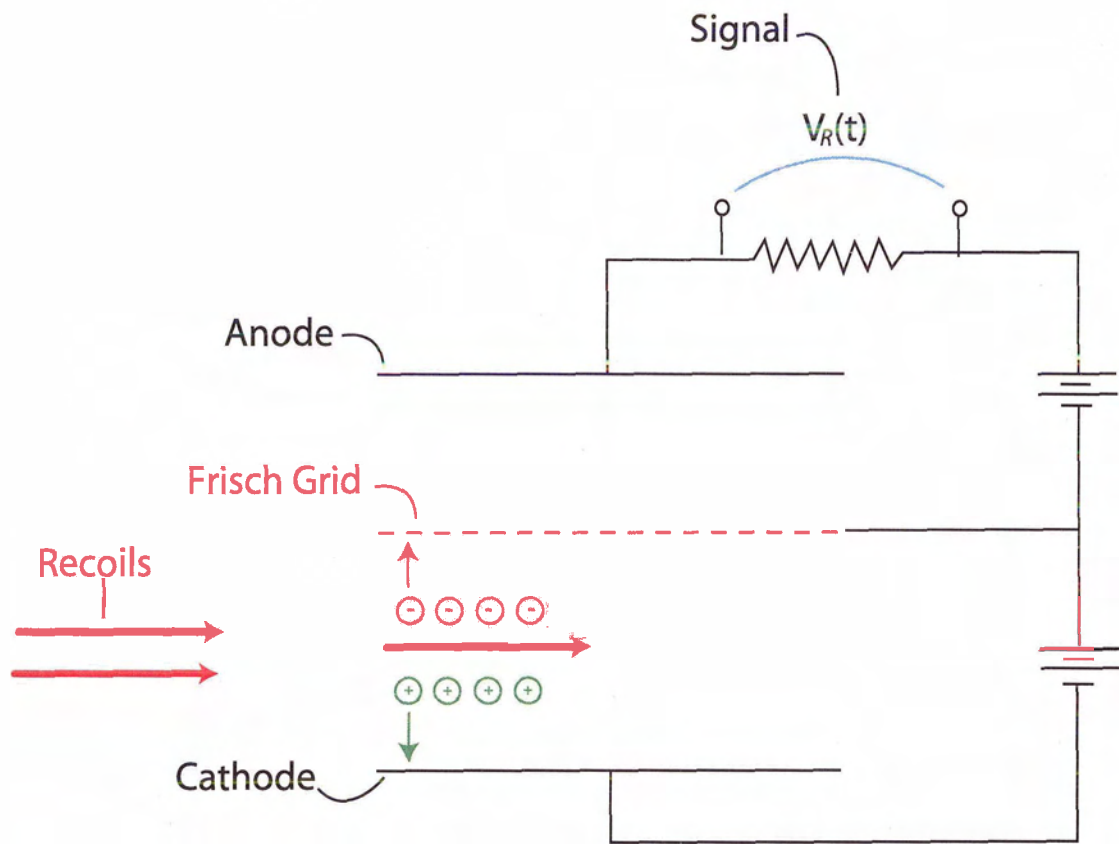


Figure 3.5: Schematic of the DRAGON iso-butane ionization chamber.

In all experiments, the beam and recoil ions have different energy, mass and nuclear charge. Segmentation of the anode allows the comparison of energy lost by nuclei in individual portions of the chamber. Using this information together with the total energy may be sufficient to discriminate between beam particles and recoil particles. It was shown in 2002 that the DRAGON ionization chamber is capable of separating beam ions from recoils in the case of the stable beam reaction $^{20}\text{Ne}(p,\gamma)^{21}\text{Na}$ at a beam energy of 0.5 MeV/amu. It is planned to use the ionization chamber for a study of the radioactive beam reaction $^{19}\text{Ne}(p,\gamma)^{20}\text{Na}$ in 2003 [45].

Parallel Grid Avalanche Counter

The DRAGON ionization chamber alone gives no information on the transverse position of entry of beam and recoils, and is capable of only coarse timing resolution. For these reasons, a parallel grid avalanche counter (PGAC) is employed [46, 47, 48]. The PGAC is a derivative of the more commonly used multi-wire proportional chamber [49, p. 190] and the parallel plate avalanche counter [49, p. 188]. It consists of an anode grid sandwiched between two cathode grids, all normal to the beam axis and mounted just inside the ion chamber window, as shown schematically in figure 3.6. The anode is held at a sufficiently high voltage so that free electrons produced in the iso-butane gas by a passing ion induce an electron avalanche as they approach an anode wire, giving a timing signal of resolution 1 ns. The electron avalanche induces a signal on the cathode wires also. Since the wires of the two cathodes are oriented orthogonally with respect to one another, the transverse position of the passing ion can be deduced in two dimensions. The cathode wires are connected to a delay line at 2 ns intervals. Signals are read out from each end of the cathode and subtracted in time to determine the position of transmission of the ion, reducing the number of channels to two per cathode plane.

Double Sided Silicon Strip Detector

Only one of these four focal plane detectors has been used in radioactive beam experiments. It is a position sensitive semiconductor diode detector; a double sided silicon strip detector (DSSSD). This detector provides 1 % FWHM energy resolution, 1.2 ns timing resolution, 3 mm position resolution, and a modified version has the potential to be used for pulse

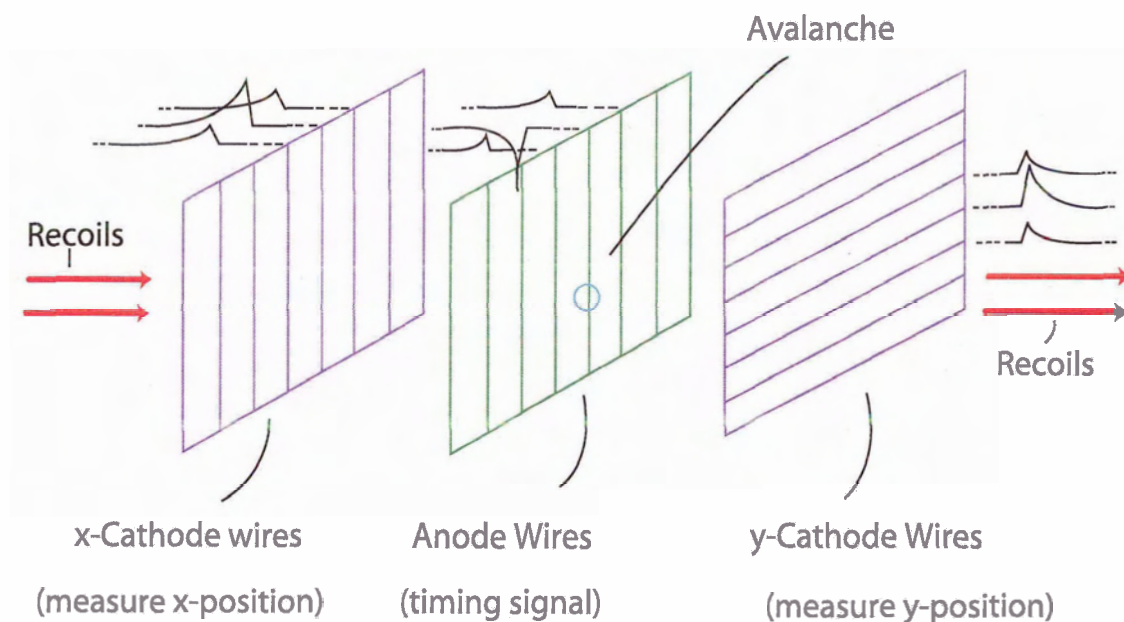


Figure 3.6: Schematic of the DRAGON parallel grid avalanche counter.

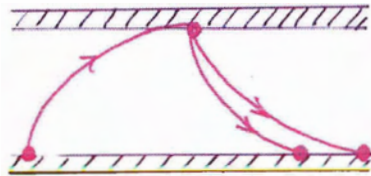
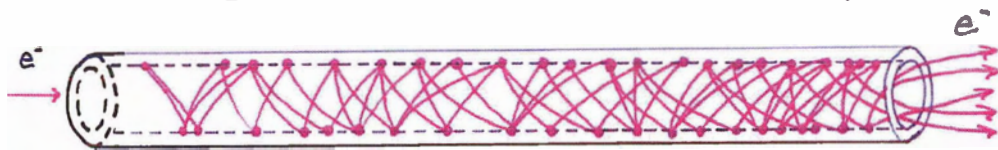
shape analysis yielding ion species identification. A DSSSD was used successfully with DRAGON in measurements of the strengths of several resonances in the $^{21}\text{Na}(p,\gamma)^{22}\text{Mg}$ reaction in 2002 [36, 37]. The DRAGON DSSSD is the subject of this thesis and it is described extensively, beginning in the next chapter.

Micro-Channel Plate Detector

A micro-channel plate (MCP) is a position sensitive electron multiplier with excellent timing characteristics [50]. The DRAGON MCPs consist of a lead glass plate of 0.5 mm thickness, punctured with an array of capillaries of 10 μm diameter that act as continuous channel electron multipliers when there is a electric potential difference applied from one side of the plate to the other, as shown in figure 3.7. The compact geometry of the capillaries provides MCPs with excellent timing resolution. MCPs may be installed in series to provide further electron multiplication, as shown schematically in figure 3.7.

A resistive anode may be used to detect electrons exiting an MCP [51]. By taking signals from the four corners of a square anode and comparing their magnitude, the position of the incident electron can be deduced.

• Continuous Channel Electron Multiplier



• MCP electron multiplication and detection

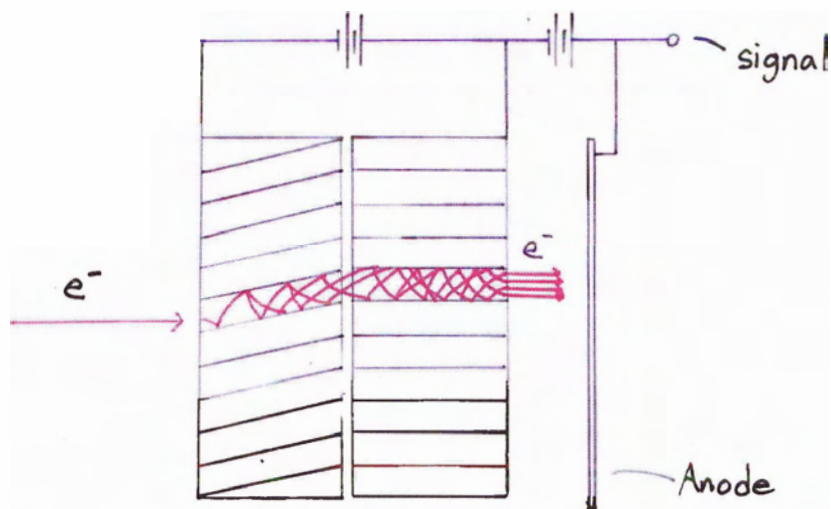


Figure 3.7: Schematics of a continuous channel electron multiplier and two micro-channel plates in a chevron configuration in front of a resistive anode.

DRAGON uses an MCP to detect secondary electrons produced when a beam or recoil ion passes through a thin carbon foil [52]. The foil is normal to the path of the ions, and the secondary electrons produced can be reflected electromagnetically to an MCP positioned out of the beam axis, as shown in figure 3.8. The DRAGON MCP setup employs two MCPs in series to give sub-nanosecond timing resolution and a resistive anode to produce an image of the transverse position of transmission of the detected ions. These components together form a position sensitive timing detector (PSTD) which is installed approximately 1 m upstream of the end detector (either the ionization chamber and PGAC or DSSSD), and provides a start signal for time-of-flight measurements with the stop signal provided by either the PGAC or DSSSD. The PSTD may also be used to determine the trajectory of ions when they are detected in coincidence with these position sensitive end-detection devices.

Utility of Focal Plane Detectors

These four focal-plane detection systems can be used in a variety of combinations for particle identification on DRAGON. Three potentially useful combinations in order from upstream to downstream from left to right are:

1. PSTD-DSSSD
2. PSTD-PGAC-Ionization Chamber
3. PSTD-PSTD-End Detector.

The combinations are shown schematically in figure 3.9. The first combination provides a local time-of-flight measurement over a 1 m flight path between the PSTD and DSSSD, position resolution of 3 mm, and energy resolution of about 1 %. The second combination provides a local time-of-flight measurement between the PSTD and PGAC, sub-millimeter position resolution, and ΔE -E information. The third combination exploits the excellent timing resolution of MCP systems to measure a local time-of-flight between two PSTDs, with either a DSSSD or the ionization chamber as an end detector.

To date, only the DSSSD has been used in DRAGON experiments, and it has worked well to distinguish between beam and recoil particles, by energy resolution alone in some cases, and in coincidence with prompt γ -rays detected by the BGO array [36, 17, 37]. The

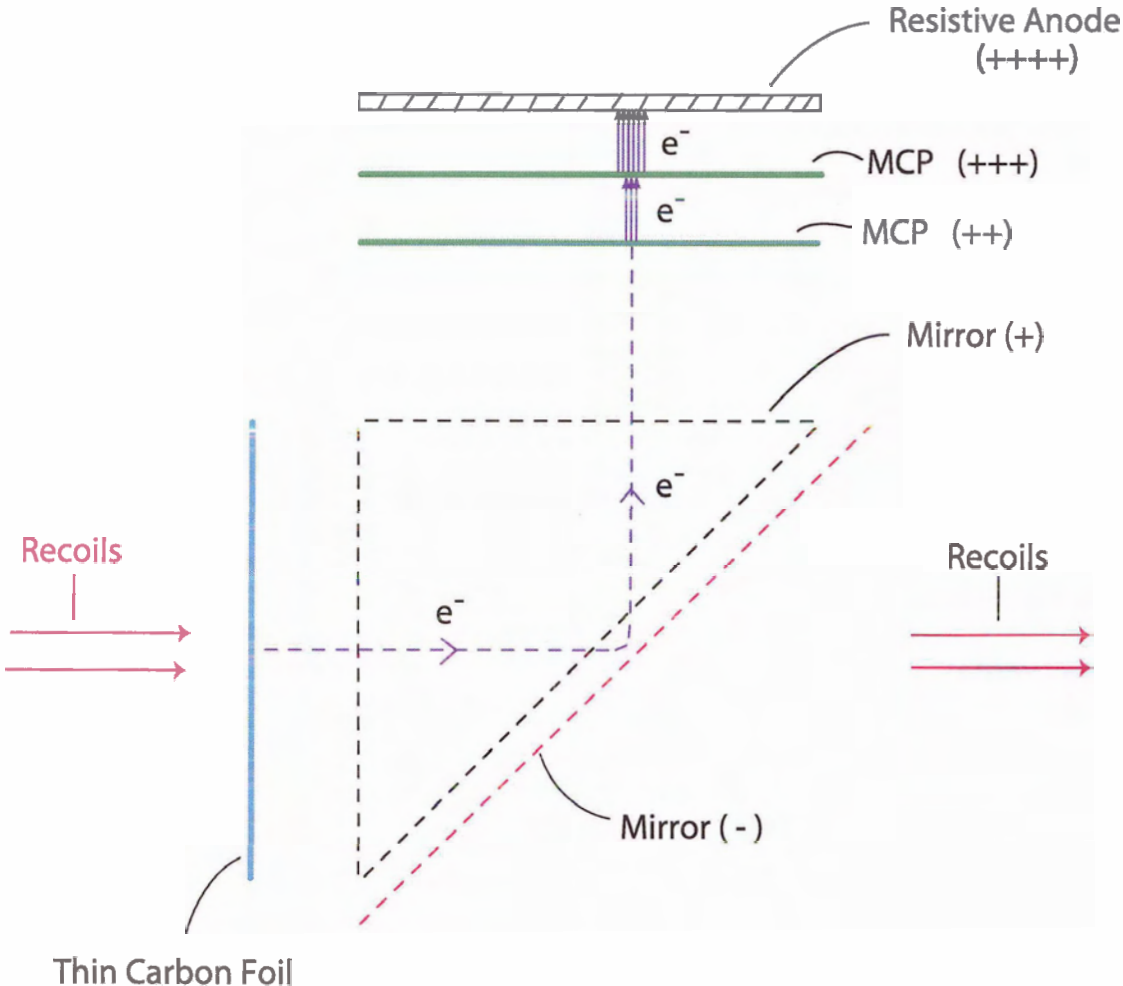


Figure 3.8: Schematic of the DRAGON position-sensitive timing detector.

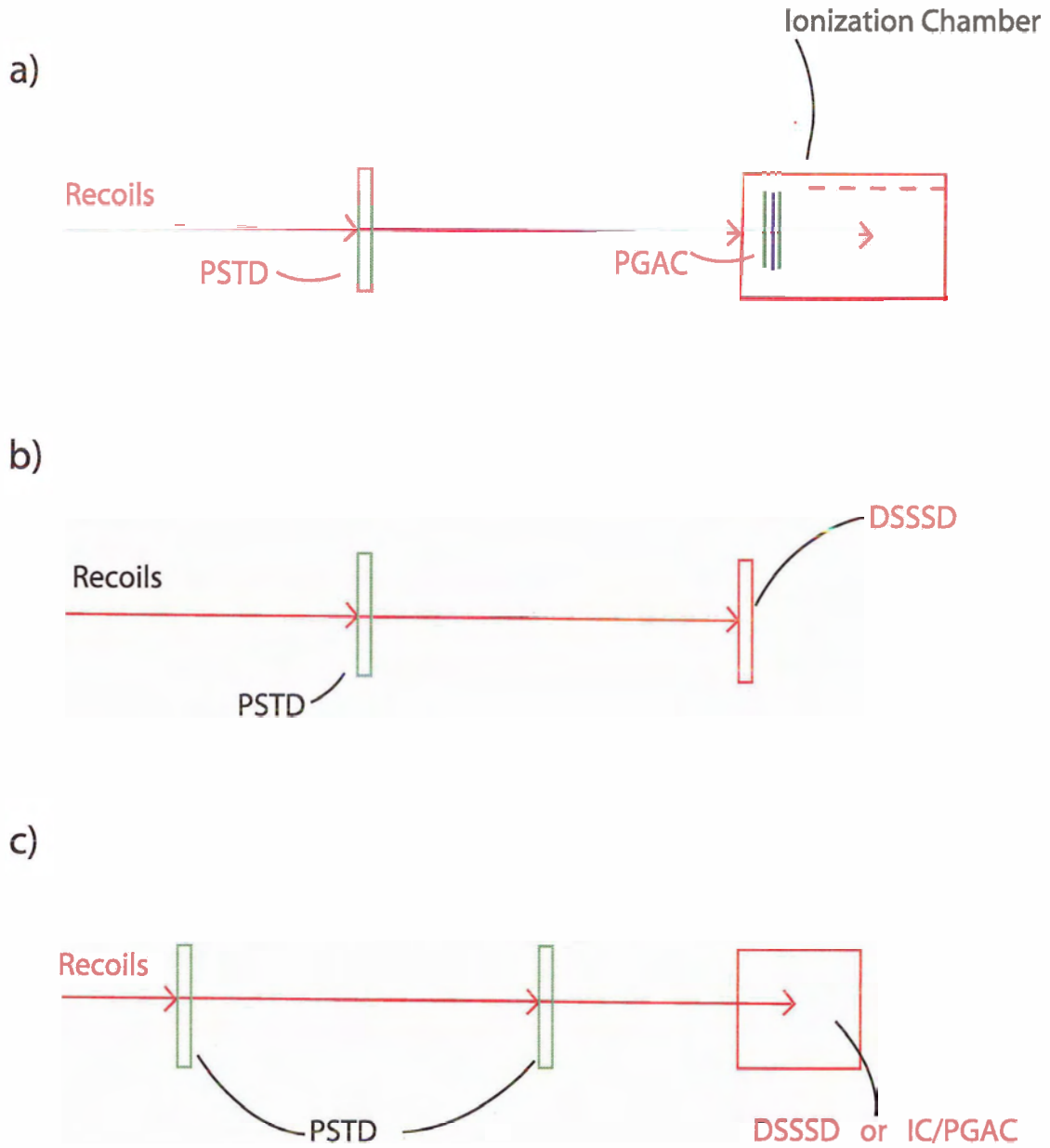


Figure 3.9: Possible focal plane detector arrangements: a) PSTD-DSSSD, b) PSTD-PGAC-Ionization Chamber, and c) PSTD-PSTD-End Detector.

PSTD is installed and is in testing [53]. The PGAC has been tested off-line and is ready for installation [48]. The ionization chamber, as mentioned, has been tested online twice with stable beam resonances. It requires minor fine-tuning before its employment in a radioactive beam experiment.

Chapter 4

The DRAGON DSSSD

4.1 Semiconductor Diode Detectors

The research for this thesis is on the DRAGON DSSSDs, the segmented semiconductor diode detectors that have been used as DRAGON end detectors. Before discussing the research, it will be instructive to briefly review the principle of operation of these detectors. A more complete description of the band theory of solids [54, ch. 7], semiconductors [55], and the use of semiconductor detectors for detection of ionizing radiations [49, ch. 11] [56, ch. 10] can be found in standard textbooks on these subjects.

4.1.1 Band Theory of Solids

Free atoms have shells with relatively well defined electronic energy levels. When atoms are packed closely as in a solid, the energy levels broaden into bands due to the interaction with surrounding atoms. This broadening is most pronounced in the outer shells, since the electron-nucleus interaction is weakest here. Loosely bound electrons reside in the highest energy band, or conduction band, where they are not bound to specific nuclei. The other electrons are in a lower energy band, the valence band, where they are bound to lattice nuclei. The space between the valence band and the conduction band is called the band gap.

At absolute zero, electrons fill up the lowest available energy states. Since electrons are Fermions and obey the Pauli exclusion principle, they cannot all exist in the lowest energy

state. Accordingly, the electrons fill all available states up to an energy called the Fermi energy. If the conduction band and valence band overlap, then there are unoccupied states available for electrons to move to under the influence of an electric field and the material is a conductor. If the Fermi energy lies within a forbidden gap, then the material is either an insulator or a semiconductor, depending on the energy required to excite an electron from the valence band to the conduction band. If the required excitation energy is above about 5 eV then the material is an insulator, and if the excitation energy is around 1 eV then the material is a semiconductor.

4.1.2 Semiconductors

Electrical conductivity of materials varies over many orders of magnitude. At opposite extremes of electric conductivity are conductors and insulators. Somewhere in between lie semiconductors. A semiconducting material is often a crystal of tetravalent atoms like silicon or germanium, meaning that each atom has four electrons in its valence shell which may form covalent bonds with neighboring atoms.

If a pure tetravalent crystal is doped with a small amount of pentavalent material like phosphorus then each phosphorus atom contributes a loosely bound electron to the material, which resides in a discrete energy level barely below the conduction band (0.05 eV below for silicon), and can be easily excited to the conduction band and transported through the material by an electric field. Such a material is called an *n*-type semiconductor because it contributes to the conductivity with loosely bound, *negatively* charged electrons as the majority charge carriers.

Conversely, if a tetravalent material is doped with trivalent atoms like boron, then vacancies in the crystal lattice are formed in a discrete energy level barely above the valence band, into which electrons from the valence band can be easily excited and transported through the material under the influence of an electric field, creating new vacancies. If the electrons move collectively in one direction, then the vacancies are seen to move in the opposite direction. The vacancies are called “holes” and can be treated as equivalent to electrons but with opposite charge, and slightly different mobility. Such a material is called a *p*-type semiconductor because it contributes to the conductivity through the filling of holes by electrons, with *positively* charged holes as the majority charge carriers.

In a p -type semiconductor, there exist small number of negative charge carriers. Conversely, in an n -type semiconductor, there exist a small number of positive charge carriers. The number of these minority carriers is strongly temperature dependant.

A heavily doped n -type semiconductor is referred to as n^+ and a heavily doped p -type semiconductor is referred to as p^+ .

4.1.3 The $p - n$ Diode Junction

Let us imagine a p -type semiconductor brought into contact with an n -type semiconductor. Across the junction occurs a diffusion of electrons from the n -type semiconductor to fill the holes in the p -type semiconductor. Conversely, holes migrate from the p -type to the n -type semiconductor. This diffusion induces equal and opposite charges on the two materials. The charges cause an electric field which eventually opposes the further diffusion of charge across the junction. The region containing the electric field is depleted of charge carriers and is appropriately called the depletion region.

If a forward bias (a bias in the direction that decreases the existing electric field) is applied to the junction, say via a power supply and electrodes, then the depletion region contracts and a large current flows across the junction. The current increases rapidly with applied voltage.

If a reverse bias (a bias in the direction that increases the existing electric field) is applied to the junction, then the extent of the depletion region is increased. At a high enough voltage, the depletion region extends over the entire volume of the crystal. In this situation, the junction is said to be fully depleted. Up to a certain voltage there exists only a small leakage current across the junction due to thermally generated minority charge carriers, so the junction can be over-depleted if need be. However, there exists a break down voltage above which the current increases rapidly due an avalanche effect from impact ionization of electron-hole pairs. The break down voltage is temperature dependent, a colder detector can sustain a higher reverse bias field than a warmer one. The current-voltage characteristics of diodes are summarized in figure 4.1.

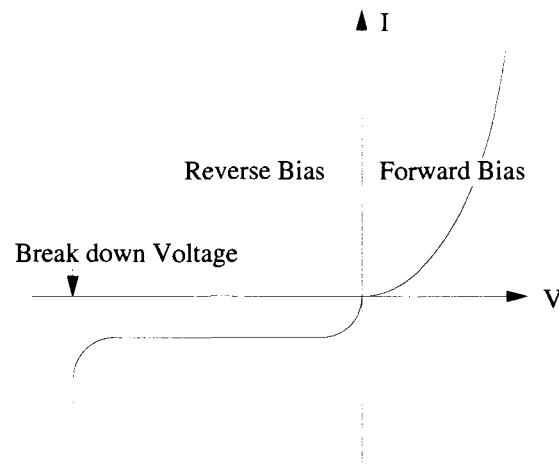


Figure 4.1: Diode current-voltage characteristics. The $-V$ scale is compressed and the $-I$ scale is expanded to show more detail.

4.1.4 Reverse Biased $p-n$ Junction as a Radiation Detector

A reverse biased $p-n$ junction may be used as a detector of ionizing radiation. For example, a charged particle passing through the depletion region of a $p-n$ junction produces electron-hole pairs in a column of plasma around the path of the particle. If the reverse bias is high enough then the electron-hole pairs are swept up quickly and efficiently by the electric field, giving a pulsed electric signal with an amplitude that is proportional to the energy of the incident radiation if the radiation stops in the depletion region of the detector.

The average energy needed to produce an electron-hole pair in silicon is 3.6 eV, compared to 20 eV – 40 eV in gas-filled detectors. The statistical advantage of having more ion pairs per incoming particle contributes to the relatively good energy resolution of silicon detectors.

4.1.5 Position Sensitive Diode Detectors

A simple silicon detector provides a spatial resolution no better than the size of the detector itself. However, it is possible to segment one (or both) of the electrodes into independent strips. If one electrode has parallel strips in one direction, and the other one has strips

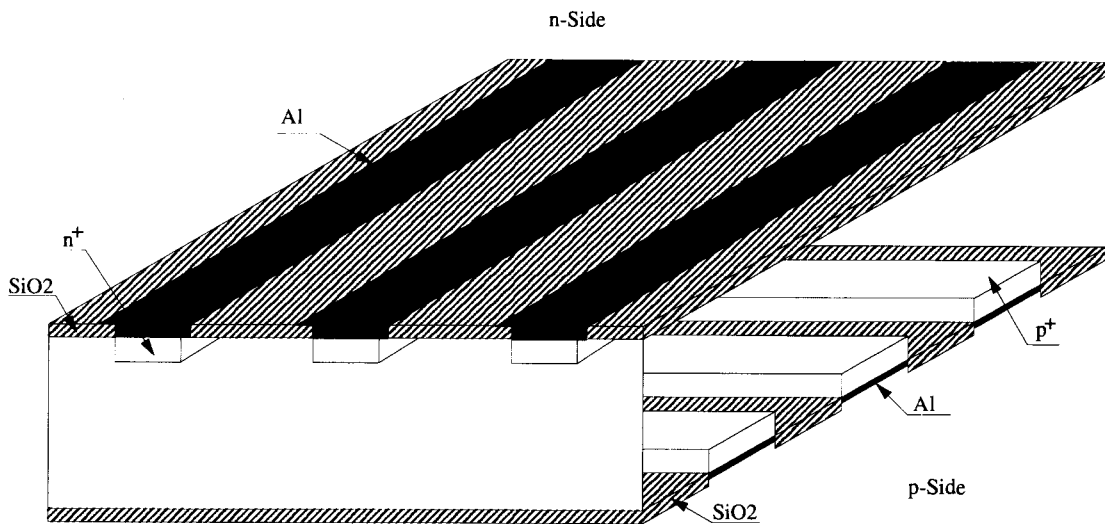


Figure 4.2: The geometry of a double sided silicon strip detector.

orthogonal to these, then the detector is divided into $l \times m$ segments, where l and m are the number of strips on the front and back of the detector respectively (figure 4.2). When an electron-hole pair is produced, they migrate to the nearest anode and cathode strips respectively, producing two coincident signals which can be recognized as a single event at a particular position on the detector. Such a detector is used with DRAGON and is commonly referred to as a double sided silicon strip detector (DSSSD).

4.2 The DRAGON DSSSD Test Station

A test station for the DRAGON DSSSDs and related electronics and data acquisition hardware and software was assembled and tested in TRIUMF's detector facility ¹. The working system was moved to ISAC and integrated with the DRAGON electronics and data acquisition systems. The test station was later rebuilt with new hardware to allow for further off-line testing and improvements to the DSSSD system. The completely assembled test station is shown in figure 4.3.

¹The electronics and data acquisition systems were conceived by Dr. Ahmed Hussein, Professor of Physics, University of Northern British Columbia

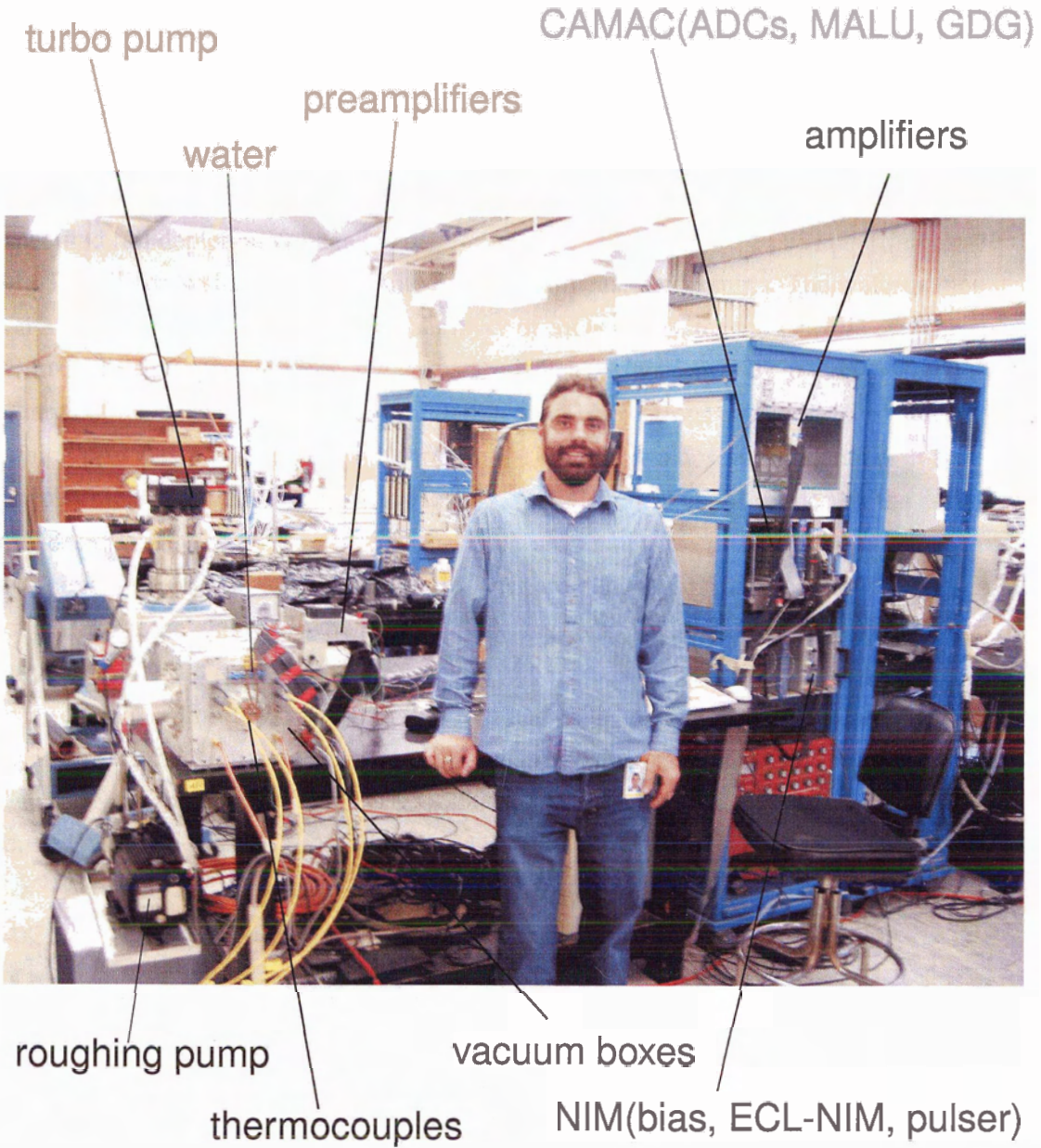


Figure 4.3: The DRAGON DSSSD test facility.

4.2.1 The DRAGON DSSSD

The Micron Semiconductor [57] Model W(DS)-250 DSSSD detector used with the DRAGON separator consists of 16 front strips (numbered 0-15) and 16 back strips (numbered 16-31), each of width 3 mm. This provides $256 \times 3 \text{ mm}^2$ pixels on the 5 cm^2 detector to encode x - y position. The gap between strips is specified to be $100 \mu\text{m}$ [57]. The thickness of the detector is $250 \mu\text{m}$. The detector can be biased between 30 V and 70 V; 50 V is a typically specified full depletion voltage [57].

The silicon wafer is ion-implanted and has dimensions 53 mm^2 . The wafer is mounted on a G-10 circuit board frame. A thin layer of SiO_2 passivates the DSSSD on both sides. On the n -side of the detector, the strips are isolated electrically by p -stops. The positive charge of the oxide attracts an accumulation layer of electrons on the surface of the silicon which provides a conductive path through the silicon; p -stops are implants of p -type material which break this conductive path [49, p.494] [58]. The electrodes on the surface of the detector are specified to be 300 nm thick aluminium [57]. Each strip is connected to the circuit board with fragile bond wires that are attached ultrasonically. The signals are output from the end of the board by 34 pin headers. Two of these are grounds, and are connected to gold plating that covers most of the backside of the circuit board. Figure 4.4 is a schematic of the DSSSD from the front and back, showing the connections of individual strips to their respective pin headers. Figure 4.5 is a photograph of the front side of a Micron Semiconductor Model W(DS)-250 DSSSD, the mount is the one currently installed on DRAGON.

4.2.2 Vacuum Systems

In the TRIUMF detector facility, the DSSSD is housed in a $24.1 \times 24.1 \times 24.1 \text{ cm}^3$ vacuum tight, light tight, stainless steel cubic box composed of a cubic frame with removable plates on all 6 sides. Gas pressure inside the box is read out by a Granville-Phillips 275 [59] convection gauge. Vacuum better than 10^{-4} torr, which is the minimum reading on the convection gauge, is achieved by a roughing pump and a turbo pump. It is well known that applying a bias to a DSSSD in the 100 mtorr gas pressure range can be damaging to the DSSSD, therefore pumping and venting should never be done with the DSSSD bias on.

The DRAGON DSSSD is housed in a vacuum box of identical dimensions with remov-

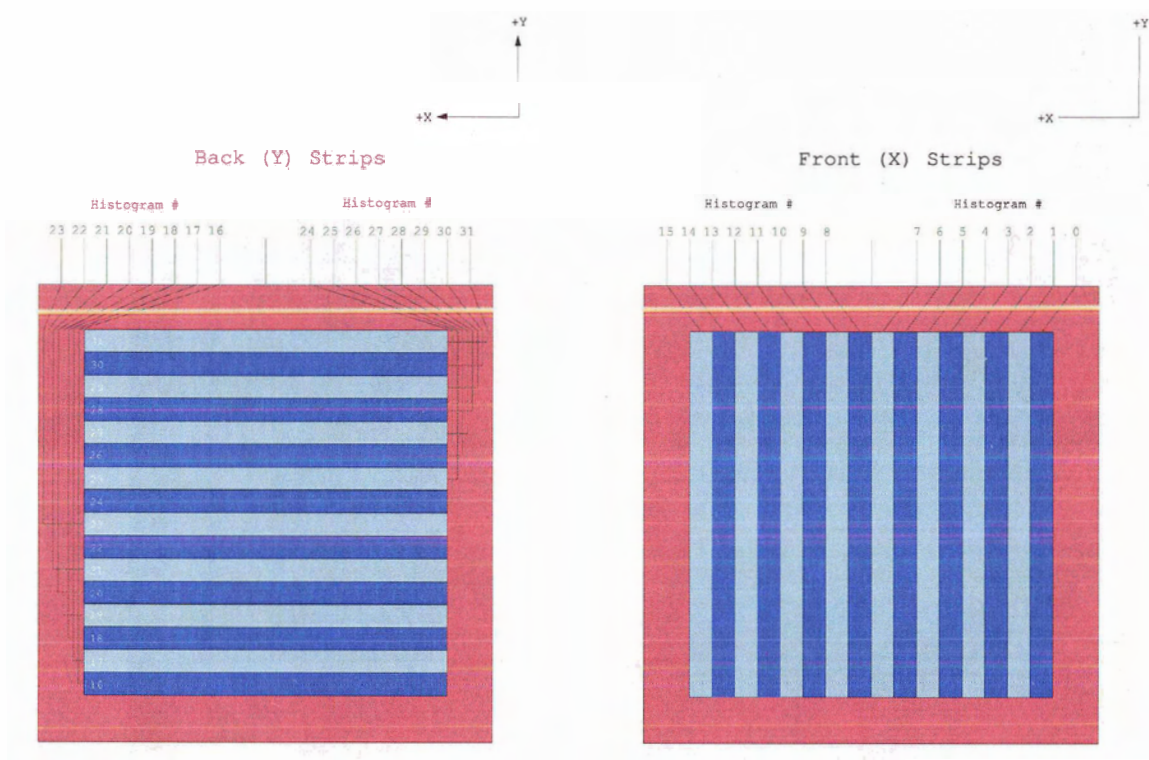


Figure 4.4: Schematic of electrical connections to DSSSD strips.

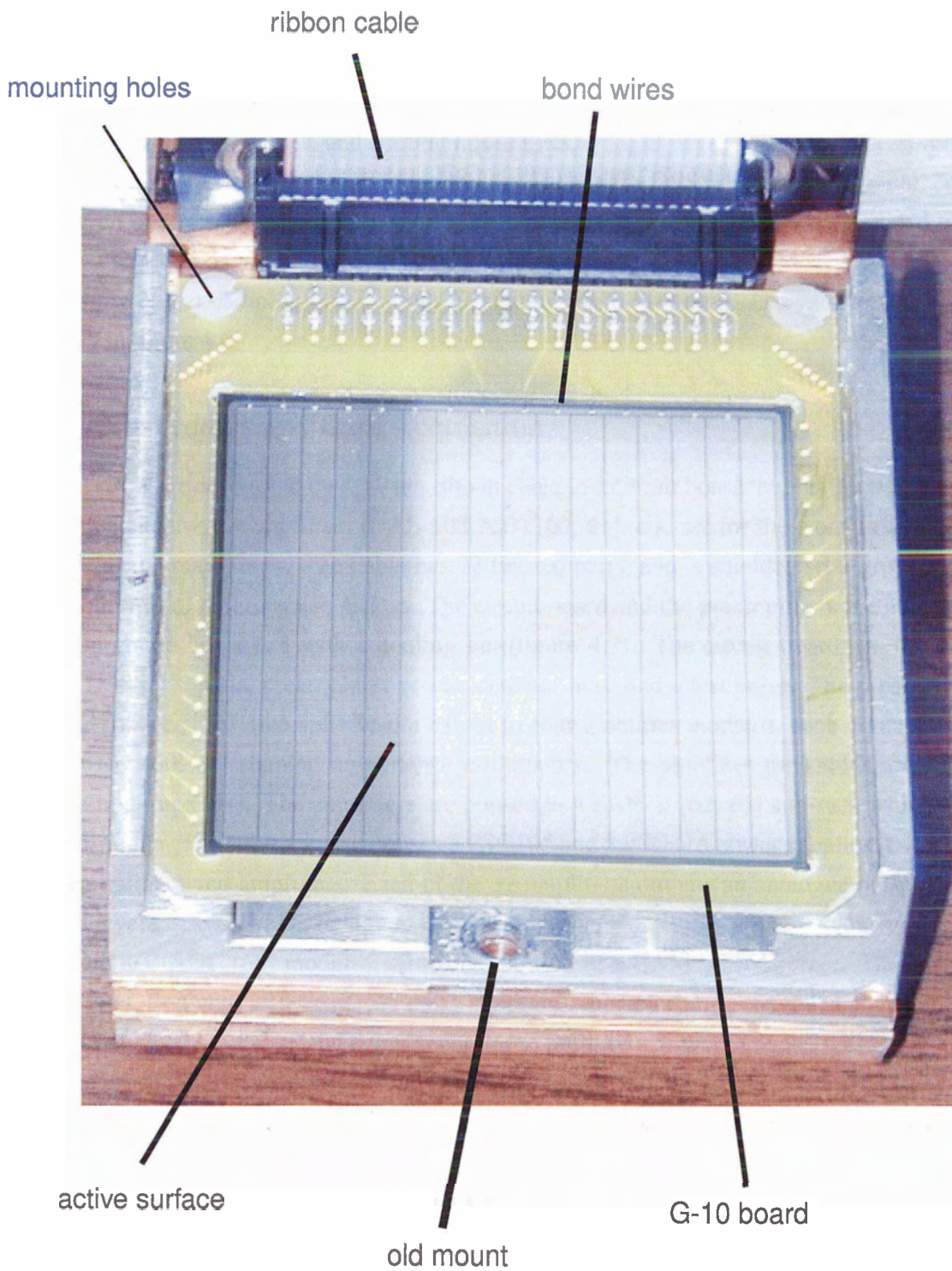


Figure 4.5: Micron Semiconductor W(DS)-250 DSSSD front view. Active surface is 5 cm \times 5 cm.

able plates compatible with those in the detector facility. Any feed-throughs for the DSSSD and related systems are fed through a single plate of the vacuum box for simplicity and compatibility with DRAGON. Feed-throughs include DSSSD bias and signals, thermoelectric cooler power, thermocouples, and cooling liquid lines.

It was found that the turbo pump introduced noise into the DSSSD when it was mounted directly on one side of the vacuum box. The vacuum system was therefore expanded to include a second box which accommodated the turbo pump. Doing so reduced the noise, presumably due to damping of vibrations originating from the pump. The vacuum system is shown in figure 4.6.

4.2.3 Electronics and Data Acquisition

DSSSD strips are connected by a 34-pin ribbon cable to a circuit board that holds two types of charge-sensitive preamplifiers (RAL 108 A,B) [60, 61], one set for the front strips and another for the back strips. The cable has 17 twisted pairs, and is shielded with grounded aluminium foil to reduce noise pickup. The circuit board and the preamplifiers are housed in an aluminum box fitted with a cooling fan (figure 4.7). The circuit board has inputs for the DSSSD signals, preamplifier power, detector bias, and a test pulse. The preamplifiers are connected by two split 34-pin cables to four amplifier modules, each containing 8 RAL 109 [60, 61] shaping amplifier/discriminators. The amplifier thresholds are adjustable in groups of 8. The amplifiers are housed in a KM6 II [62, 63] sub-rack which is cooled by a fan. The sub-rack also houses 3 PSG105 and 2 PSG115 power supplies [64] for the preamplifiers and amplifiers. Each of the 32 amplifiers outputs an analogue pulse and an ECL-level fast-discriminator signal. Each analogue signal is input directly to one of four Silena 4418/V ADC [65] modules, which are housed in a CAMAC [66] crate. The ECL signals are ORed with a LeCroy [67] 4532 logic unit, then converted to a NIM signal and fed to a LeCroy 2323A gate and delay generator to produce a 3 μ s ADC gate. MIDAS [68] software is used for data acquisition and PAW [69] is used to display data. Figure 4.8 shows the DSSSD electronics schematically, and figure 4.9 is a photograph of the electronics and data acquisition systems.

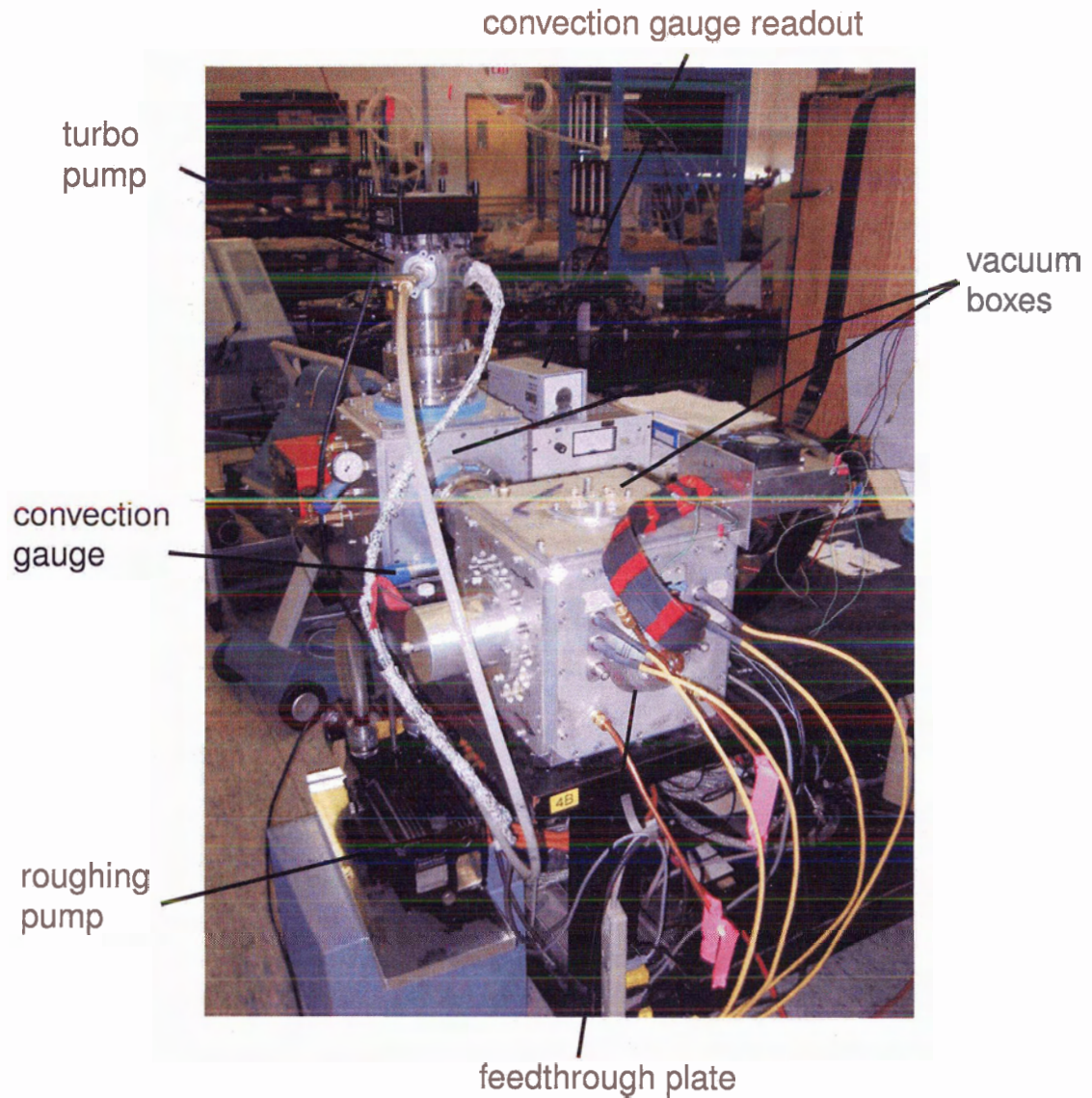


Figure 4.6: DSSSD test facility vacuum system.

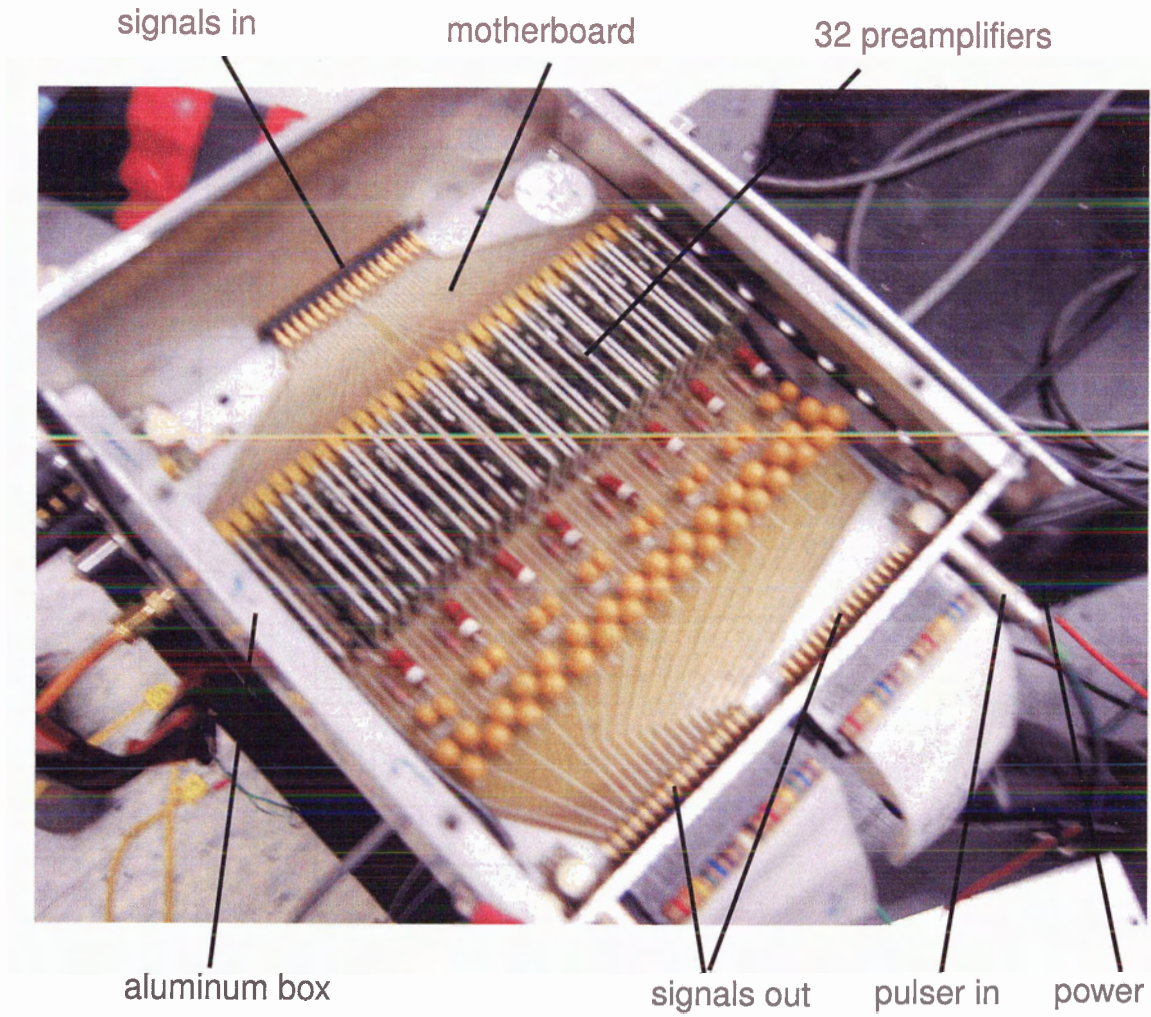


Figure 4.7: RAL 108A,B preamplifiers in place.

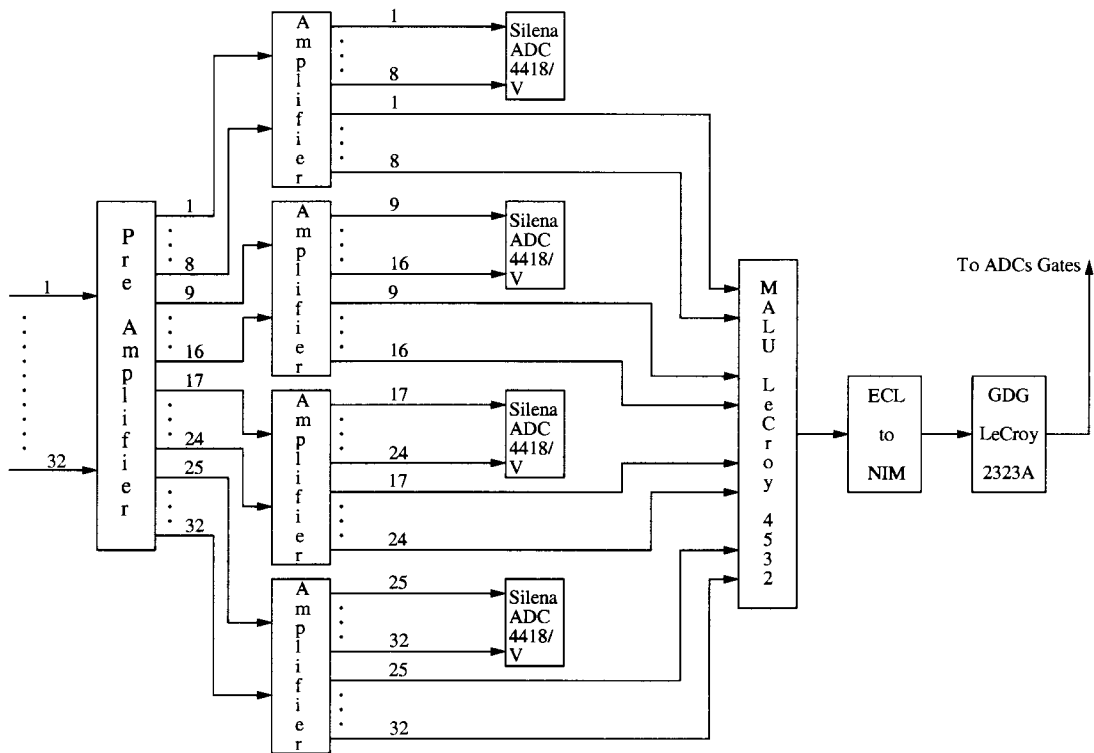


Figure 4.8: The DRAGON DSSSD test station electronics.

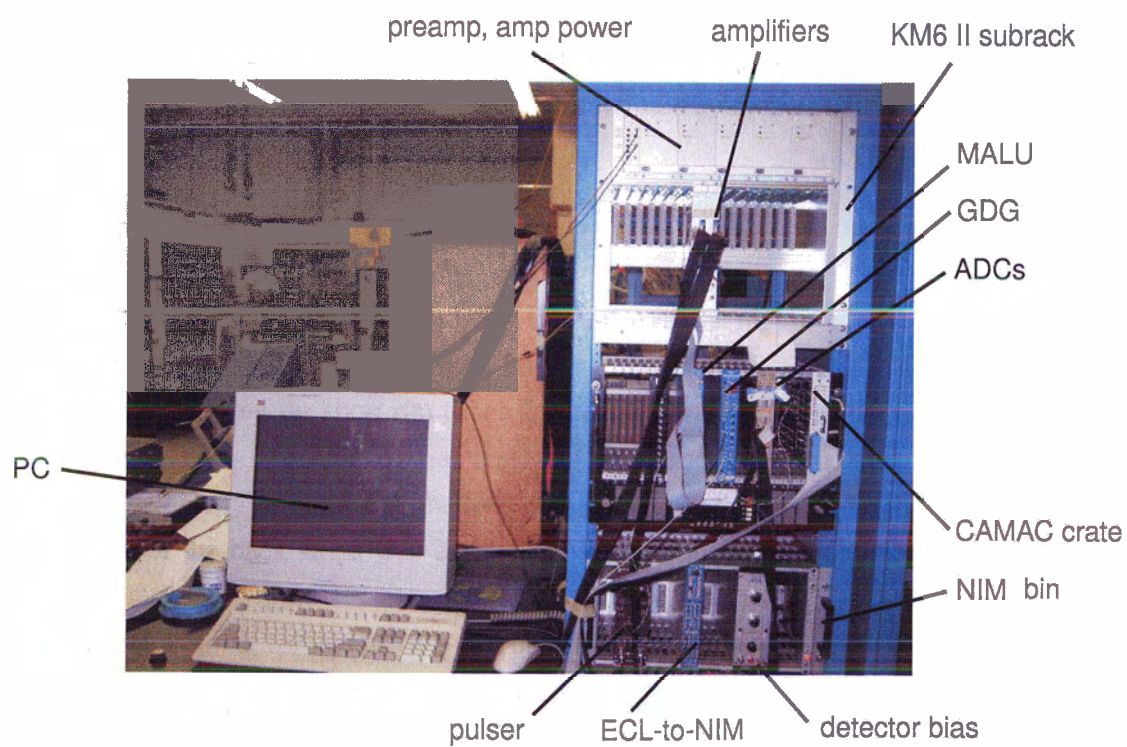


Figure 4.9: DSSSD test facility electronics and data acquisition.

Chapter 5

DSSSD Testing and Calibration

5.1 Energy Resolution

The energy resolution of individual DSSSD strips was first measured using a 10 μCi ^{241}Am source placed 20 cm from the DSSSD, flooding the it with α -particles. The 10 μCi source was strong, allowing for short run times, but relatively thick which degraded the observed energy resolution. The DSSSD was biased at 50 V and 30 000 counts per strip were acquired. The energy resolution of the front strips was found to be 1.2 %–1.4 % FWHM. The resolution of the back strips was 2 %–3% FWHM, with some anomalous strips showing poor resolution.

Raising the bias voltage to 70 V did not affect the energy resolution of the front strips. The energy resolution of the back strips improved to 1.5 %–2.0%. Some back strips, particularly the edge ones, showed poorer energy resolution.

A thinner 15 nCi ^{241}Am source was used to repeat the experiment with 70 V bias. Strips received 40 000 counts on average. In this case, the resolution of the front strips was 0.7 %–0.9% FWHM. Resolution of back strips was 1.0 %–1.4% FWHM. Resolution data are shown in table 5.1. These measurements were taken at the DSSSD test station using electronics that are now integrated with DRAGON. With the current apparatus at the test station, resolution better than 0.7 % for front strips has been measured with several brand new DSSSDs. The intrinsic line width of the source may still contribute a significant width to these measurements.

Table 5.1: Energy resolution of individual strips for 5.486 MeV α -particles.

Strip Number	Energy Res. (FWHM) (%)
0	0.95
1	0.88
2	0.88
3	0.93
4	0.89
5	0.89
6	0.87
7	0.78
8	3.53
9	2.45
10	0.76
11	0.81
12	0.74
13	0.77
14	0.73
15	0.78
16	2.71
17	1.43
18	1.29
19	1.16
20	1.48
21	1.12
22	1.37
23	1.29
24	1.10
25	1.30
26	1.10
27	1.02
28	1.25
29	1.70
30	1.23
31	1.78

5.2 Relative Efficiency of Strips

To test the relative efficiency of strips, a long run was performed with the stronger ^{241}Am source fixed 20.0 ± 0.5 cm from the DSSSD without collimation. The projections of the 2-D position histograms, displayed in figures 5.1 and 5.2, show that the strips are close to the same relative efficiency with the exception of the edge strips. Solid angle effects cause the slight curvature of the distributions; the expected distributions with geometry taken into account are denoted by black crosses in the figures.

5.3 The Pulse Height Defect

Heavy ions produce a signal of smaller amplitude than light ions of the same energy in a silicon ionization detector because of the way that they lose energy in materials [70]. The pulse height defect is the difference between the energy of an incident ion and its apparent energy indicated by the pulse height output by a detector calibrated with light ions, usually α -particles. Three factors contribute to the pulse height defect: The window defect, the nuclear stopping defect, and the residual defect.

5.3.1 The Window Defect

The DRAGON DSSSD is furnished with a thin window of aluminum, for electrical contact, and SiO_2 to passivate the DSSSD. DRAGON has its DSSSDs manufactured with especially thin windows since the energy loss of heavy ions in the energy range 0.15 MeV/u to 1.5 MeV/u is expected to be significant in the window of the detector. A thin region also exists near the surface of the bulk semiconductor in solid state radiation detectors to which the depletion region does not extend. This region is known as the “dead layer” [49, p. 377] since ionization produced in this region is not collected by the detector. The window defect results from incident ion energy lost in the window and dead layer of the detector.

The combined thickness of the window and dead layer was determined for DSSSD 2239-3¹ by measuring the pulse height produced by α -particles incident on the DSSSD at

¹See table 6.4 for an inventory of the DRAGON DSSSDs.

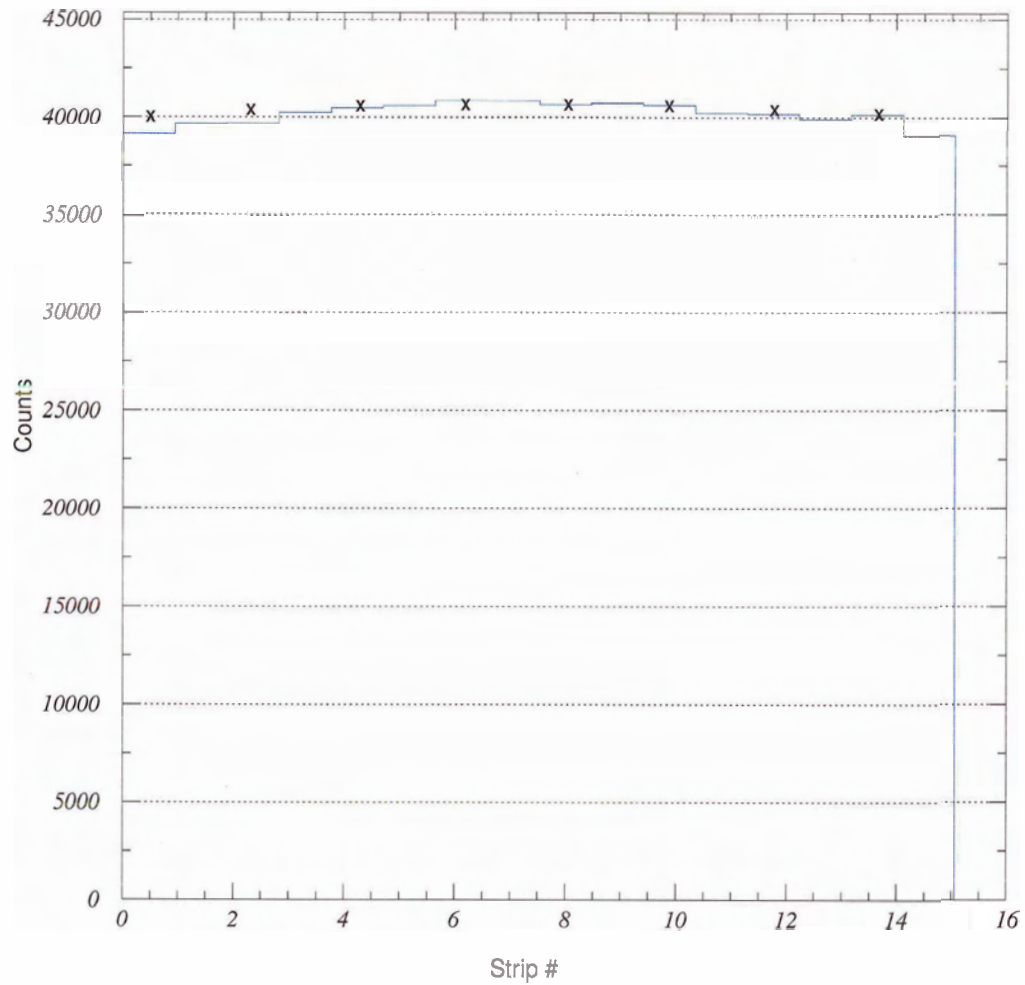


Figure 5.1: Projection of front strips with an un-collimated 5.486 MeV α -particle source.

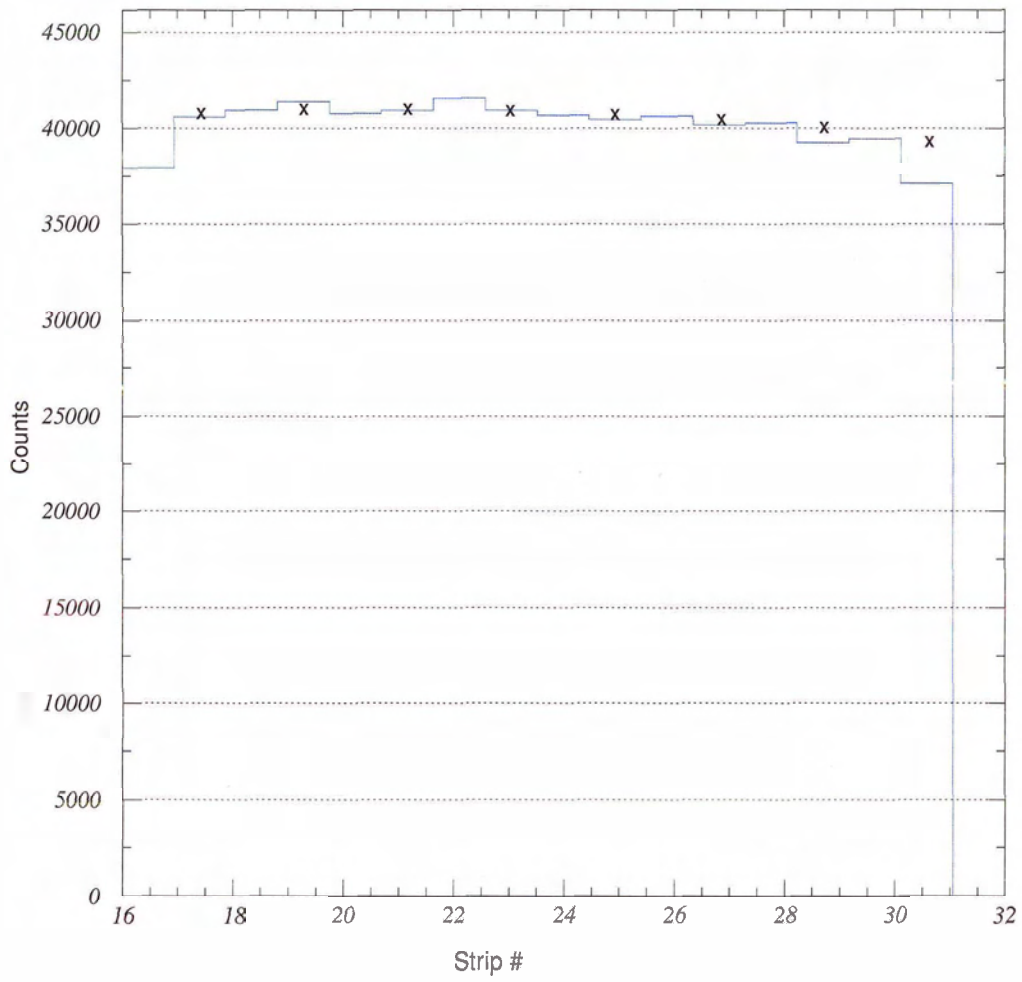


Figure 5.2: Projection of back strips with an un-collimated 5.486 MeV α -particle source.

angles of 0° , 45° , and 60° to the normal. At each angle, the bias voltage was varied to test the effect of DSSSD bias on the thickness of the dead layer.

Varying the bias revealed that the combined thickness of the window and the dead layer is constant as a function of bias. This suggests that the front dead layer thickness is constant above 30 V bias, since the window thickness is certainly constant.

Four independent measurements of the window thickness were done, each at different bias. The data are shown in table 5.2 and figure 5.3. The energy lost in the window was found to be 10.1 ± 0.7 channels out of 950. Therefore, 1.05 ± 0.07 % of the energy of the 5.486 MeV α -particles, or 57.6 ± 4.0 keV were lost in the window. The DSSSD manufacturer quotes an aluminium window of thickness $0.3 \mu\text{m}$. SRIM [71] shows that the measured α -particle energy loss in the window requires a window thickness of $0.374 \pm 0.026 \mu\text{m}$ of aluminium equivalent. Assuming the Micron Semiconductor [57] specification to be correct, the extra thickness (beyond $0.3 \mu\text{m}$) must be due to the dead layer of silicon and to an insulating SiO_2 layer that passivates the detector. Since both SiO_2 and Si have similar stopping powers to Al [71], it is safe to assume that ions incident on the DSSSD pass through $0.374 \pm 0.026 \mu\text{m}$ of pure aluminum before entering the active volume of the DSSSD for the purpose of modelling the window defect. The error introduced by making this assumption is negligible in comparison to the inherent ± 6.1 % accuracy of SRIM [71] for heavy ions with proton number between those of beryllium and uranium.

5.3.2 The Nuclear Stopping Defect

The nuclear-stopping defect is the result of non-ionizing nuclear collisions in a detector, and is most prominent for ions of low velocity and high Z [72]. The magnitude of the nuclear stopping defect for an ion of given energy can be modelled using SRIM for an ion of energy, E , by two steps. First, by subtracting the window defect from the incident energy of the ion to deduce the energy of the ion, E' , as it enters the depletion region. Second, by using E' as an incident energy on a silicon target in the TRIM portion of the SRIM software. TRIM performs a Monte Carlo simulation of incident ions and outputs the average percentage of energy converted to ionization in silicon. The remaining energy is lost to nuclear collisions. The energy lost is the nuclear stopping defect, and can be added to the window defect to model the total pulse height defect, giving an observed energy E'' . The nuclear stopping

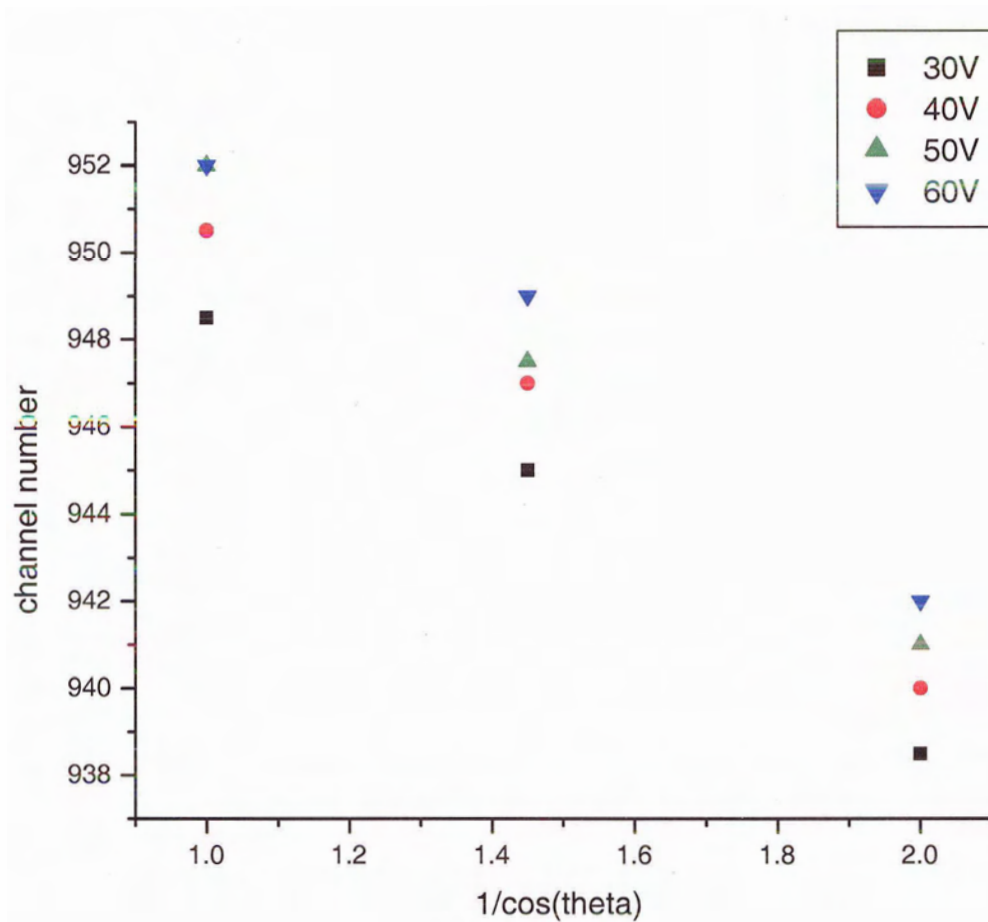


Figure 5.3: Window defect as a function of window thickness.

θ (deg.)	$\frac{1}{\cos(\theta)}$	channel no.	bias (V)
0	1	948.5	30
0	1	950.5	40
0	1	952	50
0	1	952	60
45	1.45	945	30
45	1.45	947	40
45	1.45	947.5	50
45	1.45	949	60
60	2	938.5	30
60	2	940	40
60	2	941	50
60	2	942	60

Table 5.2: Window thickness measurements.

defect is stochastic and statistical anomalies contribute to the low-energy tail of the energy spectrum.

5.3.3 The Residual Defect

The residual defect is due to incomplete charge collection in the detector when electron-hole pairs recombine prior to charge collection, particularly in dense ionization tracks [73]. Recombination may be avoided by increasing the electric field strength in the detector by raising the bias voltage.

Lowering the DSSSD bias voltage from 60 V to 30 V bias was measured to cause a 0.4 ± 0.4 % reduction in pulse height for ^{241}Am α -particles. Above the full depletion voltage, increases in bias voltage had a less significant effect on the pulse height defect for α -particles. The residual defect is expected to be larger for heavy ions since they produce denser ionization tracks.

Radiation damage increases the residual defect by producing charge trapping centers, which promote electron-hole recombination [49, p. 391]. The influence of radiation damage

on the residual defect could be measured systematically by gradually inflicting radiation damage on one DSSSD intentionally, however this would be expensive.

5.3.4 Energy Calibration as a Function of Ion Species

The predictions of the above model for the pulse height defect can be compared with measurements of the pulse height defect for ions of known energy and species taken with DSSSDs installed at the end of DRAGON (figure 5.4). For each DRAGON run, a ^{241}Am α -particle peak is present in the DSSSD singles spectrum centered at channel number 836 which serves to ensure that the gain remains constant. The α -particles have an incident energy of 5.486 MeV, which is degraded by $1.05 \pm 0.07 \%$ due to energy loss in the window. The nuclear stopping defect is negligible for these α -particles. Therefore, we may say that without the pulse height defect, and ignoring a small ADC offset, there are 154.0 ± 1.5 channels/MeV. We can compute the (measured channel number)/(known incident ion energy) for each ion species, and compare it to the nominal value to deduce the percentage of ion energy that was lost to the pulse height defect. This number is shown in the last column of table 5.3, and may be compared with the number deduced from the model in the penultimate column. SRIM [71] claims 6.1 % accuracy for ions with proton number between those of beryllium and uranium. The standard deviation, σ_{ion} , of heavy ion peaks in DSSSD energy spectra is 17 % of the pulse height defect on average. The standard deviation in the nominal pulse height as a percentage of the pulse height defect, $\sigma_{\alpha} = 8.5 \left(\frac{E(\text{MeV})}{5.5} \right) \%$, is magnified linearly with energy since there is only one α -particle calibration point available. As a result, the model is more accurate at low ion energies where the pulse height defect is more prominent. This error budget results in a reduced chi-square, $\chi^2 = 0.87$, for the fit between the model and data. In most cases, the pulse height defect is underestimated by the model, which could be due to omission of the residual defect.

Shown in figure 5.4 is a sample singles DSSSD energy spectrum. In the spectrum are 5.25 MeV ^{22}Na recoils centered at channel 628, 5.5 MeV ^{21}Ne beam centered at channel 681, and a few 5.486 MeV α -particle counts centered at channel 836. Although all of the particles have energies around 5.5 MeV, the peaks reside in different channels in the energy spectrum because of the pulse height defect. Figure 5.5 is a spectrum which requires DSSSD events to be in coincidence with an event in the γ -ray detector array, with an appro-

Ion	Z_{ion}	E_{ion} (MeV)	E'	E''	$\frac{E-E''}{E}$ (%)	$\frac{\Delta chan}{chan}$ (%)
^4He	2+	5.486	5.43	5.42	1.2	—
^{21}Ne	10+	5.5	4.70	4.50	18.2	20.1
^{21}Ne	10+	15.8	14.9	14.7	7.0	11.7
^{21}Na	11+	11.6	10.6	10.4	10.3	14.0
^{21}Na	11+	15.9	14.9	14.7	7.5	9.4
^{22}Na	11+	5.25	4.33	4.11	21.7	22.1
^{22}Na	11+	15.0	14.0	13.8	8.0	13.6
^{22}Mg	12+	11.1	9.98	9.78	11.9	16.8
^{22}Mg	12+	15.2	14.0	13.8	9.2	12.3
^{24}Mg	12+	9.9	8.79	8.58	13.3	13.6
^{24}Mg	12+	19.4	18.3	18.1	6.7	4.2
^{25}Al	13+	9.5	8.35	8.0	15.8	15.5
^{25}Al	13+	18.7	17.5	17.2	8.0	6.6

Table 5.3: Calculated and measured pulse height defects.

appropriate delay for recoil time of flight. The figure shows that the peak centered at channel 628 is the recoil peak. The apparent height of the peak in this spectrum is increased by a factor of four due to binning. The number of counts in the coincident recoil peak is approximately half that in the singles recoil peak due to the γ -ray detector array efficiency of $\approx 50\%$.

The model may be used to predict the centroid channel numbers of beam and recoil peaks in DSSSD energy spectra for future DRAGON experiments, and to see if any experiments at particularly low energy, or high Z, will have problems due to the pulse height defect. Shown in table 5.4 are the predicted pulse height defects and energy spectrum channel number locations of beam and recoils respectively for proposed DRAGON experiments. The $^{15}\text{O}(\alpha, \gamma)^{19}\text{Ne}$ calculation raises concern because the pulse height defect is so large, about 30 % for beam and 40 % for recoils, and because the pulse height itself is so small. It would be advantageous to use a detector with a thinner window for that reaction. Both $^{20}\text{Na}(p, \gamma)^{21}\text{Mg}$ and $^{26}\text{Al}(p, \gamma)^{27}\text{Si}$ are predicted to have relatively large pulse height defects. However, these reactions should not be a problem because the energies and pulse height defects for these reactions are similar to those of $^{21}\text{Ne}(p, \gamma)^{22}\text{Na}$ at 5.5 MeV which

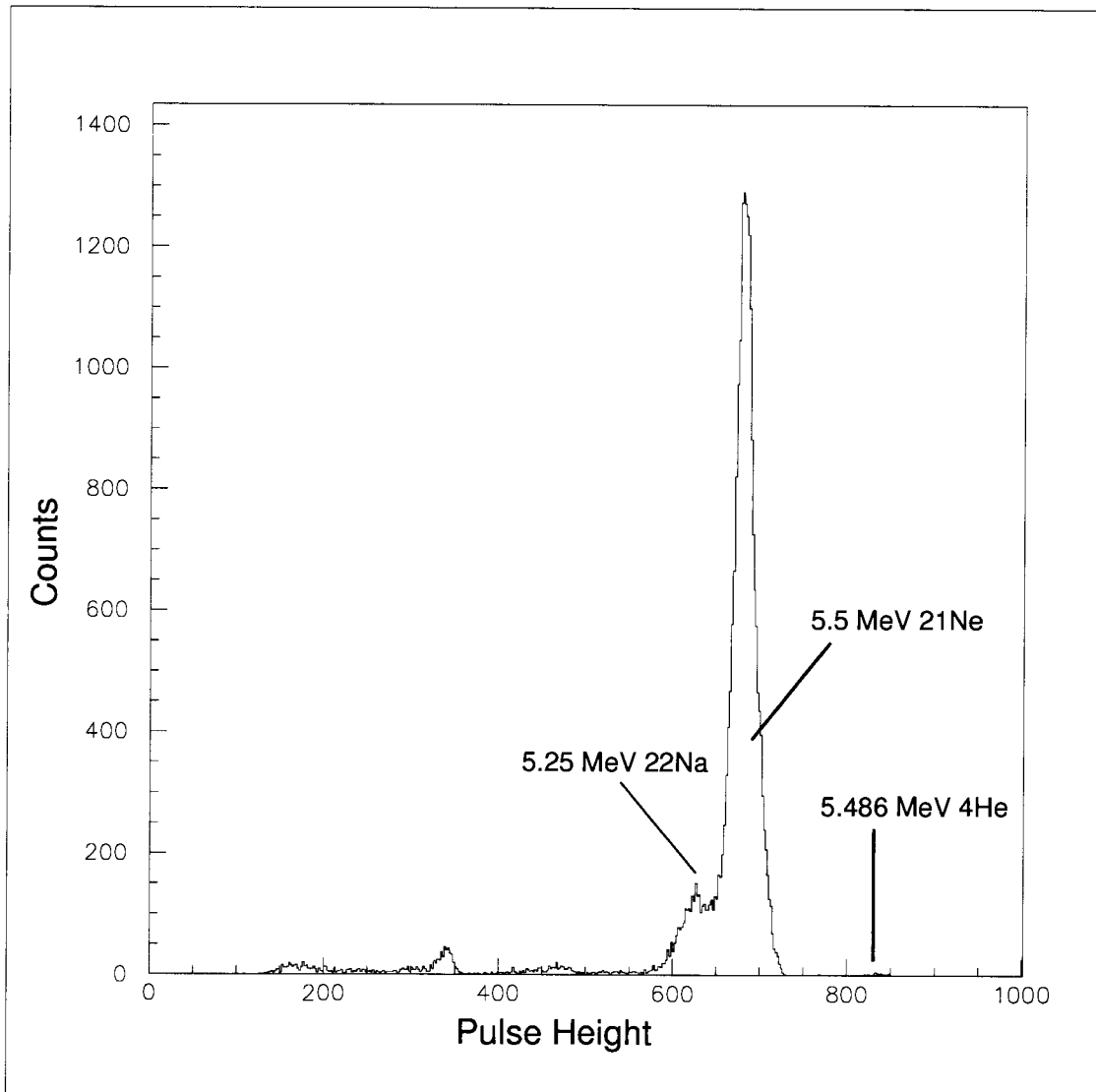


Figure 5.4: DSSSD singles spectrum for $^{21}\text{Ne}(p,\gamma)^{22}\text{Na}$ at 5.5 MeV showing the pulse height defect.

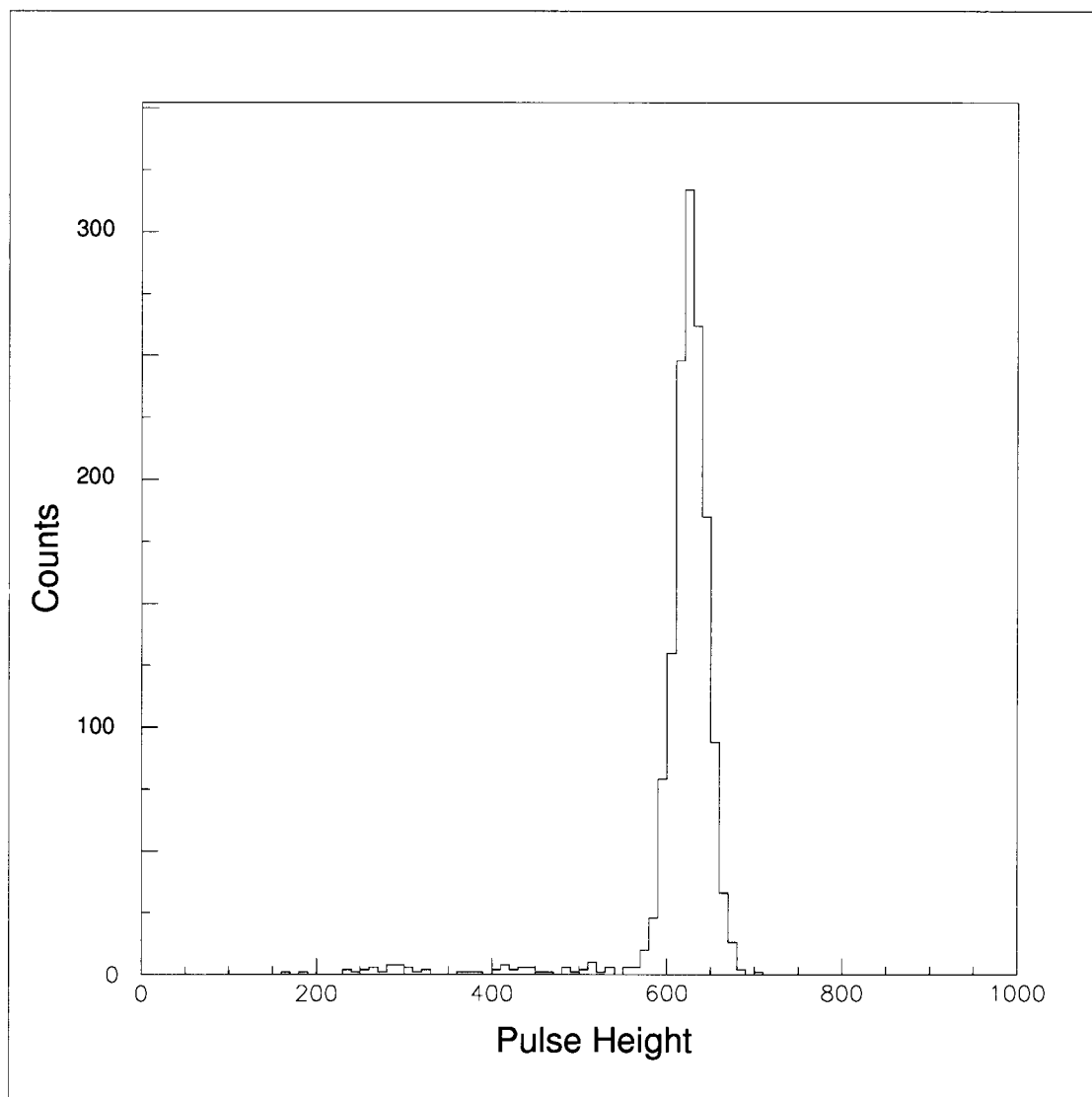


Figure 5.5: DSSSD γ -coincidence spectrum for $^{21}\text{Ne}(p,\gamma)^{22}\text{Na}$.

Reaction	species	Z (e)	E (MeV)	E'' (MeV)	$\frac{E-E''}{E}$ (%)	channel no.
$^{15}\text{O}(\alpha, \gamma)$	^{15}O	8+	2.4	1.67	30.5	296
	^{19}Ne	10+	1.9	1.15	39.3	178
$^{17}\text{F}(\text{p}, \gamma)$	^{17}F	9+	11.6	10.67	8.0	1643
	^{18}Ne	10+	10.8	9.73	9.9	1499
$^{18}\text{F}(\text{p}, \gamma)$	^{18}F	9+	6.3	5.35	9.8	875
	^{19}Ne	10+	5.9	4.91	16.7	757
	^{18}F	9+	8.6	7.65	11.0	1179
$^{19}\text{Ne}(\text{p}, \gamma)$	^{19}Ne	10+	8.2	7.14	12.9	1100
	^{19}Ne	10+	8.9	7.85	11.8	1209
	^{20}Na	11+	8.4	7.18	14.6	1105
$^{20}\text{Na}(\text{p}, \gamma)$	^{20}Na	11+	6.2	5.02	19.0	773
	^{21}Mg	12+	5.9	4.70	20.3	724
$^{23}\text{Mg}(\text{p}, \gamma)$	^{23}Mg	12+	12.2	10.9	11.0	1672
	^{24}Al	13+	11.8	10.3	12.8	1585
$^{25}\text{Al}(\text{p}, \gamma)$	^{25}Al	13+	11.8	10.3	12.9	1583
	^{26}Si	14+	11.4	9.88	13.3	1522
$^{26m}\text{Al}(\text{p}, \gamma)$	^{26m}Al	13+	6.0	4.70	21.7	723
	^{27}Si	14+	5.7	4.32	24.1	666

Table 5.4: Pulse height defects for proposed DRAGON reactions.

did not introduce crippling problems in the analysis of DSSSD spectra.

5.4 The Gap Effect

Neighboring DSSSD strips are separated by an insulating SiO_2 gap. It has been observed [74] that a highly ionizing non-transmitted charged particle entering an oxide passivated ion-implanted DSSSD through the gap between front (p -type) strips induces a reduced pulse height in one of these strips in comparison to a particle entering directly through a strip. This effect is believed to be the result of negative charge trapping due to the shape of the electric field between the strips [74]. This effect was examined using α -particles collimated

to enter the detector through the gap between front strips ².

First, a $10 \mu\text{Ci } ^{241}\text{Am}$ source was fixed 20.0 ± 0.5 cm from the surface of the DSSSD and collimated with a paper slit $280 \pm 20 \mu\text{m}$ wide. The collimator was placed 5 mm in front of one of the front strips. Data were taken under the following conditions:

1. the slit was placed parallel to the strip positioned at its center, and
2. the slit was positioned to straddle a gap between two front strips.

The count rate under the full energy peak for case (2) was $\approx 41 \%$ of that for case (1). This is consistent with the ratio of the gap width (measured to be $110 \pm 2 \mu\text{m}$ with a microscope) to the slit width, suggesting that none of the α -particles entering through the gap produced signals with pulse heights corresponding to the full energy. The slit was then aligned orthogonal to the strips so that it crossed several gaps. The deficiency of full energy counts in the relevant strips was slightly greater than the ratio of the gap width to the strip width, confirming that none of the α -particles entering the gap produced a signal of full energy.

Next, a $180 \pm 20 \mu\text{m}$ slit was aligned parallel to a gap and moved across two gaps in small steps with a micrometer. To ensure that the slit was parallel to the gap, the slit orientation was adjusted until the two strips adjacent to the gap had a nearly uniform count rate along the strips (fig. 5.6). Figure 5.7 shows the summed full energy count rate of the three relevant strips versus position of the slit. The two troughs correspond to the positions of two gaps. The widths and depths of the troughs are consistent with the assumption that the effective gap width is $120 \mu\text{m}$ and no α -particles entering the gap produce full energy pulses. The effective gap width is defined here to be the gap width which would account for the loss of counts in the full energy peak, assuming that no gap events produce a signal of full pulse height. The strip width is 3 mm, so $3.85 \pm 0.10_{stat} \pm 0.43_{sys} \%$ of all α -particles incident on the surface of the DSSSD are not detected at full pulse height.

There is a slight discrepancy between the specified gap width of $100 \pm 2 \mu\text{m}$ [57], the measured gap width of $110 \pm 2 \mu\text{m}$, and the effective gap width of $120 \mu\text{m}$. When a particle enters the DSSSD, the column of plasma produced has a diameter on the order of microns [75]. If a particle enters a strip at a location that is within a few microns of a gap

²The text of this section follows ref. [18] closely

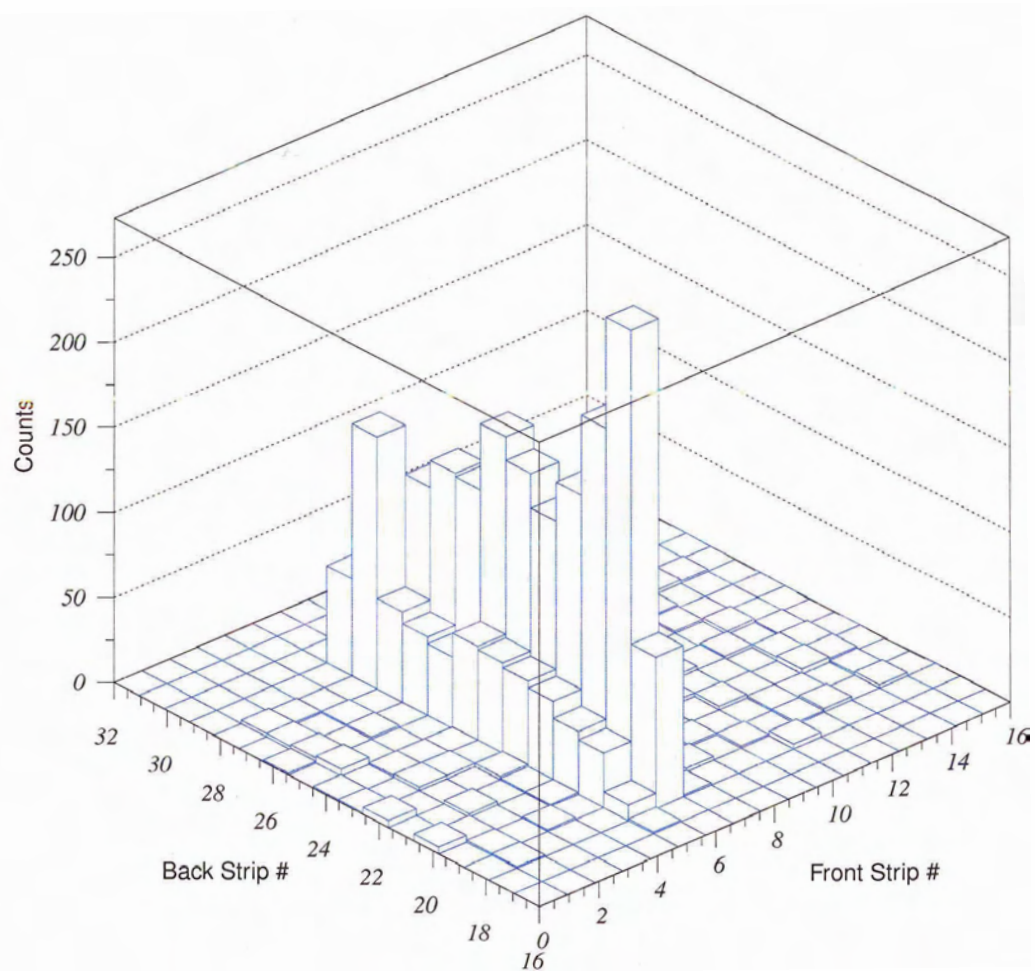


Figure 5.6: Parallel collimator evidence: counts on strips adjacent to a collimated gap.

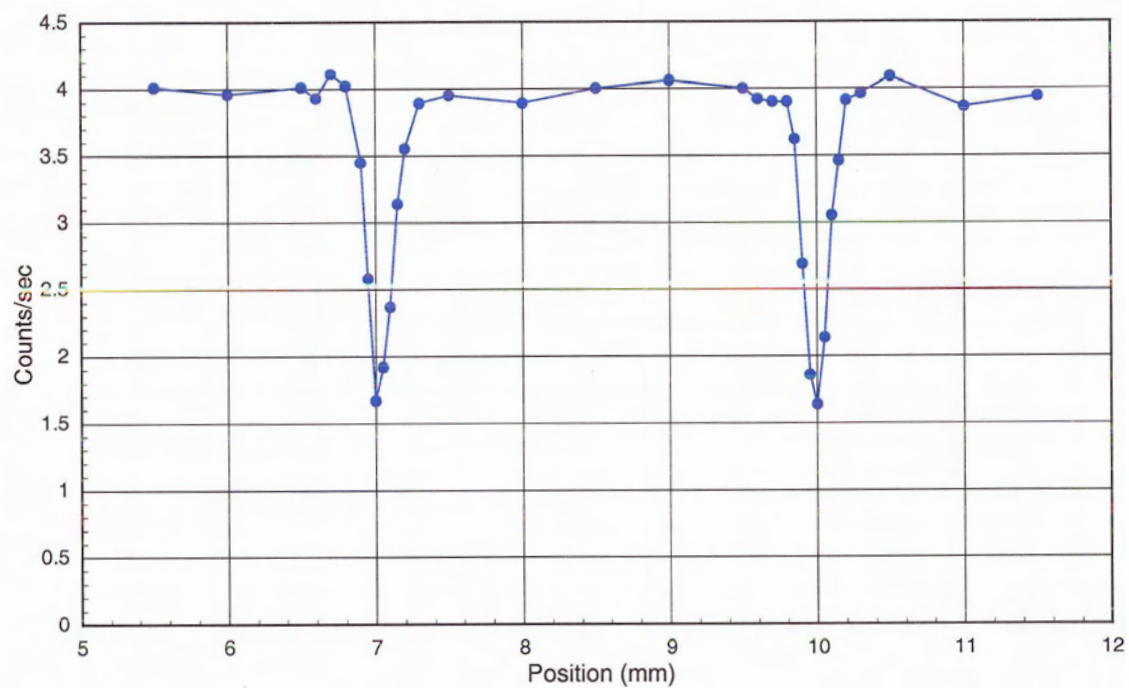


Figure 5.7: Scan of a 180 μm collimator across two gaps and three strips.

then some of the plasma column will lie within the gap and may be trapped, causing a pulse height defect. The effect may be further enhanced by transverse diffusion of charge carriers ($\approx 5 \mu\text{m}$ for $300 \mu\text{m}$ detector thickness [95]) during charge collection. These may be the reasons that the effective gap width is larger than the actual gap width.

By integrating the energy spectra of the relevant front strip(s) in case (1) and case (2) above, and subtracting the background (α -particles that penetrated the paper collimator), it was observed that the total count rate in the relevant front strip(s) was constant. Therefore, α -particles that entered through the gap each produced one signal on one front strip, but at reduced pulse height. Most of these gap events are present under a peak in the energy spectrum that is at about half the energy of the full energy peak, however there is also a continuum of gap events from zero energy up to the full energy. Qualitatively, this distribution of pulse heights is in agreement with the proposed model of Yorkston et. al. [74], with the exception of an anomalous trough visible at an energy just above that of the gap peak (fig. 5.8), discussed in section 5.5.2. Their model also predicts the absence of a signal from back strips for gap events in the peak of reduced pulse height, due to the trapping of negative charge.

5.5 Beam Testing Results

5.5.1 Energy and Time Resolution

A DSSSD was mounted downstream of the first electrostatic dipole at the position of the mass slits [17]³. A 1 MeV/amu beam of ^{16}O was prepared by ISAC operators to have a minimal time spread and an optical focus at the DSSSD. The intrinsic time width of the beam bunches was less than 1 ns and the spot size was between 6 mm and 9 mm which corresponds to 2 or 3 strips on the DSSSD. The intensity of the beam was reduced to 1000 ions/s by selecting the improbable charge state of 8^+ at the charge separation slits downstream of the first magnetic dipole. The beam was scanned across the DSSSD by varying the field in the first electric dipole. Shown in fig. 5.9⁴ are the summed energy

³These measurements were done by Dr. Joel G. Rogers, Research Scientist, TRIUMF, and Dr. Ahmed Hussein, Professor, University of Northern British Columbia

⁴This figure was provided by Dr. Joel G. Rogers

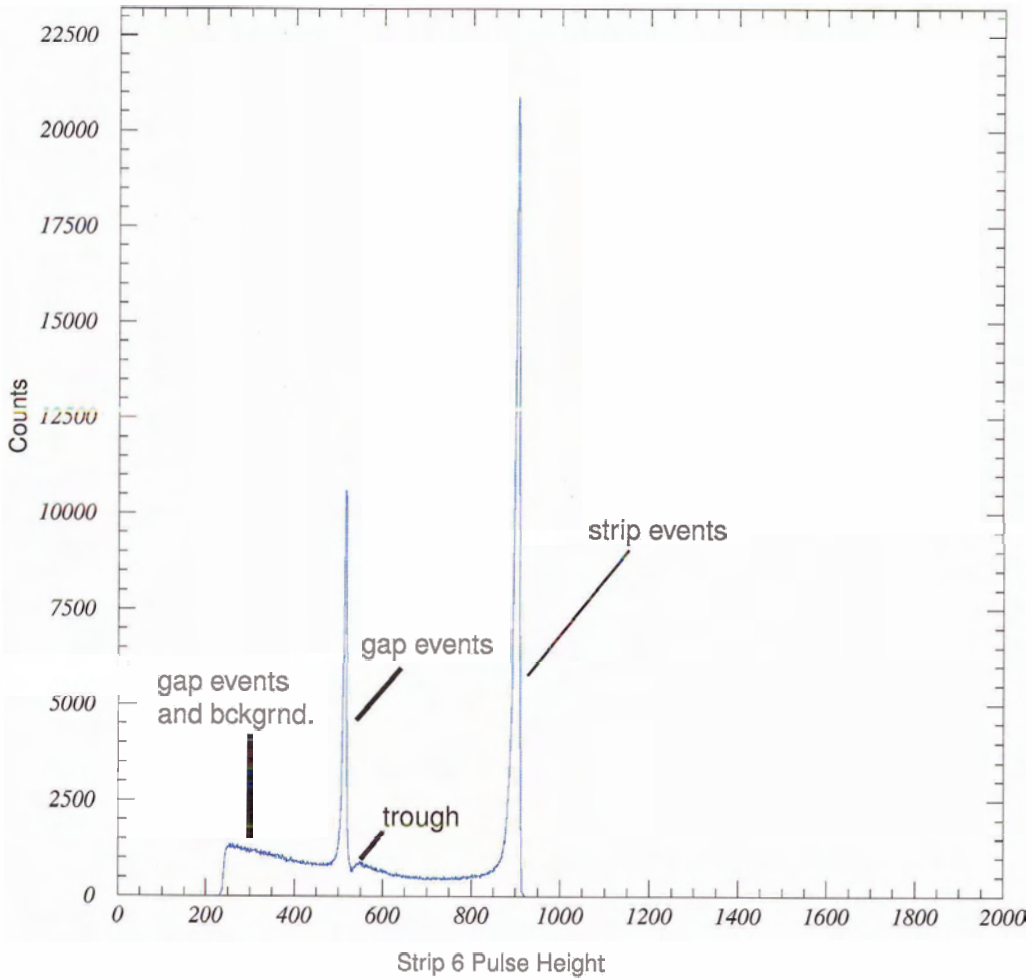


Figure 5.8: Gap peak and full energy peak in 5.486 MeV α -particle energy spectrum with a collimator straddling a gap.

spectra of all 16 front strips at 6 different positions across the DSSSD. The position of the centroid of the beam is shown in the top corner of each spectrum as a front strip number. The FWHM energy resolution of the full energy peak is shown as a percentage of the full pulse height. The peak around channel 800 is from a nearby α -particle source.

The energy resolution varies between 1.1 % and 1.8 %. The poor resolution around strip 5 is attributed to prior radiation damage. The poor resolution around strips 12 and 13 is attributed to a relative offset in their energy spectra. The time resolution of the DSSSD was measured to be 1.2 ns with the intrinsic time width of the beam bunches subtracted.

5.5.2 The Forbidden Trough

A curious feature of the ^{16}O spectra (fig. 5.9) is a trough occurring at an energy just above the energy of the gap peak in each spectrum. A similar trough was seen when observing gap events during α -particle testing (fig. 5.8). The long continuum of events at all energies below the full energy and above the discriminator threshold is known to consist mainly of gap events because the continuum is not present in α -particle runs performed with the collimator over a strip, and it is far too intense to be the low energy tail from nuclear scattering within the DSSSD. Therefore, the trough is a feature of gap events. The small number of events occurring within the trough can be attributed to nuclear scattering within the DSSSD. Since the trough represents the possible absence of less than 0.1 % of all events, the trough is merely a curiosity.

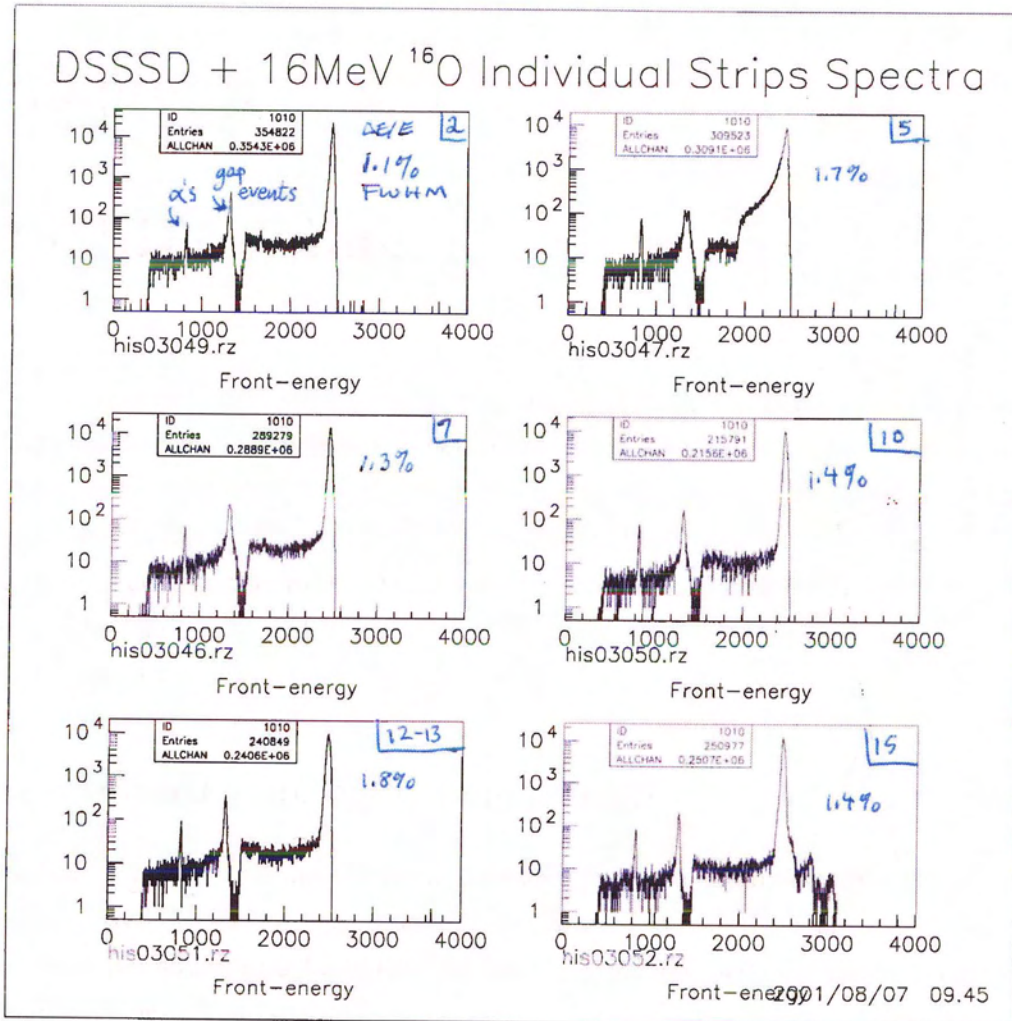


Figure 5.9: Scan of a 1 MeV/amu ^{16}O beam across a DSSSD.

Chapter 6

DSSSD Cooling

It is well known [76, 77] that cooling semiconductor radiation detectors can improve their energy resolution. In DRAGON experiments, the separation of recoil events from leaky beam events in DSSSD energy spectra can be enhanced by reducing the overall energy width. A cooling system has been designed and tested with the interest of minimizing the thermal contribution to the DSSSD energy resolution. However, reviving the growing stock of radiation damaged DRAGON DSSSDs has proved to be the primary benefit of the cooling system.

6.1 DSSSD Cooling System Design

To avoid the need for a cumbersome liquid cooling system, thermoelectric (Peltier) cooling was employed. However, water cooling was required to cool the heat sink of the thermoelectric device so a hybrid thermoelectric/liquid design was used. The system required three iterations of design and testing.

6.1.1 The Peltier Effect and its Application

When two dissimilar conductors are brought into contact and a current is transmitted through their junction, the junction either produces or absorbs heat (depending on the direction of the current) due to the difference in energy of the conduction bands of the two materials [78]. This effect, discovered in 1834 by French Physicist Jean Peltier [79], has since

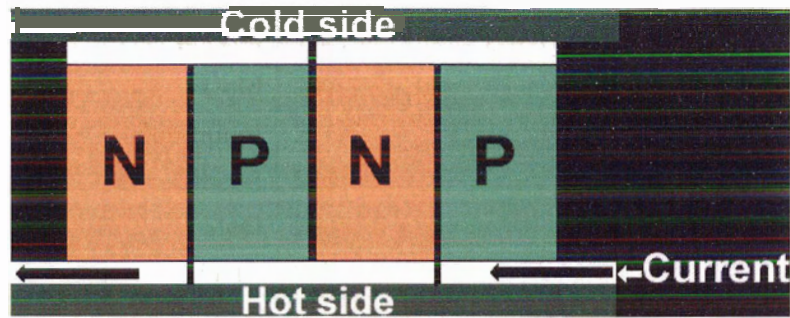


Figure 6.1: Peltier effect in a thermoelectric pump.

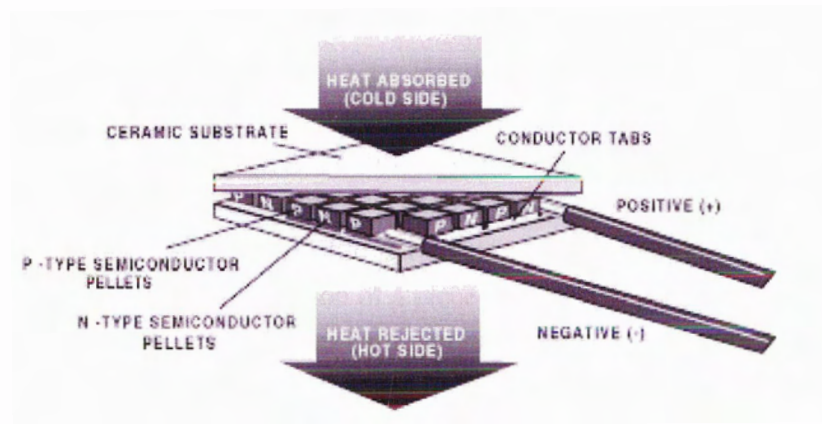


Figure 6.2: Schematic of a Peltier cooler.

found many cooling applications [80] and is known as the Peltier effect.

In modern thermoelectric coolers it is convenient and efficient to use bismuth telluride n -type and p -type semiconductors arranged alternately in series (figure 6.1). By placing heat-absorbing junctions on one side of the device and heat producing junctions on the opposite side and applying a direct current, one can pump heat across the device (figure 6.2). Such a device is commonly referred to as a “Peltier cooler”.

Peltier coolers are capable of producing temperature differentials of up to $\Delta T = 60\text{ }^{\circ}\text{C}$. Performance is determined by several factors including the semiconductors used, the current-voltage characteristics of the device, the quality of the heat sink, the thermal connection to

Material	Thermal Conductivity (W/m/K)
Gold	291.3
Aluminium	216.5
Silicon	145.7
Steel	20.0
G-10	0.3

Table 6.1: Thermal conductivities of cooling system materials.

the heat sink, the power supply available, and the heat load.

6.1.2 Heat Transfer

Heat may be transferred by three processes: conduction, convection and radiation [81, p. 543]. All three of these processes are relevant to the DSSSD cooling system.

Conduction is the transfer of heat through a material by collisions between its atoms. For example, if one heats a small portion of a piece of material, then its atoms move faster in this portion. When fast moving atoms collide with colder neighboring atoms, they transfer kinetic energy to these atoms, speeding them up and heating adjacent portions of the material, and so on. Different materials transfer heat at different rates.

Thermal conductivity is a property of materials that expresses the heat flux f_c (W/m²) that will flow through the material if a temperature gradient, $\frac{dT}{dx}$ (K/m), exists over its thickness. The thermal conductivity, l , is expressed in W/m/K. The equation,

$$f_c = l \frac{dT}{dx}, \quad (6.1)$$

relates the temperature gradient to the heat flux via the thermal conductivity [81, p. 545]. Thermal conductivity is a property that describes an equilibrium situation; the temperature gradient is assumed to be constant. If the temperature gradient starts to change then other parameters enter the equation. Table 6.1 shows the thermal conductivity of materials relevant to this work [82].

Radiative heat transfer is the transfer of heat by electromagnetic radiation. An ideal blackbody is one which absorbs all of the radiation incident upon it, and emits this energy

with a characteristic spectrum [83]. The power, P , emitted by an ideal blackbody can be shown [84, 85] to be

$$P = \sigma AT^4, \quad (6.2)$$

where A is the surface area of the blackbody, T is its temperature and σ is the Stefan-Boltzmann constant. To a first approximation, many of the solids that we encounter on Earth behave as blackbodies. The heat flux, f_R , between two infinite parallel plate ideal blackbodies of temperature T_1 and T_2 can be shown to be

$$f_R = \sigma (T_1^4 - T_2^4). \quad (6.3)$$

Convective heat transfer is the transfer of heat by moving hot atoms from one place to another [81, p. 548]. For example, breathing and showering are convective processes. In general, convective processes are chaotic and difficult to describe mathematically.

6.1.3 Cooling System Design I

The original design for a DSSSD cooling system consisted of a Leufken Technologies TEC156 [86] Peltier cooler sandwiched between a cold plate and a water cooled heat sink. The TEC156 is 5 cm², and 3.5 mm thick, and is powered by a Hewlett-Packard Model 6286A [87] 12V, 12A maximum, variable DC power supply. The electronic components of the Peltier cooler are contained and insulated electrically by a thin layer of ceramic, which also conducts heat from the cold plate and to the hot plate.

Because the DSSSD is a transmission detector, there is very little back surface to which a cold plate can be contacted. The cold plate was designed to have maximal direct contact with the grounded gold plating on the back of the G-10 DSSSD frame. The rest of the cold plate was sunken by a fraction of a millimeter so that it would not touch the back active surface of the DSSSD and the fragile wires that connect individual strips to the circuit board, or short circuit wires on the circuit board. The sunken portion of the cold plate was kept about 1 mm from the back surface of the DSSSD so that it might induce maximal radiative cooling. The DSSSD was held in place by a set of washers, screws, and ridges in the copper which fit snugly around the sides of the G-10 board, defining the position of the DSSSD. Figure 6.3 shows the surface of the cold plate on which the DSSSD sat.

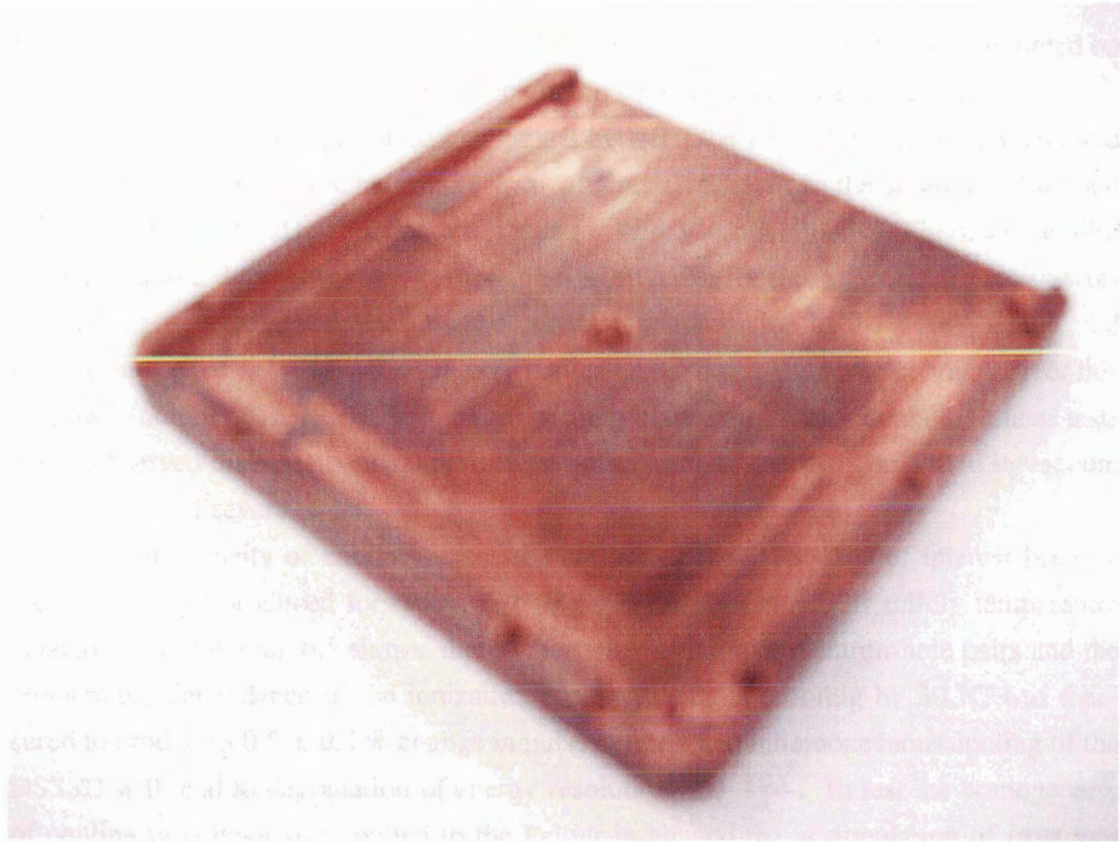


Figure 6.3: Cold plate for cooling system design I.

The heat sink consisted of a copper cylindrical chamber of 3 cm diameter through which 2 L/min of 10 °C city water flowed continuously. The heat sink was mounted through a vacuum plate containing feed-throughs for the DSSSD ribbon cable, four K-type thermocouples read out by a Fluke 54 II [88] thermometer, and DC voltage for the Peltier.

6.1.4 Testing of Cooling System Design I

Before testing the thermal characteristics of the cooling system, a DSSSD was mounted on the cold plate and checked for short circuits with an ohmmeter; none were found.

Good thermal contact must be maintained between the Peltier and the cold plate, and between the Peltier and the heat sink. Without a material between the ceramic Peltier and the copper plates to aid conduction, the cooling system was not effective. Thermalcote [89], a silicone based thermal transfer compound was effective for this purpose. However, worries about evaporation of the paste and subsequent condensation on the surface of the cold DSSSD prompted a test of indium (a very malleable solid and good heat conductor) for this purpose. Indium proved to be better than nothing but unsatisfactory overall. In later tests it was observed that there was no noticeable evaporation of thermal compound in vacuum over a period of several weeks.

The homogeneity of cooling across the surface of the DSSSD is of interest because the pulse height produced for radiation of a given incident energy is mildly temperature dependent, as equation 6.5 shows, due to thermal excitation of electron-hole pairs and the temperature dependence of the ionization energy in silicon (cooling by 30 °C was measured to produce a 0.5 ± 0.4 % change in pulse height), and inhomogeneous cooling of the DSSSD will lead to degradation of energy resolution of $1 \frac{\text{keV}}{^\circ\text{C}}$. To test the homogeneity of cooling, a voltage was applied to the Peltier in air and the accumulation of frost was observed on the DSSSD. It was clear that one quadrant of the DSSSD was colder than the others. This inhomogeneity is attributable to non-uniform pressure applied by the washers which hold the DSSSD against the cold plate, providing contact.

Performance of the system in vacuum was tested by measuring the temperature of the cold plate, heat sink, and the center of an unusable DSSSD simultaneously with the K-type thermocouples and thermometer. Optimal operating conditions were 8 V and 8 A applied to the Peltier. Under these conditions, the heat sink was measured to be 31 °C, the cold

plate $-8.5\text{ }^{\circ}\text{C}$, and the DSSSD $2.0\text{ }^{\circ}\text{C}$. The Peltier worked well but the cold plate was not cooling the DSSSD to its own temperature.

The lack of heat transfer from the DSSSD to the cold plate can be attributed to four factors.

1. Under vacuum there is no convective cooling. This is the reason that the DSSSD did not reach sub-zero temperatures as it did in air.
2. A lack of firm contact between the DSSSD and the cold plate can hamper conductive heat transfer.
3. Heat from the center of the DSSSD must be conducted from the bulk silicon, and through the G-10 board, before coming into contact with the cold plate.
4. G-10 is a terrible heat conductor (table 6.1). Still, in the absence of a heat source the DSSSD should eventually reach the temperature of the cold plate. Therefore, radiative heating of the DSSSD competes with conductive and radiative cooling provided by the cold plate.

Factors one and three cannot be avoided. To test the importance of the fourth factor, a piece of aluminum foil was appended to the cold plate and curled over the front face of the DSSSD without contacting it, to shield the DSSSD from thermal radiation inside the vacuum box. It was observed that the minimum temperature of the DSSSD was reduced by $5\text{ }^{\circ}\text{C}$. This proved that radiative heating was a factor to consider. An attempt was made to improve on the above deficiencies with a redesign of the cold plate.

6.1.5 Cooling System Design II

A new design of the cold plate imposed tighter, electrically insulated clamps on the frame of the DSSSD to improve contact with the cold plate and the homogeneity of temperature across the DSSSD. The clamps were designed to have variable position across the surface of the frame of the DSSSD to accommodate DSSSDs mounted on G-10 boards of various sizes. Pins were inserted in the cold plate to fix the position of the DSSSD absolutely by its mounting holes rather than by the dimensions of the G-10 board. Shown in figures 6.4

and 6.5 are the outside and inside of the vacuum plate that holds the cooling system, respectively. Also present in the photographs are extra water lines and an extra cold plate which were added later. Figure 6.5 shows the new circular cold plate with a DSSSD clamped to it.

A 15.3 cm long, 10.3 cm diameter, cylindrical copper shell extending from the DSSSD to the far end of the vacuum box was appended to the cold plate, surrounding the DSSSD with cold walls. The geometry was chosen to avoid constraints on possible optics settings for DRAGON. A schematic of design II of the cooling system is shown in figure 6.6.

6.1.6 Testing of Cooling System Design II

Temperature versus Peltier Voltage

The effects of Peltier voltage on the temperatures of various components of the system were measured simultaneously. Temperature measurements were taken on the cold plate, on the hot plate, and in the center of an unbiased DSSSD. A DSSSD with broken wires and radiation damage was used so that the temperature could be taken in the center of the DSSSD without any concern of damaging the DSSSD. The Peltier voltage was raised in 1 V steps to a maximum of 12 V. The radiation shield was employed for these measurements. The results are shown in table 6.2 and graphically in figure 6.7

It is apparent that 10 V on the Peltier gives optimal cooling. The minimum DSSSD temperature of $-13.5\text{ }^{\circ}\text{C}$ is cooler than required to improve the performance of a good DSSSD, or to revive any of the radiation damaged DSSSDs. The optimum temperature of the DSSSD is between $0\text{ }^{\circ}\text{C}$ and $-10\text{ }^{\circ}\text{C}$. Reducing the temperature to below $-10\text{ }^{\circ}\text{C}$ increases the risk of damaging the DSSSD through differences in the amount of thermal contraction in different DSSSD materials.

The temperature of the cold plate and the temperature of the DSSSD were not observed to be equal. This situation can be explained by appealing to factors one and three in section 6.1.4: the competition between radiative heating, and cooling by radiation and conduction. In the situation of maximum cooling once equilibrium has been reached, the ambient temperature is 296.0 K, the cold plate temperature is 252.6 K, and the DSSSD temperature is 259.7 K. If we assume the DSSSD to be sandwiched between two infinite parallel plate blackbodies (one representing the vacuum box and one representing the cold plate), then from equation 6.3, we have a net radiative heat transfer to the front surface of the DSSSD

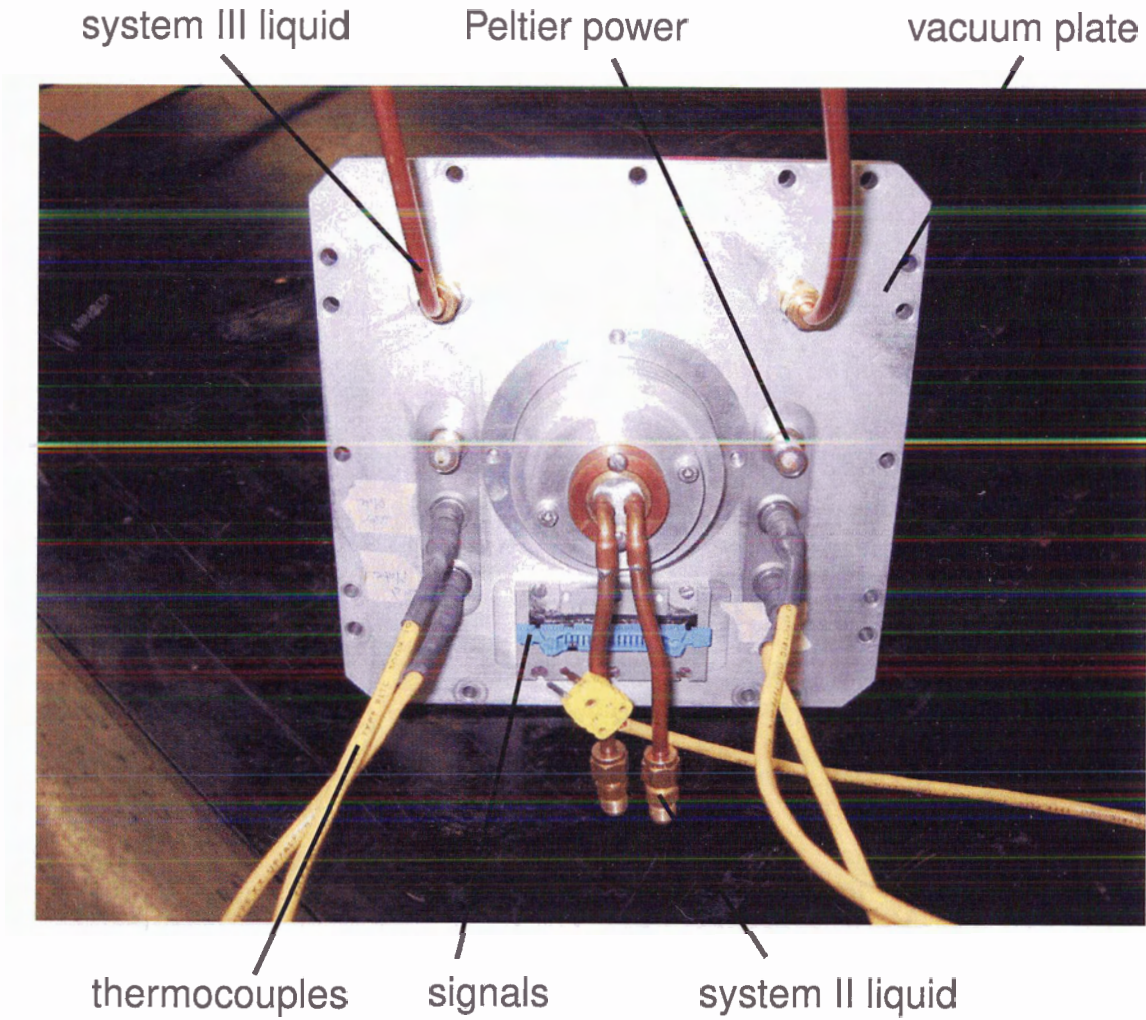


Figure 6.4: Outside of cooling system II vacuum plate and feed-throughs.

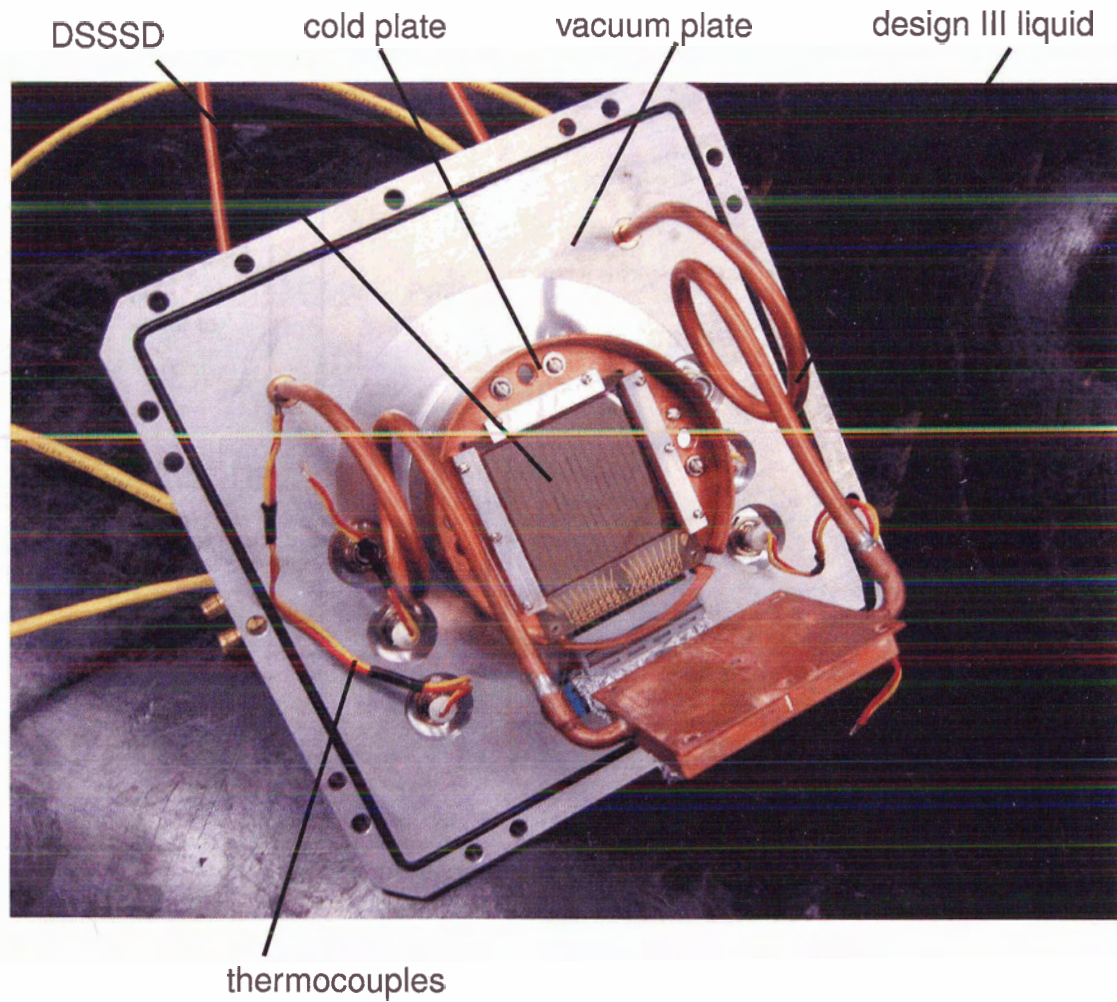


Figure 6.5: Inside of cooling system II vacuum plate.

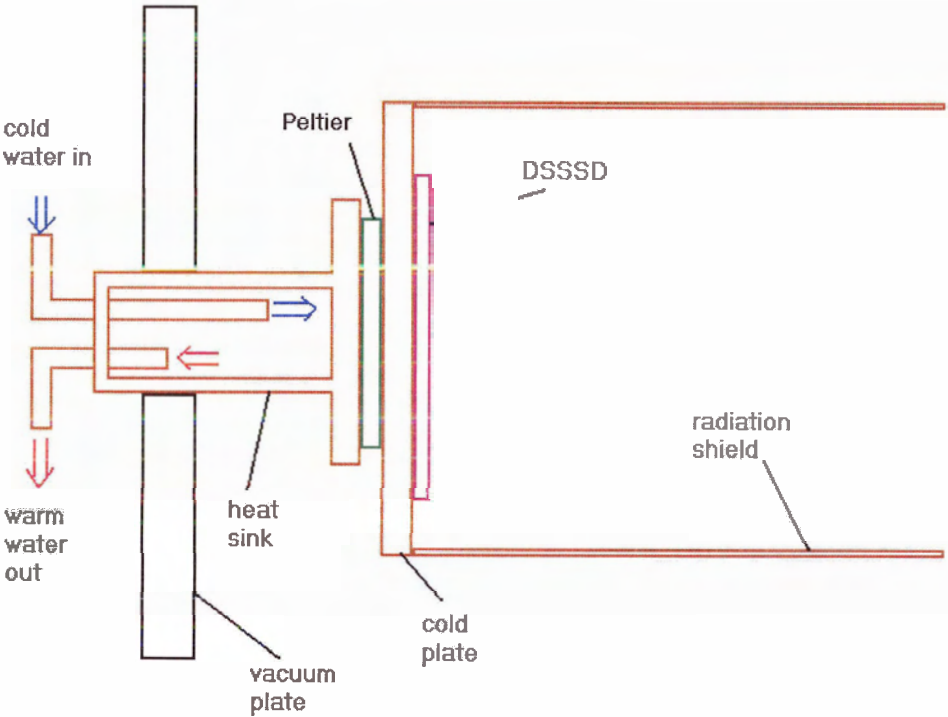


Figure 6.6: Schematic of cooling system design II.

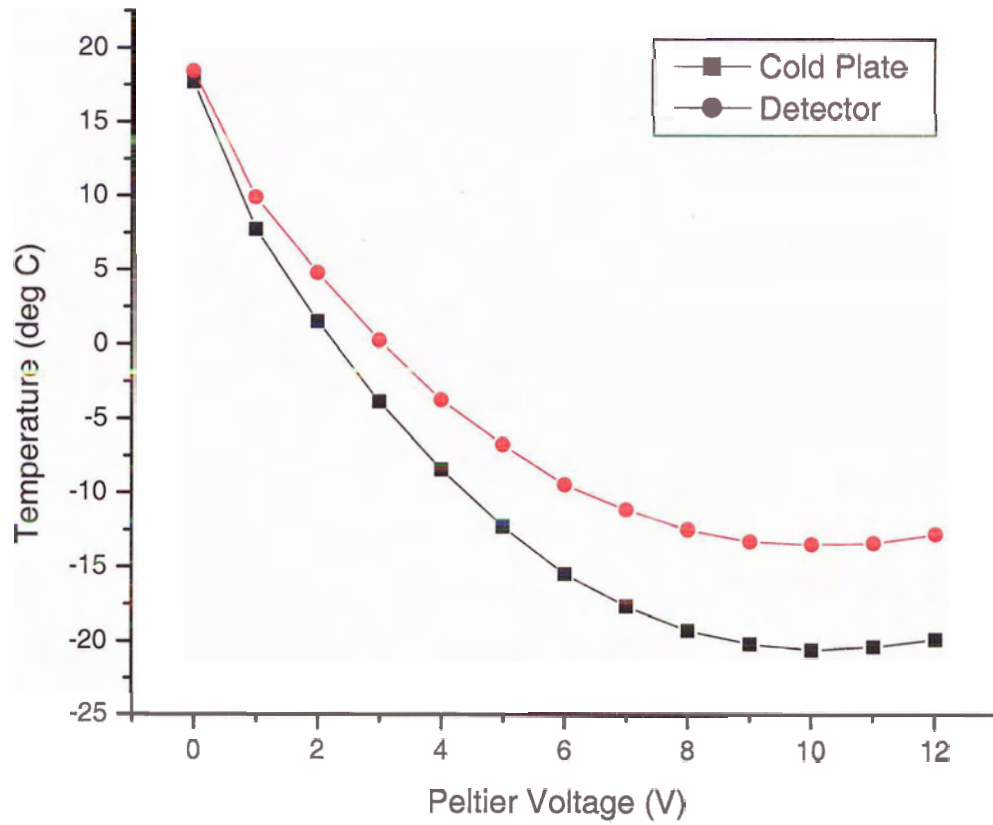


Figure 6.7: Effect of Peltier voltage on DSSSD temperature.

Pelt (V)	T cold plate	T detector	T hot plate	T ambient
0	17.7	18.4	18.0	20.0
1	7.7	9.9	16.6	20.0
2	1.5	4.8	16.0	20.0
3	-3.9	0.2	15.6	20.0
4	-8.5	-3.8	15.3	20.0
5	-12.3	-6.8	15.6	20.1
6	-15.5	-9.5	16.0	20.3
7	-17.7	-11.2	16.7	20.8
8	-19.3	-12.5	17.6	21.3
9	-20.2	-13.3	18.8	21.9
10	-20.6	-13.5	20.4	22.8
11	-20.4	-13.4	22.2	23.5
12	-19.9	-12.8	23.6	24.4

Table 6.2: Cooling system, design II temperatures versus Peltier voltage.

of 0.443 W (this is an upper limit since the radiation shield is in use). Similarly, we have a net heat transfer from the back surface of the DSSSD to the cold plate of 0.068 W. This leaves 0.375 W (at most) to be carried away by conduction. Let us assume that the rate determining step in heat conduction through the system is the G-10 board. The temperature gradient across the G-10 is about 7.1 K/0.2 cm. The cross section of G-10 available for conduction is about 0.1 cm \times 5 cm \times 4 sides. Using equation 6.1, we calculate the heat transfer through the G-10 to be 0.213 W. These estimates are of the right order of magnitude to show that a competition between radiative heating of the DSSSD and conductive cooling of the DSSSD through the circuit board results in the inequality of DSSSD temperature and cold plate temperature.

Restoration of ambient temperature

If the vacuum system is vented when the DSSSD is still cold, then condensation will form on the surface of the DSSSD. This situation should be avoided, so the temperature of the

time (mins)	T cold plate	T detector
0	-20.6	-13.5
1	-12.1	-12.1
2	-8.0	-9.8
3	-4.3	-6.7
4	-1.3	-3.5
5	1.3	-0.7
6	3.3	1.6
7	5.2	3.9
8	6.7	5.6
9	8.2	7.3
10	9.3	8.7
11	10.4	9.9
12	11.3	11.0
13	12.2	12.0
14	12.9	12.8
15	13.5	13.5
18	14.9	15.2

Table 6.3: DSSSD warming time.

DSSSD as a function of the time elapsed since the cooling system was deactivated is of interest. The temperatures of the cold plate and DSSSD were measured as a function of time after switching the Peltier off from 10 V. The results are shown in table 6.3 and plotted in figure 6.8.

The data show that the system should not be vented until 10 minutes have passed since deactivating the Peltier. Since the Peltier voltage can be reversed to pump heat into the cold plate and accelerate warming of the DSSSD, it may be tempting to do so. However, the cold plate and DSSSD are not designed to act as heat sinks and cannot dissipate heat efficiently so using this method introduces the risk of melting the soldered leads on the Peltier or damaging the DSSSD, and it should only be used in emergency circumstances.

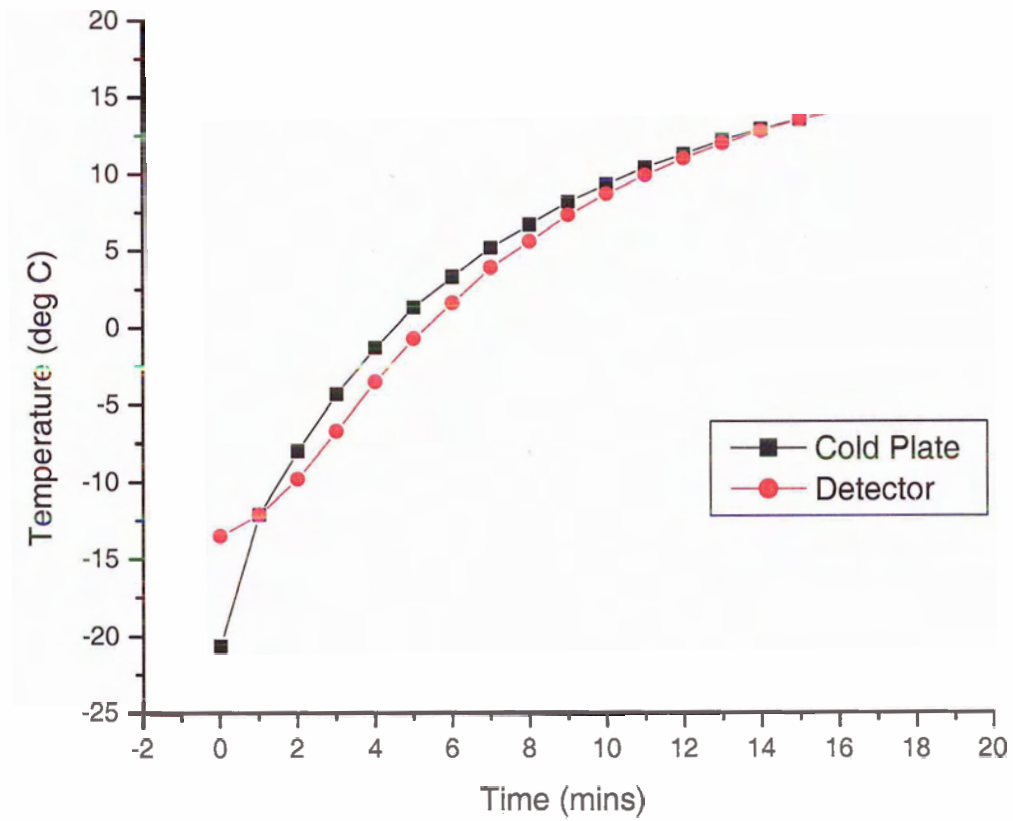


Figure 6.8: Restoration of ambient temperature of a cooled DSSSD.

6.2 Cooling New DSSSDs

It has been shown [77] that the 15 keV contribution of thermal detector noise to the energy resolution of silicon detectors can be effectively eliminated (when measuring ionizing particles of energy on the order of MeV) by cooling a silicon detector to -10°C . Originally, a cooling system for the DRAGON DSSSDs was proposed to improve the energy and timing resolution of the DSSSDs. However, other factors degrade the energy resolution of the beam, recoils and DSSSD to the point that the elimination of thermal detector noise altogether would not provide a significant improvement in overall energy resolution. Contributions to the recoil peak width in DRAGON DSSSD energy spectra include resonance width, prompt γ -ray direction, intrinsic beam energy spread, energy straggling in the gas target, energy straggling in the DSSSD window, fluctuations in electronic and nuclear stopping, and electronic noise. The beam peak is devoid of reaction effects but may be subject to less predictable contributions since the beam peak is composed ions that have likely undergone an interaction with residual gas or a solid surface in the separator. By isolating independent contributors from above to the width of the peak, their respective contributions add in quadrature [90, p. 17] and the small amount contributed by thermal detector noise becomes insignificant. For example, in the $^{21}\text{Na}(p,\gamma)^{22}\text{Mg}$ reaction at around 212 keV/u, the energy spread of ^{22}Mg recoils is 2.6 % [17] of the beam energy, or over 100 keV from reaction kinematics alone. Nevertheless, it is an interesting exercise to test the effects of cooling on an undamaged DSSSD off-line with an α -particle source and a pulser.

6.2.1 Effect of Cooling on α -particle Energy Resolution

Off-line testing with an α -particle source eliminates or reduces many of the contributions to the energy width observed in the DSSSD on-line. Reaction effects are eliminated, and there is no gas target straggling. Beam energy spread is replaced by energy straggling in the source, a thin source may contribute 10 keV to the width [77]. Because $Z = 2$ for α -particles, energy straggling in the DSSSD window is reduced to a width of $23.5\sqrt{x}$ keV = 15 ± 1 keV [91, 77], where $x = 0.374 \pm 0.026$ μm is the window thickness in microns, and fluctuations in nuclear and electronic collisions can be assumed to contribute 6 keV and 7 keV [77] respectively. Taking the above contributions to the width to be from fluctuations in independent quantities, they can be added in quadrature [90, p. 17]

to give a 20.2 keV width. Adding 24 keV (see next section) for noise due to the electronics associated with the DSSSD gives a 31.4 keV width. Thermal noise is expected to contribute 15 keV [77] at room temperature, for a total width of 34.8 keV or 0.63 % FWHM which is the best resolution measured with DRAGON DSSSDs using a ^{241}Am source. Therefore, the elimination of thermal noise should reduce the width of the peak in the energy spectrum from 0.63 % to 0.57 %, provided that a thin source is used.

On several occasions, an α -particle source was placed in front of an undamaged DSSSD and an energy resolution better than 0.7 % FWHM was measured at room temperature, and later at a sub-0 °C temperature using design II of the cooling system. On each occasion, there was a negligible change in energy resolution as a function of temperature. It was also observed that upon warming each DSSSD and measuring the resolution again, the resolution was degraded slightly from its former value, by about 0.1 % FWHM. Evidently, any improvement in resolution from cooling was balanced by this degradation, which is permanent. Damage in the DSSSD is induced even after a very small voltage is applied to the Peltier cooler so it is not an effect of excessive cooling, rather it is induced electromagnetically. For this reason it is not recommended to use the Peltier cooling system on DSSSDs that have no prior damage of any kind. A different power supply was used for comparison and yielded the same result, as discussed in the next section.

It was observed that pulse heights were reduced by about 0.5 % when DSSSDs were cooled from room temperature to -10 °C. This effect is due to two factors. First, the ionization energy in silicon is a function of temperature. For example, cooling silicon to liquid nitrogen temperature (77 K) has been shown to increase the ionization energy by 3 % [92] in an approximately linear fashion. Second, the probability of thermally exciting a charge carrier into the conduction band decreases with decreasing temperature [56, p.209]. Therefore, temperature stability and homogeneity throughout a measurement with a silicon detector are important, since thermal fluctuations and gradients contribute $1 \frac{\text{keV}}{^\circ\text{C}}$ [77] to the broadening of energy spectra.

6.2.2 Effect of Cooling on Pulser Width

If cooling improved the thermal contribution to energy resolution with the α -particle source then the improvement was masked by larger contributors to pulse height spread, and damage

from the Peltier system. Since a source with better resolution was not available, tests were done to see if the width of a pulser peak could be reduced by cooling a DSSSD. An Ortec 419 Precision Pulse Generator [93] was input to the preamplifier motherboard, and adjusted until it produced a pulse height equal to that produced by 5.486 MeV α -particles. The pulser resolution was determined to be optimal and constant with the DSSSD bias between 30 V and 60 V, so the bias was set to the usual value of 50V . Efforts were then made to minimize electronic noise. The optimal configuration was one with the turbo pump mounted on an adjacent vacuum box, all cables shielded and grounded, and the Peltier power supply grounded.

The width of the pulser peak was measured at various Peltier voltages. It was observed that the width of the pulser peak did not change significantly with the Peltier disconnected, with the Peltier connected and off, with the Peltier connected and on and no voltage applied, with application of voltage on the Peltier (i.e. cooling the detector), or with the increase of Peltier voltage. The average resolution of front strips remained constant at $0.43 \pm 0.03 \%$ in all of these situations. This is equivalent to a contribution of 24 keV to the peak width from electronic noise, assuming that the pulse is a δ -function. A typical pulser spectrum for strip 10 is shown in figure 6.9.

Peaks were observed between channels 110 and 140 in the energy spectra when the Peltier voltage was on. The peaks were present in the energy spectra when the DSSSD was disconnected from the electronics, so the peaks were picked up in the electronics from the Peltier power supply and not in the DSSSD. The presence of the extra peaks did not degrade the resolution of the pulser peaks. Figure 6.10 shows a comparison of a pulser spectrum with the Peltier off and disconnected to a pulser spectrum for the same strip with the Peltier voltage set to 6 V. The peak may result from an AC ripple in the DC voltage from the Peltier power supply, an HP 6286A; the frequency is close to 60 Hz.

To test the effect of the Peltier power supply on on the DSSSD and electronics, the power supply was replaced with a different model: a BK Precision Model 1601 [94]. With the application of 1.5 V and 3.0 V, there was no extra peak observed in the energy spectrum. However, using the different power supply with a new DSSSD mounted induced the same permanent damage in a DSSSD as the other power supply did. In conclusion, the extra peak and DSSSD damage are both induced by the Peltier system and the peak disappears with a good power supply. However, they are independent effects induced on different parts of the

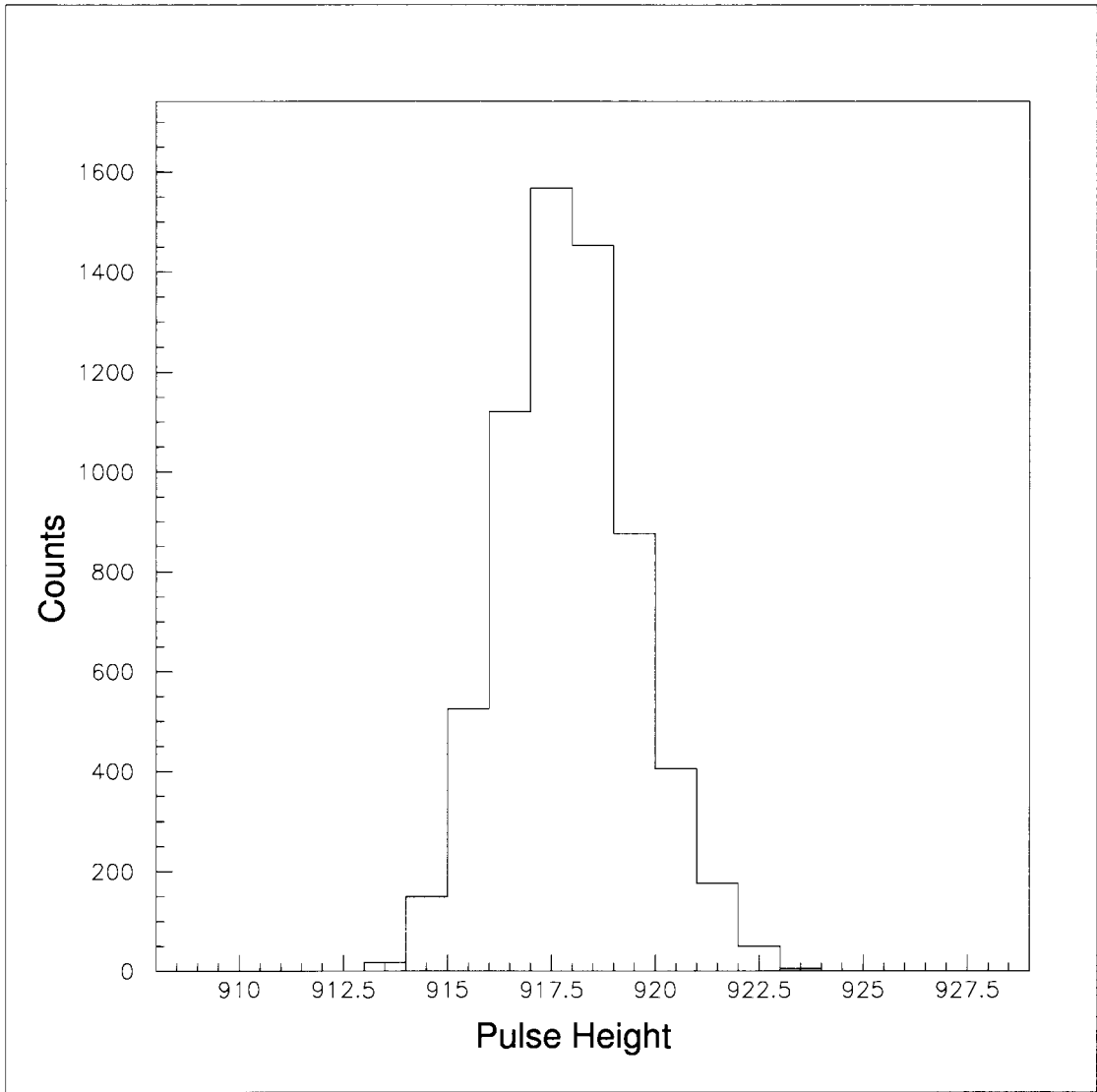


Figure 6.9: Pulser spectrum for strip 10 with Peltier disconnected and power supply off.

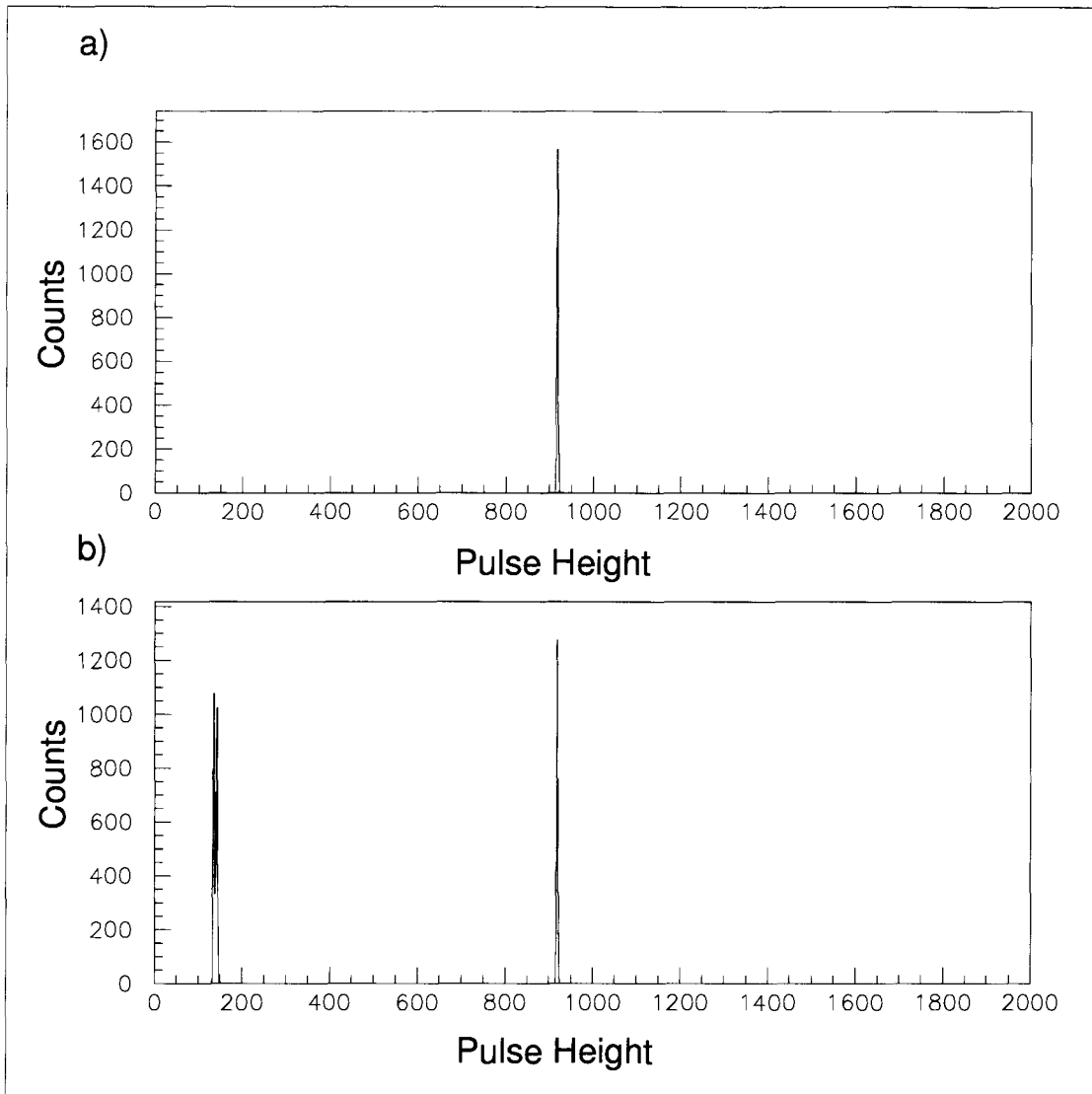


Figure 6.10: Pulser spectra for strip 10 with Peltier a) disconnected and power supply off, and b) connected and 6 V applied.

DSSSD system. The DSSSD damage is from an interaction between the Peltier system and the DSSSD whereas the extra peak is from an interaction between the Peltier system and DSSSD electronics or cables.

6.2.3 Effect of Cooling on Timing Resolution

The timing resolution of a cooled DSSSD has not been measured because a timing signal must be measured relative to another detector or to an accelerator frequency, neither of which are easily incorporated into the DSSSD test station. When the DSSSD cooling system is installed on DRAGON, scheduled for summer 2003, timing resolution can be measured relative to a PSTD, or relative to the the RFQ accelerator frequency. An advantage of cooling a DSSSD is that the leakage current is reduced significantly, as modelled by equation 6.5. Measurements with the cooling system displayed 20-fold reductions in leakage current from room temperature to -13.5°C . Therefore, the bias voltage can be raised to two or three times the depletion voltage without a risk of break-down of the diode. Doing so raises the electric field in the DSSSD, and reduces the charge carrier transit time and its fluctuation as discussed in chapter 7. Future timing measurements using DRAGON could measure time resolution as a function of temperature at fixed bias, and as a function of bias at fixed temperature.

6.3 Radiation Damaged Detectors

6.3.1 Radiation Damage

Radiation damage can affect detector performance. There are two mechanisms for inducing radiation damage in a segmented silicon semiconductor detector [49, p. 387] [95].

1. Bulk damage may result from an incident charged particle undergoing a non-ionizing collision with a silicon atom, displacing it from its lattice site. Depending on the collision kinematics, the recoiling silicon atom may displace further atoms forming a cluster of defects in the lattice. Bulk damage leads to charge carrier trapping, and a build-up of space charge which changes the required operating voltage and increases the leakage current.

2. Surface damage leading to increased surface currents may result from charge build up on the surface of the DSSSD and affect the inter-strip isolation. Effects of charge build-up depend strongly on the structure and composition of the detector.

The reverse bias current increase per unit volume for a silicon detector, ΔI_R , is a linear function of particle fluence, Φ , the time-integrated particle flux, when a DSSSD is used to detect transmitted particles.

$$\Delta I_R = \alpha \Phi, \quad (6.4)$$

where the damage coefficient $\alpha = 3 \times 10^{-17}$ A/cm for minimum ionizing protons, for example [95]. Equation 6.4 can be simplified for low energy heavy ions of the same energy: if the ions are all stopped in the detector then the detector volume is irrelevant and current is proportional to the total number of ions incident on the detector. Low energy heavy ions induce more damage per particle than minimum ionizing protons, but estimates vary with ion species and energy [49, p. 388], so equation 6.4 must be used as a guide. After enduring a sufficiently large fluence, a detector becomes inoperable due to the increase in leakage current. This situation may be rectified by cooling the detector since the leakage current is a strong function of the temperature of the detector.

$$\frac{I_R(T_2)}{I_R(T_1)} = \left(\frac{T_2}{T_1}\right)^2 \exp\left[-\frac{E}{2k}\left(\frac{T_1 - T_2}{T_1 T_2}\right)\right], \quad (6.5)$$

where I_R is the leakage current as a function of temperatures T_1 and T_2 , k is the Boltzmann constant, and $E = 1.2$ eV is the ionization energy of crystalline Si. Equation 6.5 shows that cooling the detector from room temperature to 0 °C should yield a 6-fold reduction in leakage current.

6.3.2 Radiation Damage to the DRAGON DSSSDs

It is never the intent of DRAGON operators to impinge the heavy ion beam delivered by ISAC directly onto the DRAGON DSSSD since doing so induces significant radiation damage in the DSSSD. However, several of the DRAGON DSSSDs have been subject to a full or partial ion beam for a sufficient duration to induce damage, due to errors made while tuning the magnetic and electrostatic elements of the separator. The DSSSDs subjected to

the beam are no longer able to hold the full depletion bias without exceeding the maximum allowable leakage current of $2 \mu\text{A}$ at room temperature.

In the high particle fluence environments of high energy particle physics experiments, a DSSSD can maintain operation up to minimum ionizing proton fluences larger than 10^{15} cm^{-2} provided that it is cooled to between $-10 \text{ }^\circ\text{C}$ and $0 \text{ }^\circ\text{C}$ [96]. A typical stable beam intensity for DRAGON experiments is 15 p nA (particle nano-Amperes) which is about 10^{11} ions/s. If the DRAGON DSSSDs were exposed to this full beam for less than 100 s , then the DSSSDs were exposed to less than 10^{13} ions. Assuming that the increase in leakage current induced by a given number of low energy heavy ions is less than 100 times that for the same number of minimum ionizing protons (this is a reasonable assumption [49, p. 388]), the damaged DSSSDs should function when cooled. Design II of the cooling system was used to test the effects of cooling on the radiation damaged DRAGON DSSSDs.

6.3.3 Inventory of the DRAGON Silicon Strip Detectors

In the summer of 2002, an inventory was taken of the DRAGON silicon strip detectors, including one single sided silicon strip detector (SSSSD). Recorded were their serial number, apparent macroscopic damage, and the extent of radiation damage gauged by the bias they could hold at $2 \mu\text{A}$ leakage current and room temperature. Shown in table 6.4 is an update of this inventory on 02/25/03 for the reference of the reader when tests with a specific detector are discussed.

6.3.4 Cooling Radiation Damaged DSSSDs

The effect of cooling on efficiency and resolution of the radiation damaged DSSSDs was tested and compared to undamaged silicon strip detectors (SSDs). Each detector was exposed to a $2 \mu\text{Ci } ^{241}\text{Am}$ α -particle source at a distance of 10 cm . Radiation damaged DSSSDs were each cooled to $-3.8 \text{ }^\circ\text{C}$ while undamaged SSDs were run at room temperature. In all cases the source geometry and electronics were identical. This gave a reliable comparison between new SSDs run at room temperature and cooled, damaged DSSSDs.

As shown in table 6.5, there is no significant difference in the efficiency of the full energy peak of undamaged SSDs and radiation damaged DSSSDs. The number of counts

Detector	Rad. Damage	Bias (V)	I_r (μA)	Macroscopic damage
DSSSD 1288-3	none	70	0.58	broken wires
SSSSD 1288-15	none	70	0.41	none
DSSSD 1288-18	none	70	1.45	broken wires
DSSSD 2069-5	beam 10/31/01	10	2.00	broken wires
DSSSD 2069-4A	beam 12/05/01	11	2.00	broken wires
DSSSD 2069-3	beam 07/30/02	16.5	2.00	none
DSSSD 2069-1				
DSSSD 1865-16	none	70	0.20	none
DSSSD 2239-3	none	50	0.17	none

Table 6.4: DRAGON silicon strip detector inventory.

Detector	Damage	Peltier (V)	I_r (μA)	Counts	Time (s)	Rate (c/s)	Efficiency
SSSSD 1288-15	none	—	0.35	789 885	1936	408.0	0.929
DSSSD 1288-3	none	—	0.47	266 020	606	439.0	1.000
DSSSD 2239-3	none	—	0.12	260 330	606	429.6	0.979
DSSSD 2069-1	beam	4.0	0.55	269 500	607	444.0	1.011
DSSSD 2069-3	beam	4.0	0.15	272 770	610	447.2	1.019
DSSSD 2069-5	beam	4.0	0.19	263 950	605	436.3	0.994

Table 6.5: Efficiency of undamaged DSSSDs compared with that of radiation damaged DSSSDs.

in the full energy peaks of strips 1 through 12 were summed to produce the column labelled "counts", and a rate was determined from run time. Efficiency data were normalized to DSSSD 1288-3, a DSSSD without radiation damage. The only anomalous efficiency is in SSSSD 1288-15 which is an old SSSSD. The small differences in efficiency between the detectors can be attributed to statistics ($\pm 0.2\%$), and subtle variations in manufacturing between detectors, particularly in the surface area of strips and gaps ($\pm 2\%$).

The energy resolution of damaged DSSSDs is of interest if they are to be used in place of new DSSSDs on DRAGON. Energy resolution data were analyzed by fitting a Gaussian curve to the Gaussian portion of the peak in the energy spectrum of each strip in each SSD. Shown in figure 6.11 is the FWHM energy resolution as a percentage of full pulse height across the front strips of 6 detectors, taken from the same runs as the efficiency data. In general, the undamaged detectors show uniform resolution across the surface of the detector with the exception of strip 11 in SSSSD 1288-15, an anomaly which cannot be due to radiation damage since this detector has not been subject to a large fluence of charged particles. DSSSDs 2069-1 and 2069-5 show good energy resolution in general but show degraded energy resolution near their center which is likely where the beam was incident. In DSSSD 2069-1, which exhibits the largest degradation, the worst resolution is 1.3 % FWHM which is useable. The localization of the resolution degradation could allow the undamaged portions of these DSSSDs to be used without sacrificing optimum energy resolution by localizing the beam and recoil spots. DSSSD 2069-3, a radiation damaged DSSSD, did not show a localized degradation in energy resolution but rather exhibited a poorer overall energy resolution which may be due to damage by a diffuse beam spot.

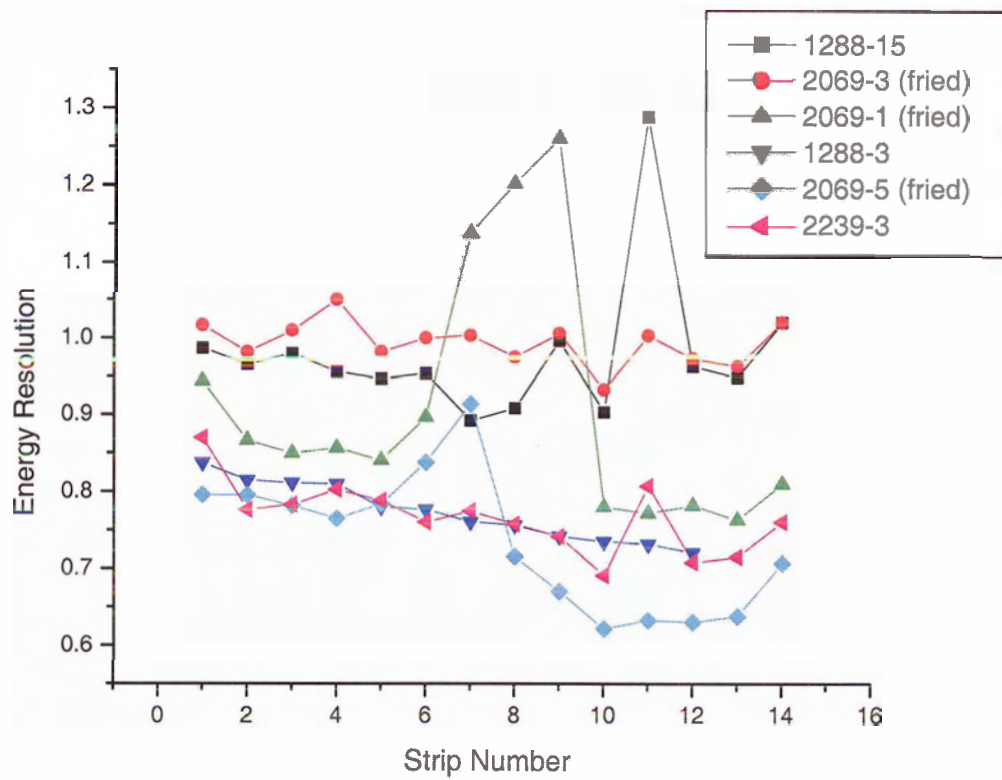


Figure 6.11: Energy resolution of undamaged DSSSDs compared with that of radiation damaged, “fried”, DSSSDs.

Chapter 7

Future prospects for the DRAGON DSSSDs

7.1 A, Z Discrimination

In a silicon detector, the pulse shape produced by an incident ion is a unique signature of its nuclear charge Z [97] and, to a lesser extent, its mass A [98]. Separating recoil ions from beam ions is the purpose of the DRAGON separator. Since some “leaky” beam inevitably passes through the separator, particle identification is an important part of the DRAGON focal plane detection systems. The future prospect of particle identification by pulse shape analysis is, therefore, appealing.

7.1.1 Rise-time

Barring the use of a digital pulse shape analyzer, the most accessible information for particle identification is the rise time of the pulse [97]. The rise time can be separated into two components: the plasma time and the carrier transit time [75, 99].

Plasma Time

When a charged particle enters a silicon detector it produces a column of ionization. Heavier nuclei form a column of ionization (plasma) that is dense in comparison with that of

lighter nuclei. If the plasma is sufficiently dense, then it can locally distort the applied electric field, and shield the inner regions of the column from the external field. The column gradually broadens due to space charge. When the column is sufficiently diffuse, the external electric field is able to penetrate it. The time taken from the formation of the ionization column until all of the charges are under the influence of the field is known as the “plasma time” [75, 99].

It has been estimated [99] that the plasma time, t_{pl} , for a nucleus of mass, M , charge, Z , and energy, E , can be approximated in nanoseconds by:

$$t_{pl}(\text{ns}) = n(MZ^2)^{1/2} \left[B \left(\frac{1}{E} \ln \frac{4m_e E}{MI} \right) \right]^{1/2} / F, \quad (7.1)$$

where $B = 2\pi e^4 N_0 Z / m_e A$ is the Bethe-Bloch constant [42], I is the average ionization energy for the absorbing material, m_e is the rest mass of the electron, F is the applied reverse bias field, and n is a normalization constant which must be determined experimentally. This equation applies for nuclei with ranges much larger than the plasma column diameter.

For ionization tracks which are short compared with the column width (i.e. small E or large A), the expression

$$t_{pl}(\text{ns}) = n(n_1 E)^{1/3} / F \quad (7.2)$$

describes the plasma time in units of nanoseconds [75, 99], where n_1 is the total initial number of carriers per unit length of track and n is again an experimentally determined normalization constant. Equation (7.1) is derived assuming that the majority of charge erosion of the column comes from its sides, whereas (7.2) assumes that the majority of charge erosion of the column comes from its tip. There is also an intermediate situation in which charge collection occurs at comparable rates from the tip and sides. In this case a plasma time may be deduced by weighting (7.1) and (7.2) appropriately.

Carrier Transit Time

Once charges are exposed to the electric field, they are swept to their respective electrodes. The time taken for a charge to reach an electrode once it is under the influence of the field is called the “carrier transit time”. Assuming that the charge carriers travel from the halfway

point of the plasma column to the back electrode at a constant velocity, the transit time is given by:

$$t_{tr}(\text{ns}) = \frac{W - \frac{R}{2}}{V} \quad (7.3)$$

where W is the thickness of the totally depleted detector in μm , R is the particle range in silicon in μm , and V is the charge carrier velocity in $\mu\text{m}/\text{ns}$, which is constant for large field strengths between $0.5 \text{ V}/\mu\text{m}$ and $1.6 \text{ V}/\mu\text{m}$, and field dependent otherwise [100]. The field strength varies throughout the thickness of the DRAGON DSSSD, and in many portions it must be less than $0.5 \text{ V}/\mu\text{m}$, so equation 7.3 is an over-simplification of the carrier transit time. A knowledge of the electric field gradient in the DSSSD is required to accurately model the charge carrier transit time.

7.1.2 Relevance to DRAGON

The characteristic charge collection time, t_{cc} , is given by

$$t_{cc} = t_{pl} + t_{tr}. \quad (7.4)$$

The direct dependence of t_{pl} on Z and A , and the dependence of t_{tr} on particle range R which depends on Z and A through the Bethe-Bloch formula [42] shows that t_{cc} has a dependence on both Z and A .

Ions detected in DRAGON experiments are predicted by SRIM [71] to have ranges of $2.5 \mu\text{m}$ to $20 \mu\text{m}$ in silicon. Since typical ionization tracks are on the order of microns in diameter [75], a combination of the two formulae 7.1 and 7.2 is required to model the plasma times in DRAGON experiments. Since field strengths vary through the thickness of the DSSSD, there are regions in which the charge carrier velocity is constant, and regions in which it is field dependent so the use of equation 7.3 is complicated. The low energy, short range, and proximity in A and Z of ions in DRAGON experiments make the use of rise-time discrimination challenging. Optimization of the technique is crucial if it is to be applied on DRAGON.

7.1.3 Optimizing A, Z Discrimination

The effectiveness of rise-time particle discrimination can be enhanced by the quality of the materials used in fabrication of the detector, the thickness of the detector, the side of the detector exposed to the incident ions, and the electronics used.

Quality of Materials

It has been shown that the quality of the bulk silicon wafer affects the quality of rise-time discrimination between particles [98]. Homogeneity of the resistivity of the bulk silicon have been identified as a major factor that limits this method. It is essential to use a detector with high surface quality and homogeneous doping.

Rear Injection and Thickness

There exists a gradient in the field strength inside a silicon detector. The field is weakest near the rear face, and strongest near the front face because the majority of the DSSSD volume is *n*-type silicon and the $p^+ - n$ junction occurs near the front (p^+) face of the DSSSD. When ions are injected into the detector, the heavier ones do not travel as far as the lighter ones for a given incident energy [42, 71]. Heavier ions produce denser ionization columns and, hence, longer rise-times as modelled by equation 7.1. If ions are allowed to enter the rear (*n*-type) side of the detector, then rise-time differences are enhanced, since the denser ionization columns are subject to a weaker field [101]. It is optimal, therefore, to use a detector whose thickness equals the range of longest range ions that are going to be measured, say 1.5 MeV/u ^{12}C in the case of DRAGON, which penetrates silicon to a distance no greater than 20 μm , as calculated by SRIM [71]. Use of a very thin detector is, therefore, optimal for DRAGON.

Electronics

Fast electronics with large bandwidth ($\gtrsim 300$ MHz) [99] and low noise are required for accurate risetime measurements.

It has been shown that with the conventional use of preamplifiers and amplifiers, the best A, Z discrimination is obtained when the detector is not fully depleted. Using low

bias affects both energy resolution and timing resolution and these cannot be compromised on DRAGON. It has been shown [98] that by taking the signal straight from the preamplifier, good rise-time discrimination can still be obtained with an over-depleted detector, minimizing the detrimental effects on energy and timing resolution.

7.2 Installation of DSSSD Cooling on DRAGON (Cooling System Design III)

Installation of design II of the cooling system at the end of DRAGON has presented some problems.

1. Design II aligns the DSSSD parallel to the vacuum plate, which requires the plate to be mounted vertically on the end of the DSSSD box at the end of DRAGON. This is inconvenient because the DRAGON ionization chamber sits just downstream of the DSSSD box and there is limited clearance for the DSSSD and cooling system feedthroughs.
2. Design II situates the DSSSD 15 cm downstream of the current DSSSD position, which is itself downstream of the final focus of the DRAGON optics design. To date, the settings of the final two DRAGON quadrupoles have been modified to induce a focus on the DSSSD.
3. Design II was tested with cold Vancouver city water which is not available in ISAC. Only TRIUMF recirculating water is available in ISAC and it is approximately room temperature. Room temperature cooling water is insufficient to cool the heat sink in design II of the cooling system.

To rectify the first two problems, a third modification of the cooling system plate was designed and built. Design III positions the DSSSD at right angles to the plate, so that it can be mounted on the top of the DSSSD vacuum box where feedthroughs are easily accessed. Design III situates the DSSSD 3 cm upstream of the conventional position, closer to the design final focus of the DRAGON optics. The plate can still be mounted 15 cm

downstream in the design II configuration if, for example, a slightly longer local time-of-flight is desired. Design III uses two new cooling liquid lines, fed through the vacuum plate and directly to, through, and from a hollowed copper block in contact with the Peltier device which acts as a heat sink. The radiation shield cannot be used with design III, but it is not necessary.

The third problem has several possible solutions. First, infrastructure could be installed that brings city water into ISAC. Second, TRIUMF recirculating water could be cooled with an off-the-shelf refrigerator and fed through the cooling system; this is the cheapest option. Third, a recirculating liquid chiller could be used to cool the DSSSD. This would eliminate the need for a Peltier cooler altogether since it could cool the cold plate to sub-0 °C temperatures on its own. It would also revert to a system whose cumbersome nature initially motivated the investigation of thermoelectric cooling.

Significant improvements to the ISAC infrastructure are required to employ the first option. A modified off-the-shelf refrigerator that incorporates water flow, a function for which it was not designed, may prove unreliable. Therefore, a recirculating liquid chiller will be purchased and installed. The chiller will cool the cold plate to -15°C, and cool the DSSSD to near -10°C without the Peltier device. Absence of the radiation shield will raise the temperature of the DSSSD by less than 5°C. By monitoring the cold plate temperature, the DSSSD temperature will be determined by referring to table 6.2. The recirculating system will allow for the cooling of DRAGON DSSSDs at all times which will enable radiation damaged DSSSDs, and assuage the spike in leakage current when a DSSSD is exposed to the full beam. A schematic of design III of the cooling system is shown in figure 7.1.

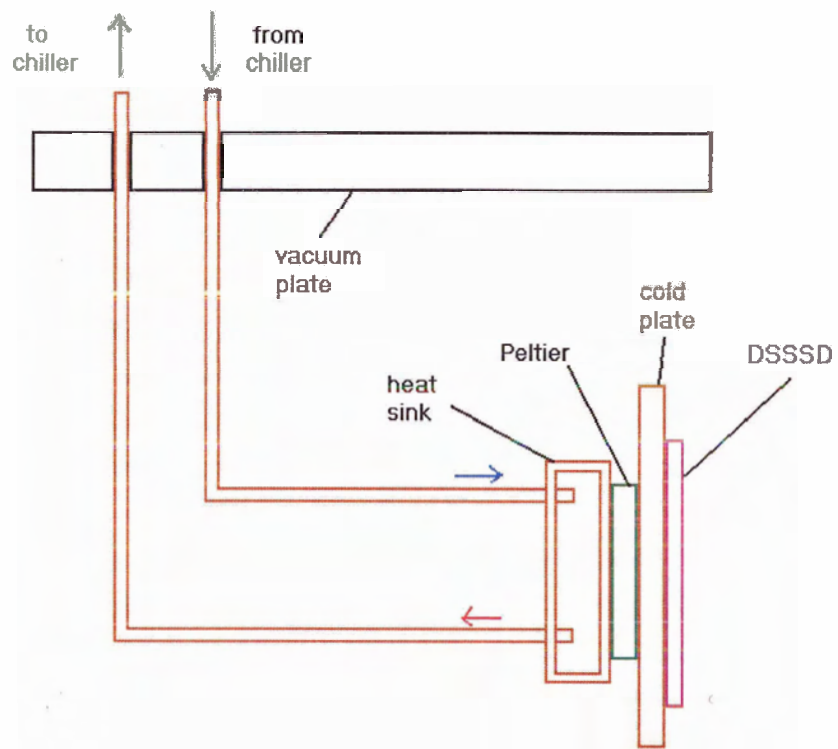


Figure 7.1: Schematic of cooling system design III.

Chapter 8

Conclusions

The properties and performance of several of Micron Semiconductor Model W(DS)-250 DSSSDs and related electronics and data acquisition systems have been tested and optimized using ^{241}Am α -particle sources, ions of mass $A=16$ to $A=25$ and energy 5.25 MeV to 19.4 MeV, and test pulses. The system has been used successfully with DRAGON at TRIUMF-ISAC in measurements of the strengths of several resonances in the $^{21}\text{Na}(p,\gamma)^{22}\text{Mg}$ reaction in inverse kinematics [36] [37]. Individual front (p^+) strips were measured to have energy resolution no worse than 1.0 % for 5.486 MeV α -particles and comparable relative efficiency. Timing resolution of the DSSSDs relative to the radio-frequency of the ISAC RFQ accelerator was measured to be better than 1.2 ns for 16 MeV ^{16}O . Contributors to the pulse height defect have been measured using a variety of ion species on DRAGON, and modelled with the conclusions that SRIM provides a reasonable model for the pulse height defect with $\chi^2 = 0.87$, and that the window defect is the main contributor. The model has predicted the pulse heights for ions that will be encountered in future DRAGON experiments. Events with a reduced pulse height due to the shape of the electric field between strips have been shown to comprise $3.85 \pm 0.10_{stat} \pm 0.43_{sys}$ % of all events for 5.486 MeV α -particles with normal incidence. Each incident α -particle is counted once and only once by one front strip. A hybrid thermoelectric/liquid cooling system has been designed and built which can cool DSSSDs to -13.5 °C. The system has been optimized so that its performance is limited by the competition between radiative heating and slow conductive cooling through the G-10 DSSSD frame. Cooling new DSSSDs using a Peltier device provided no improvement in the energy resolution of new DSSSDs, and damaged them slightly. Ra-

radiation damage to the DRAGON DSSSDs has been assessed with the conclusion that all DSSSDs in the DRAGON inventory which are inoperable at room temperature are operable below 0 °C, with no count deficiency and minimal degradation in energy resolution. Installation of the cooling system on DRAGON using a recirculating liquid chiller sans Peltier is imminent. Pulse shape discrimination for particle identification is an interesting prospect for DRAGON, but it will certainly require new detectors, and likely new electronics.

Bibliography

- [1] J. D. Watson and F. H. C. Crick, *Nature* 171 (1953) 737.
- [2] C. Darwin, *On the Origin of Species* (1859).
- [3] W. Fowler, *Nobel Lectures, Physics 1981-1990*, Elsevier Publishing.
- [4] G. Lemaître, *Ann. Soc. Sci. Bruxelles A47* (1927) 49.
- [5] J. Silk, *The Big Bang* (W. H. Freeman and Company, 1989).
- [6] R. A. Alpher, H. Bethe, G. Gamow, *Phys. Rev.* 73 (1948) 803.
- [7] E. M. Burbidge, G. R. Burbidge, W. A. Fowler and F. Hoyle, *Rev. Mod. Phys.* 29 (1957) 547.
- [8] A. G. W. Cameron, *Atomic Energy of Canada Ltd., CRL-51* (1957).
- [9] G. Wallerstein, I. Iben, P. Parker, A. M. Boesgaard, G. M. Hale, A. E. Champagne, C. A. Barnes, F. Käppeler, V. V. Smith, R. D. Hoffman, F. X. Timmes, C. Sneden, R. N. Boyd, B. S. Meyer, D. L. Lambert, *Rev. Mod. Phys.* 69 (1997) 4.
- [10] S. Burles, K. M. Nollett, J. N. Truran and M. S. Turner, *Phys. Rev. Lett.* 82 (1999) 4176.
- [11] C. E. Rolfs and W. S. Rodney, *Cauldrons in the Cosmos* (University of Chicago Press, 1988).
- [12] E. Anders and M. Grevesse, *Geochim. Cosmochim. Acta* 53 (1989) 197.

- [13] T. Davinson, W. Bradfield-Smith, S. Cherubini, A. DiPietro, W. Galster, A. M. Laird, P. Leleux, A. Ninane, A. N. Ostrowski, A. C. Shotter, J. Vervier and P. J. Woods, Nucl. Instr. and Meth. A454 (2000) 350.
- [14] A. Shotter, Nucl. Instr. and Meth. B204 (2003) 17.
- [15] P. Bricault, R. Baartman, M. Domsbky, A. Hurst, C. Mark, G. Stanford and P. Schmor, Nucl. Phys. A701 (2002) 49.
- [16] R. E. Laxdal, R. A. Baartman, P. Bricault, G. Dutto, R. Poirier, P. Schmor and G. Stanford, Nucl. Phys. A701 (2002) 647.
- [17] D. A. Hutcheon, S. Bishop, L. Buchmann, M. L. Chatterjee, A. A. Chen, J. M. D'Auria, S. Engel, D. Gigliotti, U. Greife, D. Hunter, A. Hussein, C. C. Jewett, N. Khan, A. M. Laird, M. Lamey, W. Liu, A. Olin, D. Ottewell, J. G. Rogers, G. Roy, H. Sprenger and C. Wrede, Nucl. Instr. and Meth. A498 (2003) 190.
- [18] C. Wrede, A. Hussein, J.G. Rogers and J. D'Auria, Nucl. Instr. and Meth. B204 (2003) 619.
- [19] J. Truran, *Essays in Nuclear Astrophysics* (Cambridge University Press, 1982).
- [20] M. Zeilik and S. A. Gregory, *Introductory Astronomy and Astrophysics*, 4th Ed. (Saunders, 1998).
- [21] S. Chandrasekhar, *Astrophys. J.*, 74 (1931) 81.
- [22] W. Y. Law and H. Ritter, *Astron. Astrophys.* 63 (1983) 265.
- [23] R. H. Fowler, *Mon. Not. R. Astron. Soc.* 87 (1926) 114.
- [24] S. Starrfield, *Classical Novae* (Wiley, New York, 1989).
- [25] M. Wiescher, H. Schatz and A. E. Champagne, *Phil. Trans. R. Soc. Lond.* A356 (1988) 2105.
- [26] A. S. Eddington, *The Internal Constitution of Stars* (Cambridge University Press, Cambridge, 1926).

- [27] R. Giacconi, Nobel Lectures, Physics 2001-2010, Elsevier Publishing.
- [28] B. Carroll and D. Ostlie, *An Introduction to Modern Astrophysics* (Addison Wesley, 1996) 598-602.
- [29] W. Baade and F. Zwicky, Phys. Rev. 45 (1934) 138.
- [30] N. K. Glendenning, *Compact Stars: Nuclear Physics, Particle Physics and General Relativity*, 2nd Ed. (Springer-Verlag, New York, 2000).
- [31] F. Hoyle, W. A. Fowler, G. R. Burbidge and E. M. Burbidge, Astrophys. J. 139 (1964) 909.
- [32] F. Pacini, Nature 218 (1967) 567.
- [33] W. H. G. Lewin, J. van Paradijs and R. E. Taam, Space Sci. Rev. 62 (1993) 223.
- [34] R. K. Wallace and S. E. Woosley, Astrophys. J. Suppl. Ser. 45 (1981) 389.
- [35] G. R. Caughlan and W. A. Fowler, Astrophys. J. 136 (1962) 453.
- [36] S. Bishop, Ph.D. thesis, *Direct Measurement of the $^{21}\text{Na}(p,\gamma)^{22}\text{Mg}$ Resonant Reaction Rate in Nova Nucleosynthesis*, Simon Fraser University (2003).
- [37] S. Bishop, R. E. Azuma, L. Buchmann, M. L. Chatterjee, A. A. Chen, J. M. D'Auria, S. Engel, D. Gigliotti, U. Greife, M. Hernanz, D. Hunter, A. Hussein, D. A. Hutcheon, C. C. Jewett, J. Jose, J. King, S. Kubono, M. Lamey, R. Lewis, W. Liu, S. Michimasa, A. Olin, D. Ottewell, P. D. Parker, J. G. Rogers, F. Strieder and C. Wrede, Phys. Rev. Lett. 90 (2003) 162501.
- [38] S. Engel, Ph.D. thesis, *Awakening of the DRAGON - Commissioning of the DRAGON Recoil Separator Facility and First Studies on the $^{21}\text{Na}(p,\gamma)^{22}\text{Mg}$ Reaction*, University of Bochum (2003).
- [39] D. Gigliotti, M.Sc. thesis, *Calibration and Simulation of a Gamma Array for DRAGON at ISAC*, University of Northern British Columbia (2003).
- [40] W. Liu, M.Sc. thesis, *Charge State Studies of Heavy Ions Passing Through Gas*, Simon Fraser University (2001).

- [41] W. Liu, G. Imbriani, L. Buchmann, A. A. Chen, J. M. D'Auria, A. D'Onofrio, S. Engel, L. Gialanella, U. Greife, D. Hunter, A. Hussein, D. A. Hutcheon, A. Olin, D. Ottewell, D. Rogalla, J. Rogers, M. Romano, G. Roy and F. Terrasi, *Nucl. Instr. and Meth.* A496 (2003) 198.
- [42] H. A. Bethe and J. Ashkin, "Passage of Radiations Through Matter" in *Experimental Nuclear Physics*, vol. 1, ed. E. Segre (John Wiley and Sons, New York, 1953).
- [43] S. Engel, S. Bishop, A. Chen, C. Dale, J. M. D'Auria, U. Giesen, U. Greife, R. Henderson, D. Hunter, D. Hutcheon, R. Openshaw, J. Rogers, C. Rolfs and A. Shotter, *Nucl. Phys.* A701 (2002) 228c.
- [44] L. O. Lamm, *Nucl. Instr. and Meth.* 281 (1989) 143.
- [45] C. Jewett, Ph.D. thesis, Colorado School of Mines (in preparation).
- [46] A. Breskin, R. Chechik, Z. Fraenkel, P. Jacobs, I. Tserruya and N. Zwang, *Nucl. Instr. and Meth.* 221 (1984) 363.
- [47] K. E. Rehm and F. L. H. Wolfs, *Nucl. Instr. and Meth.* 273 (1988) 262.
- [48] S. McGee and D. Hunter, *Parallel Grid Avalanche Counter*, DRAGON internal report (2001).
- [49] G. F. Knoll, *Radiation Detection and Measurement* (John Wiley and Sons, New York; 3rd Ed., 2000).
- [50] G. Gabor, *Nucl. Instr. and Meth.* 130 (1975) 65.
- [51] A. N. James, *Nucl. Instr. and Meth.* A267 (1988) 144.
- [52] D. Shapira, T. A. Lewis, L. D. Hulett Jr. and Z. Ciao, *Nucl. Instr. and Meth.* A449 (2000) 396.
- [53] J. Fallis, *Use of a Micro Channel Plate Detector at DRAGON*, DRAGON internal report (2002).
- [54] C. Kittel, *Solid State Physics, 7th Ed.* (John Wiley and Sons, New York, 1996).

- [55] S. M. Sze, *Physics of Semiconductor Devices* (John Wiley and Sons, New York, 1982).
- [56] W. R. Leo, *Techniques for Nuclear and Particle Physics Experiments* (Springer-Verlag, Berlin, 1987).
- [57] Micron Semiconductor, www.micronsemiconductor.co.uk.
- [58] J. Matheson et al. (RD20 Collaboration), *Nucl. Instr. and Meth.* A362 (1995) 297.
- [59] Granville Phillips Company, www.helixtechnology.com.
- [60] Rutherford Appleton Laboratories, www.rl.ac.uk.
- [61] S. L. Thomas, T. Davinson and A. C. Shotter, *Nucl. Instr. and Meth.* A288 (1990) 212.
- [62] Farnell Electronic Components Ltd., www.farnell.com.
- [63] Electro Sonic Inc., www.electrosonic.com.
- [64] Schroff, www.schroff.com.
- [65] Silena International S.p.A., www.silena.com.
- [66] CAMAC is a modular digital data handling system introduced by the European Standards on Nuclear Electronics Committee in 1969. [56, ch. 18].
- [67] LeCroy test and measurement, www.lecroy.com.
- [68] MIDAS is TRIUMF's standard data acquisition system and was developed at the Paul Scherrer Institute (Switzerland) and at TRIUMF.
- [69] PAW (Physics Analysis Workstation) is public domain software package from CERN.
- [70] B. D. Wilkins, M. J. Fluss, S. B. Kaufman, C. E. Gross and E. P. Steinberg, *Nucl. Instr. and Meth.* 92 (1971) 381.
- [71] SRIM 2003 is software developed by J.F. Ziegler that models the stopping and range of ions in matter, <http://www.srim.org/>.
- [72] E. L. Haines and A. B. Whitehead, *Rev. Sci. Instr.* 37 (1966) 190.

- [73] E. C. Finch and A. L. Rodgers, *Nucl. Instr. and Meth.* 113 (1973) 29.
- [74] J. Yorkston, A. C. Shotter, D. B. Syme and G. Huxtable, *Nucl. Instr. and Meth.* A262 (1987) 353.
- [75] W. Seibt, K. E. Sundstrom and P. A. Tove, *Nucl. Instr. and Meth.* 113 (1973) 317.
- [76] M. Martini, T. A. McMath and I. L. Fowler, *IEEE Trans. Nucl. Sci.* 17 (1970) 139.
- [77] F. Calligaris, P. Ciuti, I. Gabrielli and R. Giacomich, *Nucl. Instr. and Meth.* 112 (1973) 591.
- [78] A. F. Ioffe, *Poluprovoduikovye Termoelementy* (Moskow-Leningrad, 1956).
- [79] J. Peltier, *Ann. Chem.*, LVI (1834) 371.
- [80] H. J. Goldsmith, *Applications of Thermoelectricity* (London, Methuen, 1960).
- [81] R. A. Serway, *Physics for Scientists and Engineers*, 3rd Ed. (Saunders, New York, 1992).
- [82] *CRC Handbook of Chemistry and Physics*, 70th Ed. (CRC Press, Baton Rouge, 1989).
- [83] M. Planck, *Ann. Physik* 4 (1901) 533.
- [84] J. Stefan, *über die Beziehung zwischen der Wärmestrahlung* (1879).
- [85] L. Boltzmann, *Ableitung des Stefan'schen Gesetzes* (1883).
- [86] Leufken Technologies, www.leufkentechnologies.com.
- [87] Hewlett-Packard Company, www.hp.com.
- [88] Fluke Electronics, www.fluke.com.
- [89] Aavid Thermalloy Inc., www.aavidthermalloy.com.
- [90] L. Lyons, *Statistics for Nuclear and Particle Physicists* (Cambridge, New York, 1996).
- [91] *Semiconductor Detectors*, eds. G. Bertolini and A. Coche (Noth-Holland Publ. Co., Amsterdam, 1968).

- [92] C. Canali, M. Martini, G. Ottaviani and A. Alberigi-Quaranta, *IEEE Trans. Nucl. Sci.* 19 (1972) 9.
- [93] Ortec, www.ortec-online.com.
- [94] BK Precision Electronic Test Instruments, www.bkprecision.com.
- [95] Particle Data Group, *Review of Particle Properties*, *Phys. Rev. D* 66 (2002) 213.
- [96] G. Lindström, M. Moll and E. Fretwurst, *Nucl. Instr. and Meth.* A426 (1999) 1.
- [97] C. A. J. Ammerlaan et al., *Nucl. Instr. and Meth.* 22 (1963) 189.
- [98] M. Mutterer, W. H. Trzaska, G. P. Tyurin, A. V. Evsenin, J. von Kalben, J. Kemmer, M. Kapusta, V. G. Lyapin and S. V. Khlebnikov, *IEEE Trans. Nucl. Sci.* 47 (2000) 756.
- [99] J. B. A. England, G. M. Field and T. R. Ophel, *Nucl. Instr. and Meth.* A280 (1989) 291.
- [100] P. A. Tove, G. Andersson, G. Ericsson and R. Lidholt, *IEEE Trans. Electron Devices* 17 (1970) 407.
- [101] T. Kitahara, H. Geissel, S. Hofmann, G. Munzenberg and P. Armbruster, *Nucl. Instr. and Meth.* 178 (1980) 201.
- [102] G. Pausch, W. Bohne, H. Fuchs, D. Hilscher, H. Homeyer, H. Morgenstern, A. Tutay and W. Wagner, *Nucl. Instr. and Meth.* A322 (1992) 43.